CRISTA-NF observations in the vicinity of the polar vortex

Dissertation

zur Erlangung des Grades

Doktor der Naturwissenschaften (Dr. rer. nat.)

vorgelegt der

Bergischen Universität
Wuppertal

Fachbereich C – Mathematik und Naturwissenschaften

von

Christoph Kalicinsky

Wuppertal 2013

Die Dissertation kann wie folgt zitiert werden:

urn:nbn:de:hbz:468-20130213-125215-6
[http://nbn-resolving.de/urn/resolver.pl?urn=urn%3Anbn%3Ade%3Ahbz%3A468-20130213-125215-6]

Abstract

CRISTA-NF (Cryogenic Infrared Spectrometers and Telescope for the Atmosphere - New Frontiers) is an infrared limb sounder operated aboard the Russian high-altitude research aircraft M55-Geophysica. The instrument measures thermal emissions of the atmosphere in the spectral range from 4 – 15 µm between flight altitude (≈ 20 km) and around 5 km. CRISTA-NF successfully participated in a large polar aircraft campaign within the EU FP7-project RECONCILE (Reconciliation of essential process parameters for an enhanced predictability of Arctic stratospheric ozone loss and its climate interactions) in Kiruna (Sweden) from mid-January to mid-March in 2010. The preparation of the instrument for the campaign including calibration measurements as well as performing the measurements during the campaign were part of this work.

The limb emission spectra measured by CRISTA-NF are used to detect polar stratospheric clouds (PSCs) and analyse their composition (NAT, STS, ice). PSCs were observed during the first five flights of the campaign (2010-01-17 – 2010-01-25). A polar stratospheric ice cloud, located above flight altitude during the first flight, is identified by means of the measurements and meteorological data. The observation of polar stratospheric clouds composed of (or clearly dominated by) a large amount of small NAT particles (mean radii < 3 µm) can be excluded by means of the analysis.

The CRISTA-NF measurements enable the derivation of several trace gas volume mixing ratios (e.g. CFC-11, O_3, HNO_3) with an unprecedented vertical resolution of around 500 – 600 m (or even less for CFC-11) for several kilometres below flight altitude and a horizontal sampling along flight direction of ≈ 15 km. Comparisons with in-situ and remote sensing measurements illustrate the quality of the retrieved volume mixing ratios.

Flight 11 of the aircraft campaign, which took place on March 2 in the vicinity of the polar vortex, is analysed in detail. The observations of the polar vortex (including the bottom edge of the vortex) and two filaments of different origin are presented. By means of O_3-CFC-11-relations these filaments are clearly identified as one vortex and one non-vortex filament.

The obtained results are compared with simulations by CLaMS (Chemical Lagrangian Model of the Stratosphere) to assess the model performance in terms of transport and chemical processes. CLaMS is capable of simulating even small scale transport structures. But the comparisons indicate an underestimation of the ozone depletion inside the vortex. Additionally, a model concept using artificial tracers, which enables the differentiation of air masses with respect to their origin, is validated. The date of the artificial tracer initialisation is very important to obtain simulation results, which are comparable to the observations. These

tracers can be used to obtain additional information about the air mass origin. Furthermore, the artificial tracers are used to determine the impact of a vortex split event in December 2009 on the composition of air masses inside the vortex.

Zusammenfassung

CRISTA-NF (Cryogenic Infrared Spectrometers and Telescope for the Atmosphere - New Frontiers) ist ein Infrarot-Horizontsondierer, der an Bord des russischen Höhenforschungsflugzeuges M55-Geophysica eingesetzt wird. Das Instrument misst thermische Emissionen der Atmosphäre im Spektralbereich von 4 - 15 µm zwischen Flughöhe (≈ 20 km) und ungefähr 5 km. CRISTA-NF hat erfolgreich an einer großen polaren Flugzeugmesskampagne innerhalb des EU FP7-Projekts RECONCILE (Reconciliation of essential process parameters for an enhanced predictability of Arctic stratospheric ozone loss and its climate interactions) in Kiruna (Schweden) von Mitte Januar bis Mitte März 2010 teilgenommen. Die Vorbereitung des Instruments auf die Kampagne einschließlich der Kalibrationsmessungen, sowie die Durchführung der Messungen während der Kampagne waren Bestandteil dieser Arbeit.

Die von CRISTA-NF gemessenen Emissionsspektren werden verwendet, um polare Stratosphärenwolken (PSCs) zu erkennen und ihre Zusammensetzung (NAT, STS, Eis) zu untersuchen. PSCs wurden während der ersten fünf Flüge der Kampagne (17.01. – 25.01.2010) beobachtet. Mit Hilfe der Messungen und meteorologischen Daten kann eine stratosphärische Eiswolke, die sich während des ersten Fluges oberhalb der Flughöhe befand, identifiziert werden. Die Beobachtung von polaren Stratosphärenwolken, die aus einer großen Anzahl von kleinen NAT-Teilchen (mittlerer Radius $< 3\,\mu m$) bestehen (oder klar dominiert sind), kann mit Hilfe der Analyse ausgeschlossen werden.

Die Messungen ermöglichen die Bestimmung der Mischungsverhältnisse mehrerer Spurengase (z.B. CFC-11, O_3, HNO_3) mit einer bis jetzt unerreichten vertikalen Auflösung von ungefähr 500 – 600 m (oder weniger für CFC-11) über mehrere Kilometer unterhalb der Flughöhe und einem horizontalen Sampling von ≈ 15 km entlang des Flugpfades. Vergleiche mit insitu- und Fernerkundungsmessungen bestätigen die Qualität der bestimmten Mischungsverhältnisse.

Flug 11 der Kampagne, der am 2. März im Bereich des Polarwirbels stattfand, wird im Detail untersucht. Während des Fluges wurden der Polarwirbel (einschließlich der Unterkante) und zwei Filamente unterschiedlicher Herkunft beobachtet. Diese Filamente werden mit Hilfe von O_3-CFC-11-Relationen eindeutig als ein Vortexfilament und ein Filament anderer Herkunft indentifiziert.

Die erzielten Ergebnisse werden mit CLaMS (Chemical Lagrangian Model of the Stratosphere) Simulationen verglichen, um die Leistungsfähigkeit des Modells hinsichtlich Transport und chemischen Prozessen zu beurteilen. CLaMS ermöglicht die Simulation sehr kleinskaliger Transportprozesse. Die Vergleiche zeigen aber eine Unterschätzung des Ozonver-

lusts im Polarwirbel. Zusätzlich wird ein Modellkonzept, das künstliche Tracer verwendet und die Unterscheidung von Luftmassen bezüglich ihrer Herkunft ermöglicht, überprüft. Der Initialisierungszeitpunkt dieser Tracer ist dabei von großer Bedeutung, um Simulationsergebnisse zu erhalten, die vergleichbar zu den Beobachtungen sind und zusätzliche Informationen über die Luftmassenherkunft liefern. Zudem werden die künstlichen Tracer verwendet, um die Auswirkung eines Wirbelsplits im Dezember 2009 auf die Luftmassenzusammensetzung innerhalb des Wirbels zu bestimmen.

Contents

List of Figures

List of Tables

1. Introduction

In addition to its main components, N_2, O_2, and noble gases, the Earth's atmosphere contains also trace gases that exist in very small amounts. Some of these gases, like CO_2, O_3, and methane are important greenhouse gases. Like water vapour, they have a large impact on the radiative forcing of the atmosphere and are thus of great interest (e.g. IPCC, 2007).

The representation of greenhouse gases in climate and other atmospheric models generally involves two major sources of uncertainty. The first is the definition of emission scenarios for anthropogenic greenhouse gases such as carbon dioxide and methane. The second is the representation of physical and chemical processes that affect their spatial and temporal distribution in the atmosphere in particular in the region of the upper troposphere and lower stratosphere (UTLS) (e.g. Riese et al., 2012). An adequate representation of natural greenhouse gases such as water vapour and ozone, which exhibit large spatial gradients in the UTLS, relies on a realistic representation of transport processes (advection and mixing) in the atmosphere (e.g. stratosphere-troposphere exchange). Transport processes typically involve small (tens of km) filamentary structures that can be seen in the distribution of rather inert trace gases (e.g. CFCs). Such trace gases serve as indicators of atmospheric transport. A detailed understanding of these transport processes is a prerequisite for improved atmospheric models and enhanced prediction capabilities of climate models. Remote sensing instruments provide a good basis for the analysis of atmospheric trace gases. The great advantage of such instruments is the capability of measuring different atmospheric constituents without getting in contact with the observed air masses.

Limb sounders, a class of remote sensing instruments, scan the atmosphere and therefore provide measurements of vertical trace gas profiles. They are operated on different platforms, like satellites, aircraft or balloons. Satellite instruments, e.g. CRISTA (Cryogenic Infrared Spectrometers and Telescopes for the Atmosphere; Offermann et al., 1999; Grossmann et al., 2002), MIPAS-ENV (Michelson Interferometer for Passive Atmospheric

Sounding-ENVisat; Fischer et al., 2008), HIRDLS (High-Resolution Dynamics Limb Sounder; Gille et al., 2003), enable the measurement of trace gas profiles with nearly global coverage and therefore the investigation of the three-dimensional structure of the atmosphere on a global scale. Compared to satellite instruments airborne instruments provide measurements with a significantly increased vertical resolution and horizontal sampling but a decreased coverage. Limb sounders operated aboard an aircraft thus allow for the analysis of small scale structures and features in the atmosphere on a local scale.

In this work the measurements of the airborne infrared limb sounder CRISTA-NF (Cryogenic Infrared Spectrometers and Telescope for the Atmosphere - New Frontiers; Kullmann et al., 2004) are analysed and discussed. CRISTA-NF is a succession instrument of the satellite infrared limb sounder CRISTA and is operated aboard the Russian research aircraft M55-Geophysica. According to the maximum flight altitude of the M55-Geophysica of around 20 km, CRISTA-NF is well suited to analyse the upper troposphere / lower stratosphere (UTLS) region. This particular region and composition changes therein are very important for the radiative forcing of the atmosphere (e.g. Riese et al., 2012). A variety of advection and mixing processes occur in this region and influence the trace gas composition (e.g. Gettelman et al., 2011). Former studies by Weigel et al. (2010) already showed the capability of CRISTA-NF to investigate mixing processes in the UTLS.

The measurements presented and discussed in this work were obtained during a large aircraft measurement campaign in Kiruna (Sweden) between January and March, 2010. The campaign was part of RECONCILE (Reconciliation of essential process parameters for an enhanced predictability of Arctic stratospheric ozone loss and its climate interactions), a FP7 (7th Framework Programme) project funded by the European Union (EU).

Scientists of 10 European measurement groups participated with more than 20 instruments in the aircraft campaign. The instruments were operated to measure the chemical composition of the Arctic stratosphere as well as particle properties and distributions. These measurements allow for the investigation and understanding of the dynamics, chemistry and cloud microphysics in the Arctic polar stratosphere. Detailed information about the aircraft campaign and the RECONCILE project can be obtained from the internet page `https://www.fp7-reconcile.eu/`. In the time period of the campaign (mid-January – mid-March, 2010) 12 flights took place in the area around Kiruna. A summary of the flights is given in Tab. 1.1.

The measurements during the RECONCILE aircraft campaign took all place in the vicinity of the polar vortex. Hence, the main scientific objectives of this thesis are the formation of the vortex and vortex filaments as well as mixing processes in the vicinity of the vortex. CRISTA-NF provides measurements of different atmospheric trace gases (e.g. CFC-11, O_3, $ClONO_2$) with an unprecedented vertical resolution and is for this reason very well suited to analyse small scale structures with an vertical extent even less than 1 km. Furthermore, the measurements provide a good basis for the differentiation of air masses in terms of their origin.

Table 1.1: Summary of the flights during the RECONCILE aircraft campaign.

flight number	flight date	flight time in UTC (airport)	PSC occurrence
1	2010-01-17	11:17 (Kiruna) – 15:33 (Kiruna)	yes
2	2010-01-20	08:13 (Kiruna) – 11:55 (Kiruna)	yes
3	2010-01-22	10:01 (Kiruna) – 13:35 (Kiruna)	yes
4	2010-01-24	13:30 (Kiruna) – 16:56 (Kiruna)	yes
5	2010-01-25	05:50 (Kiruna) – 09:19 (Kiruna)	yes
6	2010-01-28	09:00 (Kiruna) – 12:56 (Kiruna)	no
7	2010-01-30	06:36 (Kiruna) – 10:15 (Kiruna)	no
8	2010-02-02	10:01 (Kiruna) – 13:31 (Kiruna)	no
9	2010-02-27	12:06 (Kiruna) – 15:41 (Kiruna)	no
10	2010-03-02	02:51 (Kiruna) – 06:31 (Spitsbergen)	no
11	2010-03-02	09:35 (Spitsbergen) – 13:35 (Kiruna)	no
12	2010-03-05	15:05 (Kiruna) – 18:36 (Kiruna)	no

The unprecedented vertical resolution of the measurements enables excellent comparisons with the chemistry transport model (CTM) CLaMS (Chemical Lagrangian Model of the Stratosphere; McKenna et al., 2002b,a; Konopka et al., 2004, 2007). Since the vertical resolution of measurements and simulations are nearly identical, no convolution of the CLaMS results is necessary. By means of these comparisons the performance of CLaMS with respect to dynamics and chemistry can be assessed and model concepts can be validated.

Another scientific objective with respect to the polar vortex is the formation and composition of polar stratospheric clouds (PSCs). PSCs are involved in the ozone chemistry inside the polar vortex and the denitrification of the stratosphere. Therefore, they are important for the understanding of the chemistry inside the vortex (e.g. Toon et al., 1986; Crutzen and Arnold, 1986; Solomon et al., 1986; Solomon, 1999). Infrared limb sounders are very sensitive to cloud detection and can contribute to the examination of the PSC composition (e.g. Spang and Remedios, 2003; Höpfner et al., 2009; Spang et al., 2012).

The thesis is structured as follows. Chapter 2 briefly summarises fundamental information about the polar vortex, polar stratospheric clouds and the ozone chemistry inside the vortex. Details about the CRISTA-NF instrument and the measurement geometry as well as the essential steps in data processing are given in chapter 3. Chapter 4 proceeds with a detailed analysis of the observations of polar stratospheric clouds with respect to the composition. Furthermore, the location of an observed polar stratospheric ice cloud is examined by means meteorological data. The next chapter gives an overview of the derivation of atmospheric constituents (so called retrieval) from the limb emission spectra measured by CRISTA-NF and highlights the unprecedented vertical resolution achievable with this measurements. Chapter 6 and chapter 7 show a detailed examination of one RECONCILE flight and comparisons with CLaMS. The observation of the polar vortex and filaments of different origin are presented and a model concept, which is capable to differentiate air masses with respect to their origin, is validated.

2. Polar vortex, polar stratospheric clouds and ozone chemistry

The measurement flights during the RECONCILE aircraft campaign took place in the vicinity of the polar vortex. Hence, important information about the polar vortex and related atmospheric phenomena are summarised in this chapter. The sections dealing with polar stratospheric clouds and stratospheric ozone (Sec. 2.2 and Sec. 2.3) are mainly based on the book edited by Müller (2012b).

2.1. Polar vortex

The stratospheric polar vortex denotes a cyclonic air mass located over the winter pole. Inside the polar vortex very low temperatures occur due to radiative cooling, because of the decreasing sun light after equinox in autumn. The resulting pressure gradient in combination with the Earth's rotation cause strong westerlies at the vortex edge. These winds form a mixing barrier which isolates the air masses inside the polar vortex from outside. Furthermore, a subsidence of air masses inside the polar vortex occurs. Because of the inhibited in-mixing, this descent of air masses and therefore of trace gases leads to a large difference of the vertical distribution of trace gases inside and outside the vortex. The low temperatures and the isolation of air masses are prerequisites for the formation of polar stratospheric clouds (see Sec. 2.2) and the ozone depletion inside the vortex (see Sec. 2.3).

A review about the polar vortex and its dynamics is given e.g. by Schoeberl and Hartmann (1991) and Waugh and Polvani (2010). A discussion about the evolution of the Arctic polar vortex in winter 2009/10 is given by Dörnbrack et al. (2012).

2.2. Polar stratospheric clouds

Polar stratospheric clouds (PSCs) are very important for the ozone chemistry inside the polar vortex (see Sec. 2.3) and therefore of great interest. A prerequisite for the formation of PSCs are very low temperatures, like they occur inside the polar vortex. Polar stratospheric clouds can be divided into different types according to their composition. First, one can distinguish two groups, HNO_3-containing PSCs (Type-I) and water-ice PSCs (Type-II). Type-I PSCs can further be divided into Type-Ia (PSCs containing solid particles) and Type-Ib (PSCs containing only liquid particles). The different types of PSCs can form and exist at different temperature conditions.

Polar stratospheric clouds of Type-Ia most likely consist of a noticeable amount of crystalline NAT (nitric acid trihydrate) particles. These NAT particles (HNO_3 and H_2O (1:3)) are thermodynamically stable at temperatures below $\approx$ 195 K (Hanson and Mauersberger, 1988). They can grow to larger particles, which leads to a sedimentation of these particles. As a consequence the stratosphere is denitrified in the source region of the particles. According to the surrounding conditions the NAT particles evaporate at some lower altitudes and a renitrification layer can form (e.g. Waibel et al., 1999; Grooß et al., 2005)

Type-Ib PSCs most likely consist of supercooled ternary solution (STS: H_2SO_4-HNO_3-H_2O) droplets. These liquid PSCs typically form at temperatures below $\approx$ 192 K, which is the dew point of HNO_3. Below this temperature threshold the existing binary H_2SO_4-H_2O droplets take up HNO_3 from the gas phase and build ternary solution droplets (Carslaw et al., 1994; Peter, 1997).

Ice PSCs (Type-II) require temperatures below the frost point T_{ice}. The frost point depends on the pressure and water vapour conditions (Marti and Mauersberger, 1993). According to the conditions in the lower stratosphere in the polar vortex, the frost point T_{ice} is typically around 188 K. Since the temperatures in the Antarctic polar vortex are normally much lower than in the Arctic polar vortex and often below the frost point, the occurrence of ice PSCs in the Antarctic is much more likely than in the Arctic. Nevertheless, ice PSCs can form in the Arctic as well, often due to local temperature minima related to mountain waves. A detailed description of the PSC formation and related topics is given e.g. by Peter (1997), Peter and Grooß (2012) and publications referenced therein.

PSCs can be observed by different remote sensing instruments. The most important technique is the LiDAR (Light Detection And Ranging) technique, which has the capability to observe PSCs and distinguish between the different types due to backscatter and depolarisation signals (e.g Pitts et al., 2009). However, an infrared remote sensing instrument like CRISTA-NF is also capable of observing PSCs of different composition as highlighted in Chapter 4.

2.3. Stratospheric ozone and the ozone hole

Stratospheric ozone is produced by the photolysis of molecular oxygen and the subsequent reaction of the produced atomic oxygen with molecular oxygen. Most of the ozone is therefore produced in the tropics due to the favourable sunlight conditions in this region. As a result, the highest ozone volume mixing ratios at a particular level ($\approx 30\,\mathrm{km}$) occur in the tropics. Furthermore, ozone is transported from the lower tropical stratosphere to the mid-latitudes and polar regions by the Brewer-Dobson circulation. The ozone accumulates in the extra tropics and the maximum in column ozone is therefore in the polar regions. Ozone is destroyed by many different reactions, e.g. in different catalytic cycles involving active nitrogen (NO), hydrogen radicals (H, HO) or active chlorine (Cl). Further information of the stratospheric ozone chemistry and global ozone distribution can be obtained from Müller (2012a) and publications referenced therein.

The situation in winter and spring time in the polar region is more complicated. The first reported observations of reduced total ozone values in Halley Bay (Antarctica) in springtime (October) were made by Farman et al. (1985) with Dobson instruments. These observations were confirmed somewhat later by measurements of TOMS (Total Ozone Mapping Spectrometer) aboard the NIMBUS-7 satellite. The horizontal distribution of this phenomenon, the so called ozone hole, was presented by Stolarski et al. (1986). All mechanisms known at that time could not explain these absence of ozone in the polar stratosphere in spring.

The release of active chlorine from the chlorine reservoir species, e.g. HCl and $ClONO_2$, via heterogeneous reactions on PSC particle surfaces was found to be a prerequisite for the ozone depletion (e.g. Solomon et al., 1986; Solomon, 1999). The most important reactions are:

$$\mathrm{HCl} + \mathrm{ClONO_2} \rightarrow \mathrm{Cl_2} + \mathrm{HNO_3}$$

$$\mathrm{HCl} + \mathrm{HOCl} \rightarrow \mathrm{Cl_2} + \mathrm{H_2O}.$$

The released Cl_2 is photolysed and the atomic chlorine destroys ozone in different catalytic cycles (e.g. Molina and Molina (1987); Müller (2012a); von Hobe and Stroh (2012)).

The denitrification of the stratosphere leads to a suppression or slow down of the back transformation to $ClONO_2$ by the reaction of ClO and NO_2, because of less NO_2 in denitrified air masses, and the ozone destruction lasts longer (e.g. Peter and Grooß, 2012). After the existence of polar stratospheric clouds and cold temperature conditions, chlorine is more and more deactivated and transformed back to the chlorine reservoir species. The ozone destruction therefore decreases. Additional information about the ozone depletion in the polar vortex in spring is given e.g. by Müller (2012a) and von Hobe and Stroh (2012).

3. CRISTA-NF instrument

The Cryogenic Infrared Spectrometers and Telescope for the Atmosphere - New Frontiers (CRISTA-NF) instrument measures thermal emissions of atmospheric trace gases in the mid infrared region (4 – 15 µm) with a very high spatial resolution (250 m vertical and 15 km horizontal) using the limb sounding measurement technique. It is operated aboard the Russian research aircraft M55-Geophysica and has participated successfully in two former tropical aircraft campaigns in Australia (SCOUT-O3) and Africa (AMMA-SCOUT-O3) (e.g. Spang et al., 2008; Hoffman et al., 2009; Weigel et al., 2010).

The CRISTA-NF instrument has been developed from the satellite infrared limb sounder CRISTA, which has participated in two space missions in November 1994 and August 1997 aboard the Shuttle Pallet Satellite SPAS (e.g. Offermann et al., 1999; Grossmann et al., 2002). For the integration on the M55-Geophysica the central CRISTA Herschel telescope and the two Ebert-Fastie grating spectrometers have been installed in a new developed cryostat. A detailed description of the design and the optical system of CRISTA-NF is given by Kullmann et al. (2004).

The following sections give a short overview of the measurement technique of CRISTA-NF and the instrument properties as well as the fundamental steps in calibrating and processing the radiance measurements.

3.1. Limb sounding measurement technique

The CRISTA-NF instrument measures thermal emissions of trace gases in limb geometry. The viewing direction of the instrument is perpendicular to the aircraft's flight direction to the right side and the Earth's atmosphere is scanned from flight altitude down to $\approx$ 5 km with a vertical sampling of $\approx$ 250 m using a tiltable mirror.

Figure 3.1 illustrates the limb sounding geometry. The line of sight (LOS) of the instru-

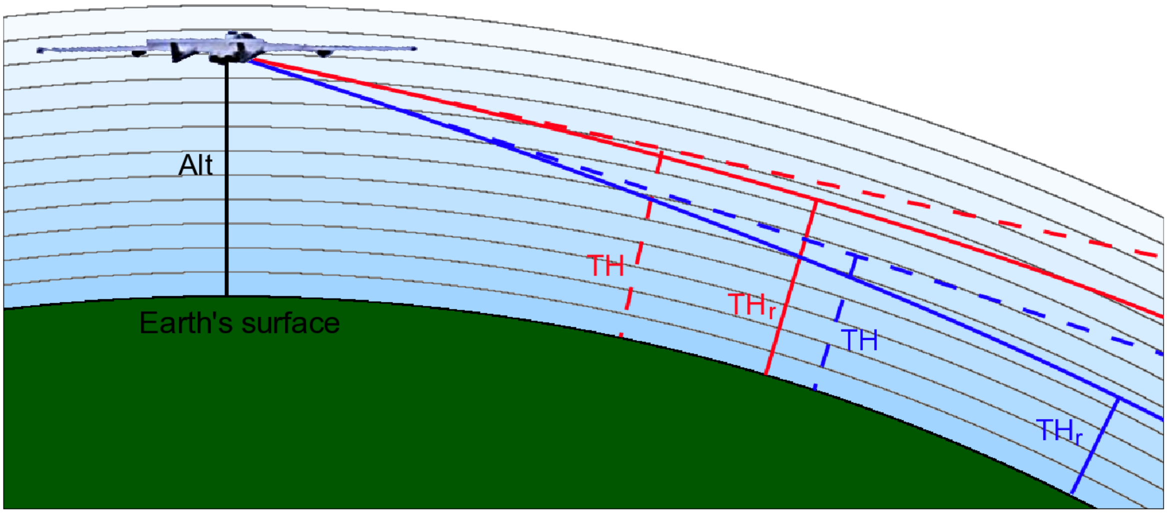

Figure 3.1: The limb sounding geometry. The line of sight (LOS) is shown for two different viewing angles in red and blue, respectively. The dashed lines show the geometric LOS and the corresponding tangent heights (TH), whereas the solid lines show the real LOS including refraction and the corresponding real tangent heights (TH_r). The flight altitude (Alt) of the M55-Geophysica is marked with the black line.

ment is displayed for two different viewing angles (positions of the primary mirror) in red and blue, respectively. The dashed lines show the geometric LOSs. In the Earth's atmosphere a LOS is bended towards the Earth's surface by refraction due to the density gradient. This effect and the resulting real line of sights are illustrated by the solid lines.

The radiance measured by a limb sounder originates along a line of sight. Taking into account the density gradient of the atmosphere and the spherical geometry of the observation, most of the observed radiance is supposed to originate from the point of the LOS closest to Earth. This point is called tangent point (TP), the corresponding altitude is the tangent height (TH). In Figure 3.1 it is obvious that a lower tangent height comes along with a larger horizontal distance between tangent point and instrument. An altitude scan therefore resembles a slant profile rather than a vertical profile.

An example of the distribution of the tangent points of CRISTA-NF measurements is shown in Fig. 3.2. This example is taken from the RECONCILE flight 10, which took place on March 2, 2010. The flight started in Kiruna (Sweden) and ended at the airport of Longyearbyen on Spitsbergen. The tangent points of the measurements are shown as circles, which are coloured according to the corresponding tangent height. The measurements of slant profiles by CRISTA-NF are clearly visible. The lowermost tangent points have a horizontal distance of a few hundred kilometres to the instrument, whereas the position of the highest tangent points is close to the position of the aircraft.

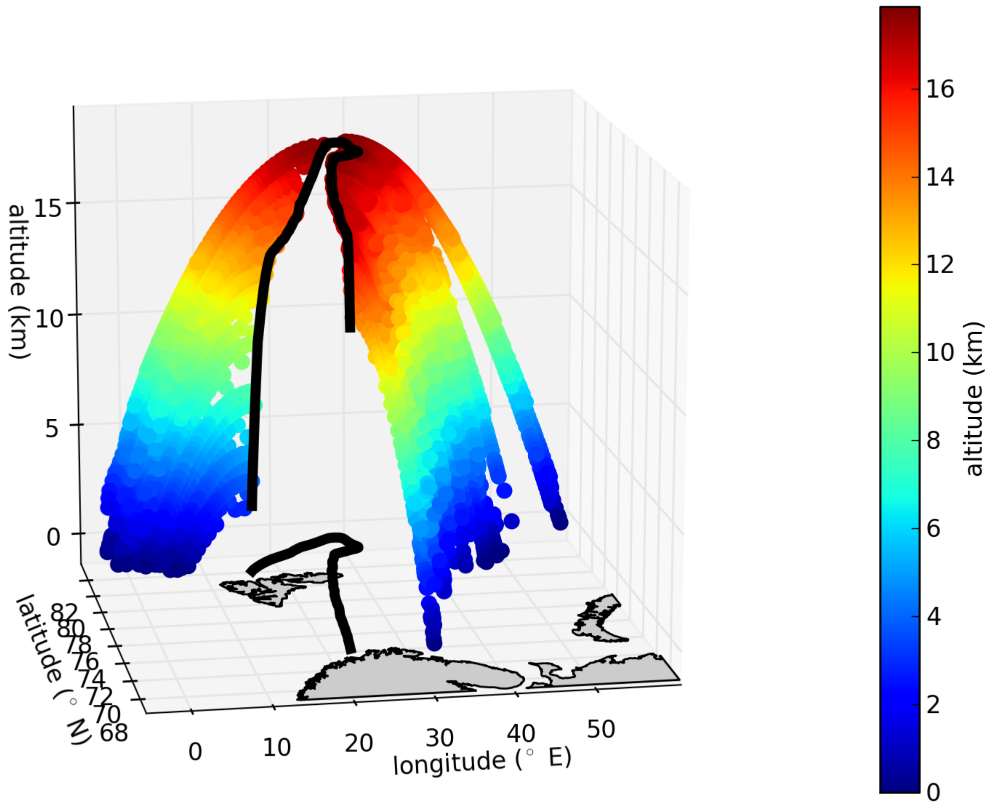

Figure 3.2: Illustration of the CRISTA-NF measurement geometry during RECONCILE flight 10. The tangent points of the measurements are shown as circles coloured according to their tangent height. The flight path of the aircraft is marked by the solid black lines, in three dimensions and as a projection onto the Earth's surface.

3.2. Instrument details

CRISTA-NF contains two Ebert-Fastie grating spectrometers (e.g. Fastie, 1991) that allow for spectrally resolved measurements of the incoming radiance in the spectral range from 4 to 15 µm. These two spectrometers provide different spectral resolutions, $\lambda/\Delta\lambda \approx 1000$ and ≈ 500 for the high resolution spectrometer (HRS) and the low resolution spectrometer (LRS), respectively. The incoming radiance is detected by a number of cryogenic semiconductor (Si:Ga) detectors: 7 for the LRS and 8 for the HRS. A cooling of these detectors down to 13 K is the prerequisite for a good signal to noise ratio, which allows for a high measurement speed of ≈ 1.2 s per spectrum. Apart from that, the whole optical system of CRISTA-NF is cooled to minimise the influence of emissions of the instrument itself on the measurements. A complete altitude scan, consisting of 60 altitude steps (spectra), lasts ≈ 70 s. Due to the flight speed of the aircraft, this leads to a horizontal sampling along the flight track of ≈ 15 km. The field of view (FOV) of the instrument is 3 arcmin × 30 arcmin in vertical times horizontal space. Thus, the vertical extent of the FOV at 10 km tangent height (20 km flight altitude) is ≈ 300 m (Spang et al., 2008).

The comparable small FOV in combination with the very dense vertical and horizontal sampling are prerequisites for the retrieval of two-dimensional trace gas distributions with high spatial resolution.

3.3. Calibration

A wavelength calibration, a LOS calibration and a radiometric absolute calibration are performed to obtain a set of calibration parameters, which is used to calculate meaningful physical values from the recorded output voltages (see Schroeder et al., 2009).

By measurements of absorption spectra of infrared active gases (here NH_3) the relation between the output voltages of the gratings and the wavelength is determined. Since this laboratory wavelength calibration is not accurate enough to fulfil the requirements of a highly precise retrieval, a post-flight wavelength calibration using limb radiance spectra measured by CRISTA-NF during RECONCILE flights is performed to determine final calibration parameters. Details of this procedure are described in A.1.

The LOS calibration is done to determine the relation between the position of the primary mirror of the telescope (recorded in voltages) and the viewing direction of the instrument. The information of the viewing direction of the instrument as well as the attitude and location of the aircraft (instrument) are essential to calculate the tangent point location of each measurement.

Finally, a radiometric absolute calibration is performed by measurements of black-body emissions. The obtained calibration parameters are used to convert the recorded detector voltages into radiance values. See A.2 for detailed information.

The RECONCILE campaign consisted of two observation phases, one in January 2010 and the second from mid-February to mid-March 2010. In the time period between these two phases the CRISTA-NF instrument has warmed and has been cooled down again before the onset of the second phase. This may have had influences on the instrument behaviour. In order to account for possible differences in the two phases a whole set of calibration parameters has been determined before the onset of each observation phase.

3.4. Calibrated limb emission spectra

By means of the obtained calibration parameters limb emission spectra are calculated from the CRISTA-NF output voltages. Examples of such limb emission spectra are shown in Fig. 3.3 for the detector channel LRS 6 (776 – 868 cm^{-1}). All spectra were measured during one altitude scan during the RECONCILE flight 11 (2010-03-02). The colours show the tangent heights of the measurements.

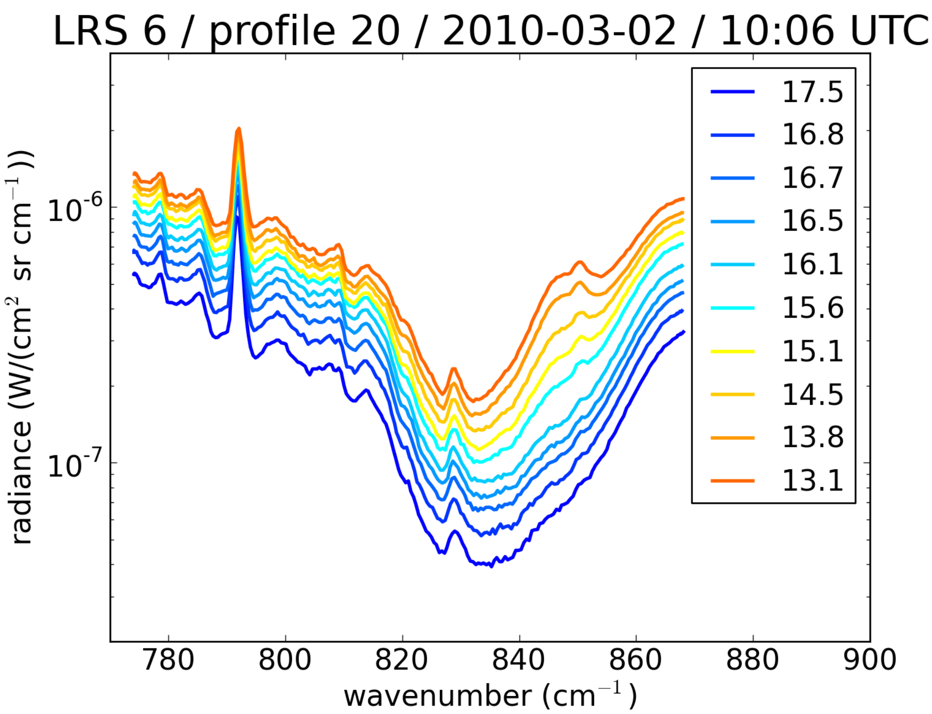

Figure 3.3: CRISTA-NF limb emission spectra at different tangent heights. The spectra were measured during one altitude scan in the detector channel LRS 6 on March 2, 2010 (RECONCILE flight 11). The tangent heights (in km) are illustrated by different colours.

In general, the radiance increases with decreasing tangent height because of the increasing density of the Earth's atmosphere. Furthermore, several spectral features caused by thermal emissions of different trace gases are clearly visible in the spectra. For example, the peak around 792 cm^{-1} is caused by emissions of CO_2 and the enhanced radiance values at the right end of the spectra (wavenumber > 855 cm^{-1}) are caused by emissions of HNO_3. These spectral features partly occur in different spectral regions depending on the trace gas, which facilitates good trace gas retrievals (see. Chap. 5).

Apart from the retrieval of atmospheric trace gases, the limb emission spectra can be analysed in terms of optical conditions and clouds. Even the composition of the observed clouds can be examined by means of the CRISTA-NF measurements (see. Chap. 4).

During one flight around 180 altitude scans, each consisting of 60 altitude steps, are performed. This leads to a total number of more than 10000 spectra for each detector channel and more than 150000 spectra for the fifteen detector channels together. Hence, during the whole RECONCILE aircraft campaign, in which 12 flights were carried out, more than 1800000 spectra were measured in total. Therefore, a large and unique data set is available for this campaign, which can be analysed with respect to different scientific objectives and questions.

3.5. LOS determination

The accuracy of the LOS is a key issue in terms of highly precise retrievals. Therefore, best possible measurements of the roll, pitch, and yaw angle of the instrument and the location of the aircraft (instrument) are necessary. Since the attitude measurements of CRISTA-NF are not accurate enough to calculate precise line of sights, measurements of other attitude systems aboard the M55-Geophysica are needed.

One attitude system providing all required information is the M55-Geophysica attitude system. The attitude angles, the aircraft location as well as pressure and temperature information are recorded and provided by the UCSE (Unit for Connection with Scientific Equipment; MDB, 2002). An obvious time shift between the CRISTA-NF measurements and the attitude measurements of the M55-Geophysica attitude system has to be corrected to obtain LOS information for each measured spectrum by means of the UCSE recordings. This time shift occurs because of an incorrect functionality of the CRISTA-NF internal clock during times, in which the instrument is not operating. The time shift is obtained using a correlation method described by Weigel (2009) (for details, see A.3).

The second instrument aboard the M55-Geophysica providing attitude measurements is the infrared limb sounder MIPAS-STR (Michelson Interferometer for Passive Atmospheric Sounding-STRatospheric aircraft; e.g. Piesch et al., 1996; Keim et al., 2008). The MIPAS-STR Attitude and Heading Reference System (AHRS; Keim, 2002) is rotated by about 90°

with respect to the M55-Geophysica attitude system. Thus, the MIPAS-STR AHRS roll angle (negative value) corresponds to the UCSE pitch angle and the MIPAS-STR AHRS pitch angle corresponds to the UCSE roll angle.

Comparisons between the two attitude information show significant differences larger than the specified uncertainties. Since the MIPAS-STR AHRS is a precise system designed for scientific application and Weigel (2009) showed major deficiencies for the UCSE, the MIPAS-STR AHRS roll and pitch angles are used instead of the UCSE pitch and roll angles.

Remaining offsets in the attitude of the MIPAS-STR and the CRISTA-NF instrument are determined before take off. The knowledge of these offsets provides the possibility to correct the MIPAS-STR AHRS measurements onto the reference system of CRISTA-NF. The other quantities (yaw angle and location), which are needed to calculate the line of sights and the tangent points of the CRISTA-NF measurements, are taken from the UCSE recordings. To obtain a compatible set of quantities an obvious time shift between the MIPAS-STR AHRS measurements and the UCSE recordings has to be corrected. A detailed description of the complete correction procedure is given in A.4.

Fig. 3.4 illustrates the effect of the employment of the MIPAS-STR AHRS measurements. The figure shows the spectrally integrated radiance in the spectral range from 791 to 793 cm^{-1} (integrated micro window (IMW) 791 - 793 cm^{-1}) at the tangent points of the CRISTA-NF measurements calculated by means of the UCSE recordings in panel a) and by means of the MIPAS-STR AHRS measurements in panel b). The example shows measurements carried out during RECONCILE flight 11. In panel a) the measurements of adjacent profiles are shifted towards each other in some parts of the flight, especially at the beginning of the flight, and implausible steps in the radiance values are clearly visible. The use of the MIPAS-STR AHRS pitch and roll angles for the LOS calculation removes nearly all of these steps. Thus, the transition from one profile to the next gets smoother and more reliable.

The MIPAS-STR AHRS measurements are used for the RECONCILE flights 10 and 11, because a retrieval is performed for this flights and an accurate knowledge of the LOS is necessary. For all other flights analysed in this work, the UCSE recordings are used to calculate the LOSs, since no MIPAS-STR AHRS measurements are available. The LOS accuracy requirements are not as stringent in these cases, because the analyses are based on altitude independent methods (see Chap. 4).

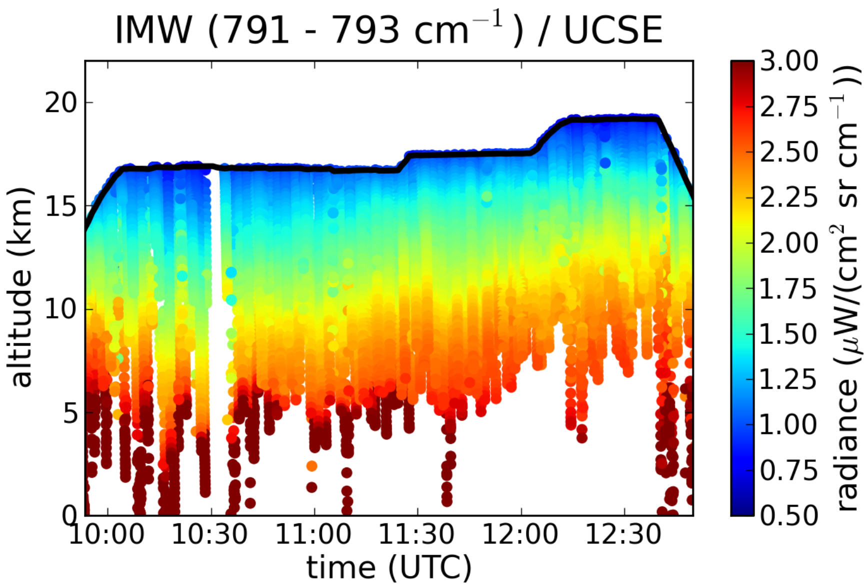

a)

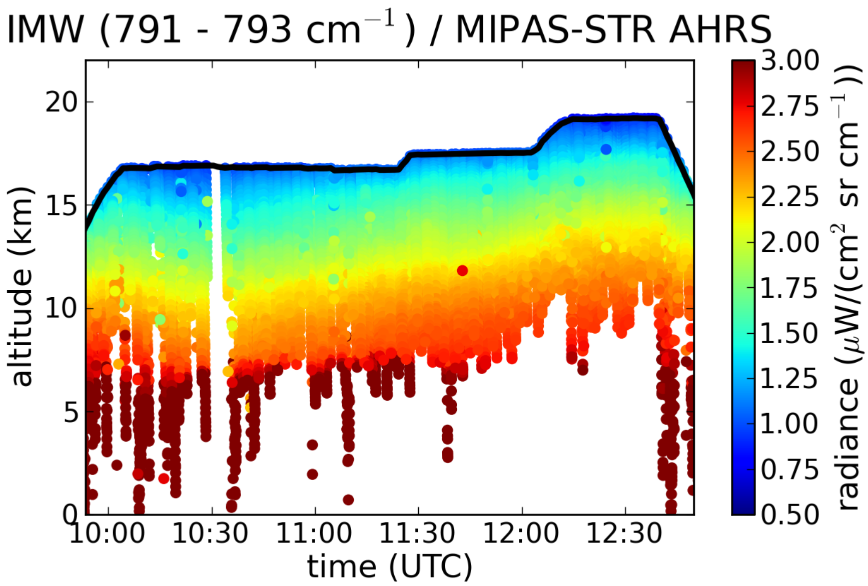

b)

Figure 3.4: Spectrally integrated radiance in the IMW 791 - 793 cm^{-1} at the tangent points of the CRISTA-NF measurements. The tangent points are calculated by means of the UCSE recordings (a)) and by means of the MIPAS-STR AHRS measurements (b)). The measurements are taken from RECONCILE flight 11. The flight path is displayed as solid black line. Note that the offset angles between the aircraft (UCSE) and the CRISTA-NF instrument is not considered in panel a), because of the lack of UCSE recordings before take off. MIPAS-STR AHRS data: courtesy of W. Woiwode and H. Oelhaf.

4. PSC observations and discrimination of PSC types

Infrared limb sounders like CRISTA-NF are very sensitive with respect to cloud detection, especially in the case of thin cirrus clouds and polar stratospheric clouds (e.g. Spang et al., 2001; Massie et al., 2007; Höpfner et al., 2009). The latter clouds play an important role in the denitrification of the stratosphere and the ozone chemistry in polar winter and springtime (e.g. Toon et al., 1986; Solomon et al., 1986; Crutzen and Arnold, 1986; Solomon, 1999). The occurrence of PSCs and their composition are therefore of great interest.

In the following chapter a cloud detection method and the observations of polar stratospheric clouds by CRISTA-NF are presented. Furthermore, the PSCs are analysed in terms of their composition (NAT, STS, ice) by means of different methods. All results are obtained from measurements by the CRISTA-NF detector channels LRS 5 (849 - 963 cm^{-1}) and LRS 6 (776 - 868 cm^{-1}).

4.1. Cloud Index

The cloud index (CI) is a simple and fast method to analyse infrared limb emission spectra in terms of clouds or optically dense conditions due to aerosol. It was originally developed to analyse the infrared limb emission spectra measured by the CRISTA satellite instrument and the MIPAS-ENV (Michelson Interferometer for Passive Atmospheric Sounding-ENVisat; Fischer et al., 2008) instrument (e.g. Spang et al., 2001, 2002, 2005).

The CI is based on the ratio between the spectrally integrated radiance of two spectral windows. These two integrated micro windows (IMW) are located in two spectral regions with quite different characteristics. The first IMW, that extends from 791 to 793 cm^{-1}, is dominated by thermal emission of CO_2, whereas the second IMW, that extends from 832 to 834 cm^{-1}, is located in an atmospheric window and therefore dominated by aerosol. In contrast to the analysis of the CRISTA and MIPAS-ENV data and with respect to the viewing geometry and spatial resolution of CRISTA-NF, the spectral range of the first IMW has been reduced from 788 - 796 cm^{-1} to 791 - 793 cm^{-1} to obtain a higher sensitivity of the ratio (Spang et al., 2008). The ratio between the integrated radiance IMW1/IMW2 is characteristic for the optical conditions during the measurements. A high value of the CI (typically larger than ≈ 3.5) shows cloud free conditions, whereas a small value indicates the presence of clouds or optically dense conditions. In the case of a optically thick cloud the CI reaches values around 1, because the measured spectrum then is nearly equal to a black body spectrum and the radiance values in the two spectral regions are approximately the same. Even values less than 1 can occur if absorption spectra are measured in the presence of clouds. The spectrally integrated radiance in the range from 791 to 793 cm^{-1} is lower than that in the range from 832 to 834 cm^{-1} in this case.

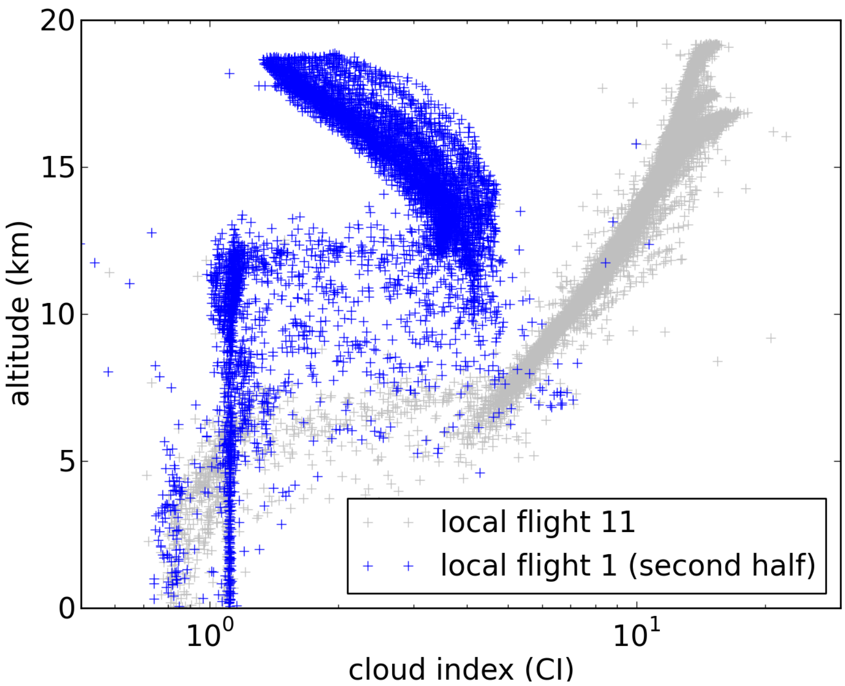

Figure 4.1: Altitude profiles of CRISTA-NF cloud index for RECONCILE flight 11 (grey) and the second half of flight 1 (blue). Note the logarithmic scale of the x-axis.

Fig. 4.1 displays altitude profiles of the cloud index for two different situations. High cloud index values are visible at altitudes above approximately 8 km for flight 11 (grey colours) showing cloud free conditions. Below 8 km very low CI values around 1 indicate the observation of tropospheric clouds. The general decrease of the CI with decreasing altitude is caused by the density of the atmosphere and the increasing aerosol background.

The situation during the second half of flight 1 (blue colours) is different to that. At the highest altitudes and below 13 km low CI values can be seen. In the altitude range in between moderate CI values occur. This indicates the presence of polar stratospheric clouds at altitudes around flight altitude as well as tropospheric clouds below 13 km.

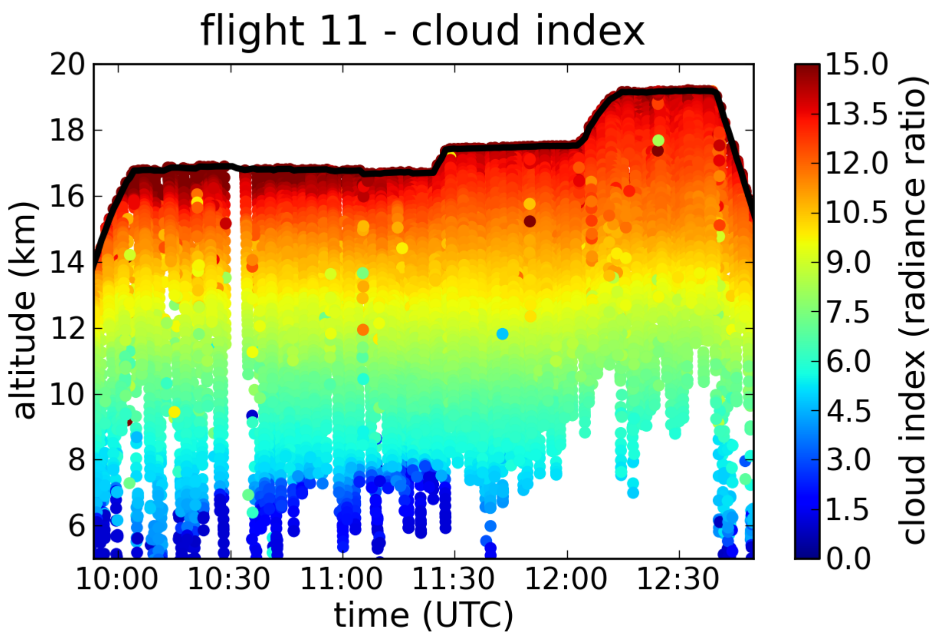

Figure 4.2: Cross section of the CRISTA-NF cloud index during RECONCILE flight 11. The altitude of the aircraft is marked by a solid black line.

In Fig. 4.2 the cloud index is displayed at the tangent points of the measurements for RECONCILE flight 11 on March 2, 2010. The cross section of the CI clearly shows cloud free conditions for the largest part of the measurements and tropospheric clouds below 8 km in the first half of the flight. Since the measurements could be influenced by clouds or aerosols at any point of the line of sight, this altitude of 8 km is not necessarily the cloud top height.

4.2. PSC observations

In the time period of the first five flights (2010-17-01 – 2010-25-01) of the RECONCILE aircraft campaign polar stratospheric clouds were present in the area around Kiruna. Fortunately, the PSCs reached down to altitudes quite below 20 km, which offered the possibility for the M55-Geophysica to cross these PSCs. Fig. 4.3 displays cross sections of the CI for the RECONCILE flights 1 – 5. These cross sections show two different types of clouds, on the one hand, tropospheric clouds and, on the other hand, polar stratospheric clouds.

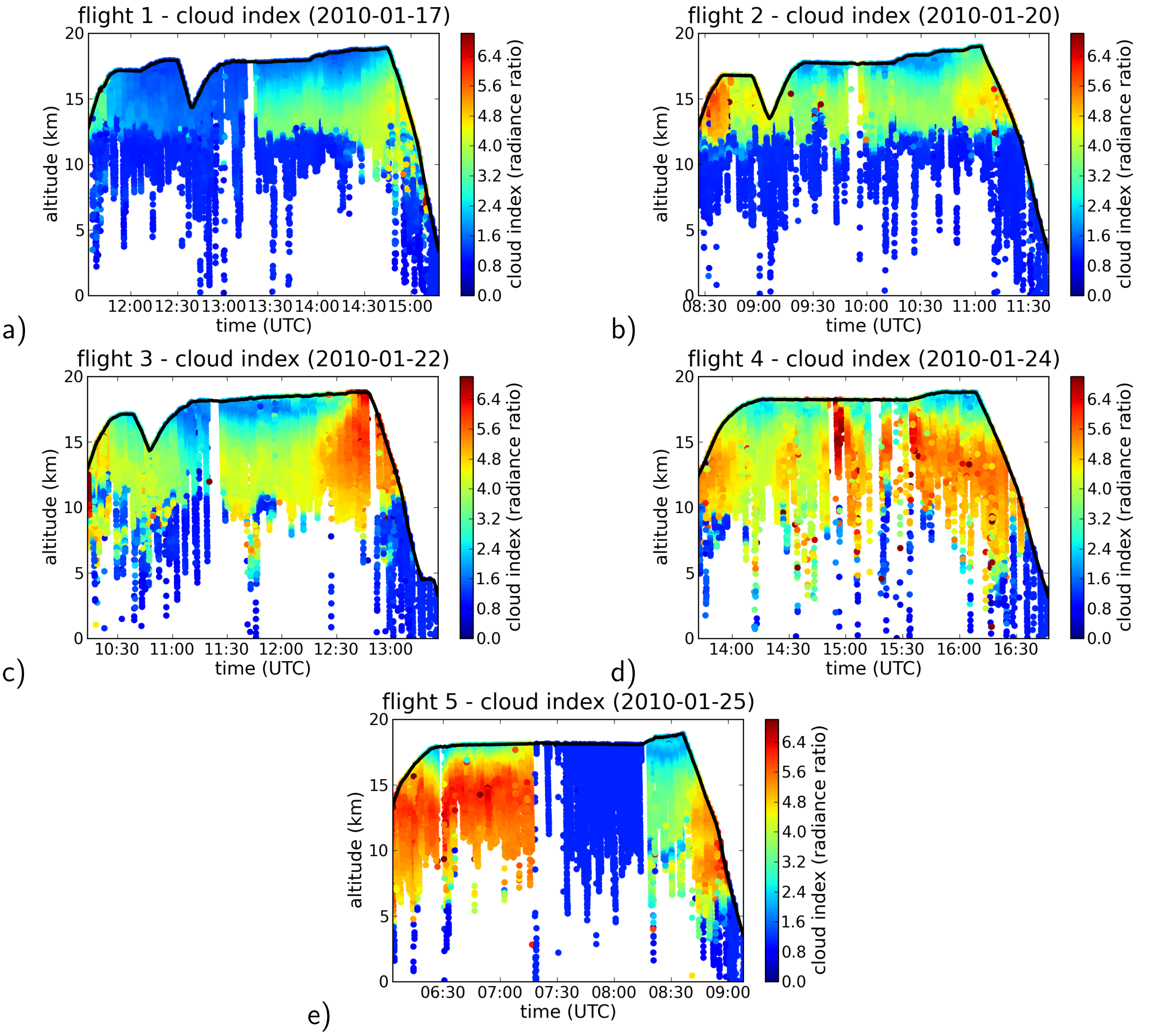

Figure 4.3: Cross sections of the CRISTA-NF cloud index during RECONCILE flight 1-5 (panels a) – e)). The altitude of the aircraft is marked by a solid black line. Note that the CI value of nearly 1 in the middle of flight 5 (panel e)) in the whole altitude range covered by CRISTA-NF is caused by a closed shutter, which acts like a black body.

Since tropospheric clouds are optically very dense, they are indicated by very low CI values of about 1 (dark blue colours). During the first two flights the tropospheric clouds reached altitudes of approximately 13 km because of an exceptionally high thermal tropopause, whereas during the flights 3 – 5 tropospheric clouds can be identified at altitudes mostly below 11 km.

Polar stratospheric clouds are optically thinner than tropospheric clouds and cause therefore slightly higher cloud index values. They are indicated by CI values in the range from about 1.5 to 3.5 (dark blue to light blue colours). PSCs were observed from flight altitude down to a few kilometres below during flight 2 – 4 and during the second half of flight 1. In contrast to that, the influence of PSCs can be seen down to $\approx$ 13 km during the first half of flight 1. The situation responsible for this contrary observation is analysed and discussed below in Sec. 4.4.

In the altitude range between the tropospheric clouds and the PSCs moderate CI values are detected showing more or less cloud free conditions. Due to the lower opacity of PSCs compared to tropospheric clouds, PSCs are only observable if a sufficient part of the line of sight of the instrument is inside a PSC. If the viewing angle of the instrument with respect to the horizon is large enough (lower tangent point) and only a small part of the line of sight is inside a PSC, CRISTA-NF measures spectra that show spectral signatures of atmospheric trace gases. The radiance emitted by trace gases below the polar stratospheric cloud is larger than the emissions of the cloud itself in such cases.

This situation is illustrated in Fig. 4.4. The spectra were measured during an altitude scan in the second half of flight 1, which shows the influence of PSCs for a few kilometres below the flight altitude. At high altitudes (blue and cyan colours) the spectra are very similar to black body spectra and only few spectral signatures of trace gases are visible. As a consequence the CI is very small at these tangent heights. In contrast to that, the spectra at lower altitudes (red and orange colours) show spectral signatures of atmospheric trace gases. The transition from the observation of polar stratospheric clouds to measurements of spectral signatures of trace gases can be seen in Fig. 4.1 as well. The CI values increase with decreasing altitude from flight altitude down to approximately 13 km illustrating the vanishing influence of the emissions of the PSC.

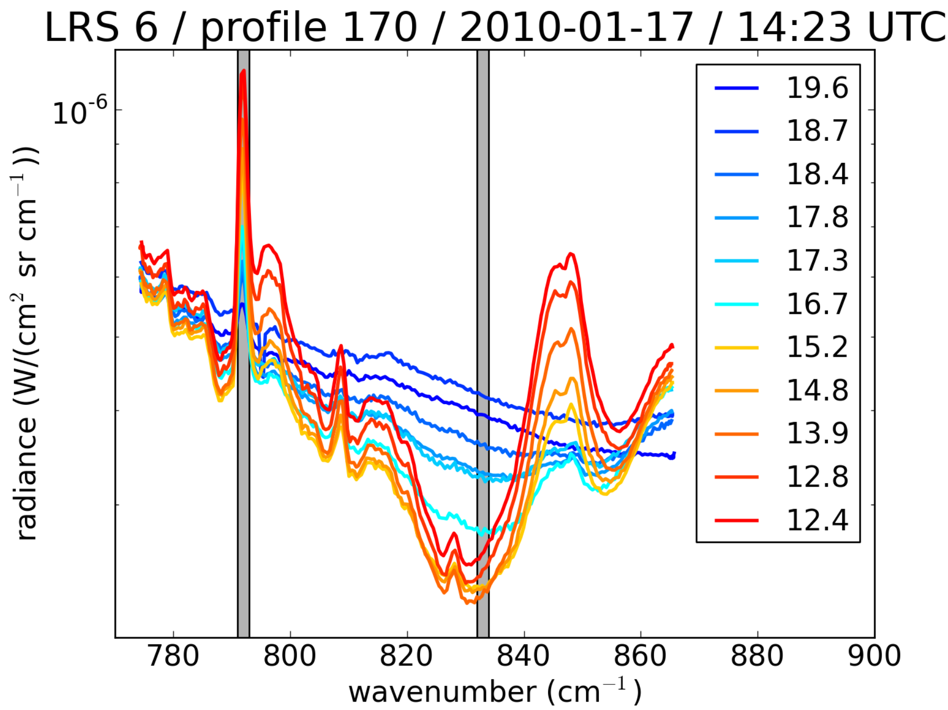

Figure 4.4: CRISTA-NF limb emission spectra in the vicinity of a polar stratospheric cloud. The grey boxes mark the spectral regions of the IMWs used for the cloud index and the tangent height (in km) of each spectrum is shown by different colours.

4.3. Polar stratospheric clouds containing NAT particles

During the CRISTA satellite mission in August 1997 (Grossmann et al., 2002) a distinct spectral feature around 820 cm^{-1} was observed in the presence of polar stratospheric clouds. This feature can only be explained by PSCs of Type-I (HNO_3-containing PSCs) and most likely by PSCs containing NAT particles (Spang and Remedios, 2003). An analysis method utilising two different colour ratios was introduced to detect such polar stratospheric clouds. The first colour ratio is defined as the ratio between the spectrally integrated radiance in the spectral regions 788.2 - 796.25 cm^{-1} and 832.3 - 834.4 cm^{-1} (MIPAS-ENV and CRISTA satellite cloud index (CI_S)) and shows the optical conditions of the measurements. The second colour ratio (NAT index (NI)), integrated radiance in the IMW 819 - 821 cm^{-1} divided by the integrated radiance in the IMW 788.2 - 796.25 cm^{-1}, includes the spectral region of the feature produced by NAT particles. In a scatter plot (NI versus CI_S), the observations of polar stratospheric clouds appear in different areas of the diagram due to their composition. Thus, a discrimination of polar stratospheric clouds is possible (see Höpfner et al., 2006;

Spang et al., 2012).

This section shows radiative transfer simulations for different PSC types to analyse the potential of the described method and the application of the method for the CRISTA-NF measurements.

4.3.1. Radiative transfer simulations

By means of a radiative transfer model limb emission spectra for the MIPAS-ENV satellite instrument for polar stratospheric clouds of different composition were calculated by Höpfner et al. (2006). Apart from the simulations of STS and ice, polar stratospheric clouds containing NAT particles with different particle sizes were simulated. For the different number size distributions of the NAT particles log-normal distributions with mean particle radii from 0.2 μm to 6 μm and a width $\sigma = 1.35$ were used.

The simulations showed a clear separation between PSCs composed of NAT particles with a mean radius ≤ 3 μm and all other types of PSCs (ice, STS, and larger NAT particles with a mean radius ≥ 3 μm). In addition, a separation line was defined as

$$\mathrm{NAT_{thres}} = 1.13/(0.164 + 0.884 \times \mathrm{CI_S} - 0.065 \times \mathrm{CI_S^2}). \tag{4.1}$$

Due to the fact that the spectral feature depends on the radii of the NAT particles and flattens for larger particles, PSCs containing NAT particles with a mean radius ≥ 3 μm cannot be distinguished from other types of polar stratospheric clouds.

Spang et al. (2012) showed simulations based on an updated cloud scenario data base. The results of the simulations are displayed in Fig. 4.5 colour coded for the different cloud types (STS, ice, and NAT). According to these simulations the separation line was slightly adjusted leading to the equation

$$\mathrm{NAT_{thres-new}} = 1.0/(0.1536 + 0.71531 \times \mathrm{CI_S} - 0.03003 \times \mathrm{CI_S^2}). \tag{4.2}$$

Nearly all data points of the simulations for NAT particles with a mean radius of 2 μm are above the separation line, whereas the data points of the simulations for NAT particles with a mean radius of 3 μm lie below or on the separation line. Therefore, the particle size of the NAT particles has to be smaller than 3 μm in radius to be identified with this method. The results of the simulations by Spang et al. (2012) and Höpfner et al. (2006) are in a very good agreement and the defined separation lines are used in the following analyses.

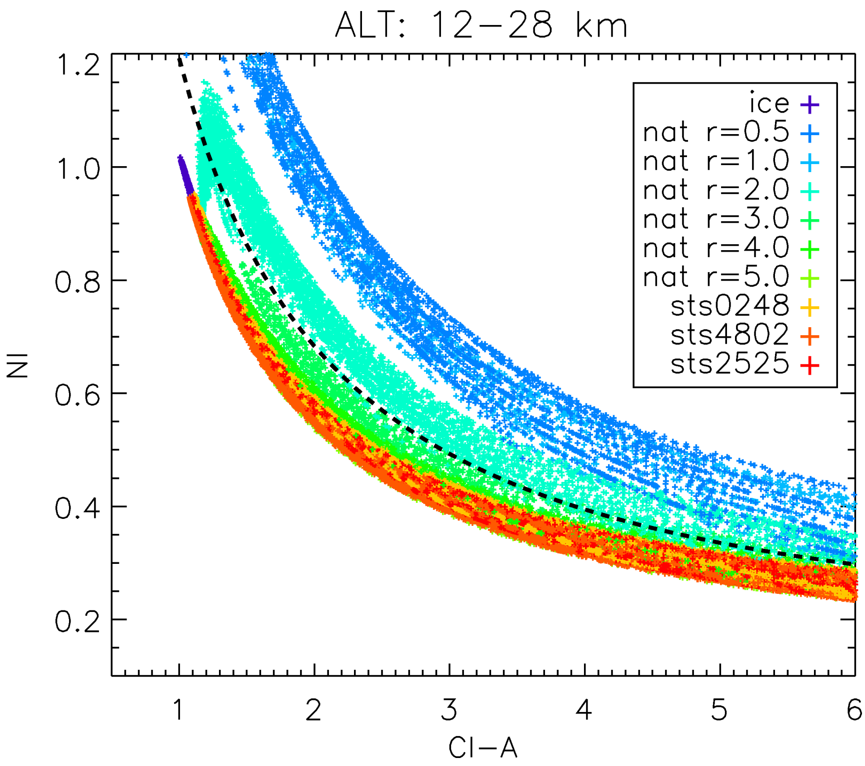

Figure 4.5: NAT index (NI) (819 - 821 cm^{-1}/ 788.2 - 796.25 cm^{-1}) versus cloud index (CI-A) (788.2 - 796.25 cm^{-1}/ 832.3 - 834.4 cm^{-1}). The data are obtained by means of radiative transfer simulations for the MIPAS-ENV satellite instrument. The different cloud types are shown colour coded: STS of different compositions in orange to red (e.g. STS0248 stands for 2 % HNO_3 and 48 % H_2SO_4), ice in dark blue and NAT particles with mean radii between 0.5 μm and 5 μm in green to blue. The dashed black line is the separation line $NAT_{thres-new}$. A width $\sigma = 1.35$ is used for the log-normal distributions of the NAT particles. The cloud index called CI-A (cloud index of the MIPAS-ENV A-band) is equal to CI_S. The plot is taken from Spang et al. (2012)

4.3.2. Results for CRISTA-NF

The described method is applied to analyse the CRISTA-NF measurements, which are carried out in the presence of polar stratospheric clouds (RECONCILE flight 1 – 5). The data are filtered with respect to altitude to analyse only PSCs and exclude measurements of tropospheric clouds. The applied altitude thresholds are the flight altitude of the aircraft and 13 km for flight 1 – 2 and 15 km for flight 3 – 5, respectively. Additionally, all spectra measured during the time period with the closed shutter during flight 5 (see Fig. 4.3) are excluded.

Fig. 4.6 shows the results of the analysis colour coded for the different flights. The two separation lines, equation 4.1 and 4.2, are displayed as a solid black line and a dashed black line, respectively. Nearly all of the data points lie below these separation lines, except for some data points for each flight, which are clearly above. These data points could be attributed to artifacts caused by strong aircraft movements during the measurements, which could not be compensated by the CRISTA-NF active attitude system. As a consequence, the limb emission spectra were not measured at a constant viewing angle of the instrument. The radiance values in the two analysed spectral regions are therefore not comparable and the analysis method not valid during such conditions. Furthermore, some data points at higher CI_S values (> 2.5) are slightly above or on the separation line defined by Spang et al. (2012) (dashed black line). These separation line nearly builds the upper envelope of the data points in the region of higher CI_S values. Nevertheless, no clear evidence for NAT particles with radii less than 3 µm can be found by analysing the CRISTA-NF measurements. But this is not a complete exclusion.

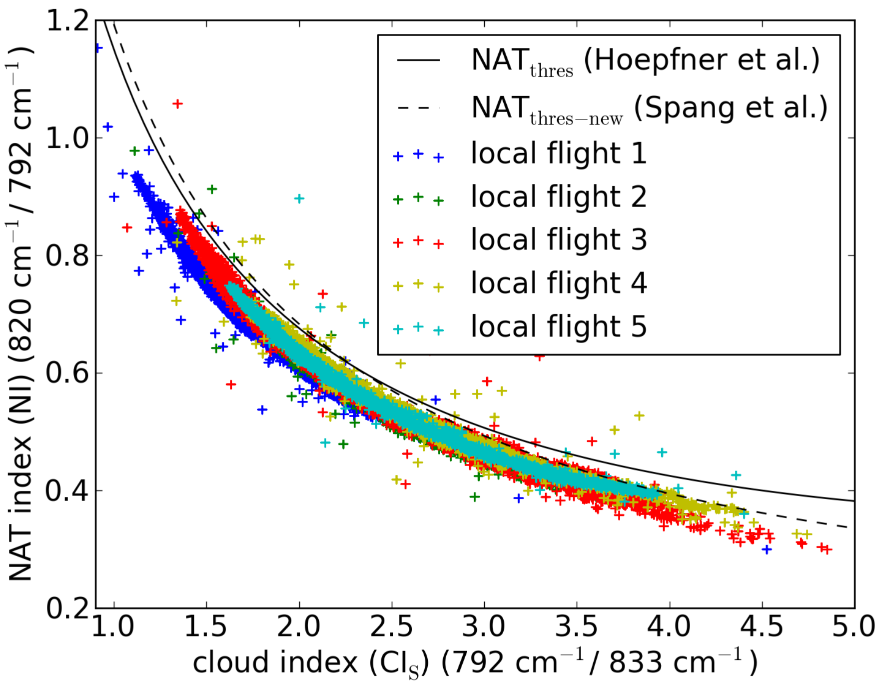

Figure 4.6: NAT index (NI) (819 - 821 cm^{-1}/ 788.2 - 796.25 cm^{-1}) versus cloud index (CI_S) (788.2 - 796.25 cm^{-1}/ 832.3 - 834.4 cm^{-1}) for the first five CRISTA-NF measurement flights during RECONCILE. The different flights are shown colour coded. The two separation lines are taken from Höpfner et al. (2006) (solid black line) and from Spang et al. (2012) (dashed black line).

Studies by Griessbach (2011) showed that the influence of a polar stratospheric cloud composed of both small and large NAT particles on an infrared spectrum is dominated by the large particles. The observation of the feature caused by small NAT particles depends therefore on the proportion of small and large particles as well. If too many large particles are present, the feature will not be visible in a spectrum anymore. Hence, only the presence of PSCs clearly dominated by (or containing only a large number of) small NAT particles can completely be excluded.

4.4. Discrimination of ice PSCs

Based on the different absorption and emission characteristics of ice, STS, and NAT at specific wavelengths, an analysis method has been introduced to separate ice PSCs from other polar stratospheric clouds. This method uses the brightness temperature difference (BTD) between the IMW 832.3 - 834.4 cm^{-1} and the IMW 947.5 - 950.5 cm^{-1}. In a scatter plot, BTD versus cloud index (CI_S), the observations of different PSC types separate from each other (see Spang et al., 2012).

In the following subsections radiative transfer simulations for different PSCs are shown and the possibility to identify ice particles is illustrated.

4.4.1. Radiative transfer simulations

The results of radiative transfer simulations for the MIPAS-ENV satellite instrument and different PSC compositions are shown in Fig. 4.7 (see also Spang et al., 2012). A clear separation between ice PSCs and polar stratospheric clouds consisting of STS of different compositions is visible in panel a). Hence, a threshold line (ice/STS) was empirically defined (dashed black line) to distinguish between ice and STS.

The possibility to differentiate between ice and NAT highly depends on the particle size of the NAT particles (see Fig. 4.7 panel b)). The simulation results for small NAT particles (mean radii smaller than 2 μm) appear in the same region as simulation results for ice. Therefore, only a fraction of the ice PSCs can clearly be distinguished from polar stratospheric clouds containing NAT (dashed black separation line (ice/NAT)). However, these small NAT particles can be identified with the analysis method described in Sec. 4.3 and a differentiation between ice and NAT particles is possible if both methods are used.

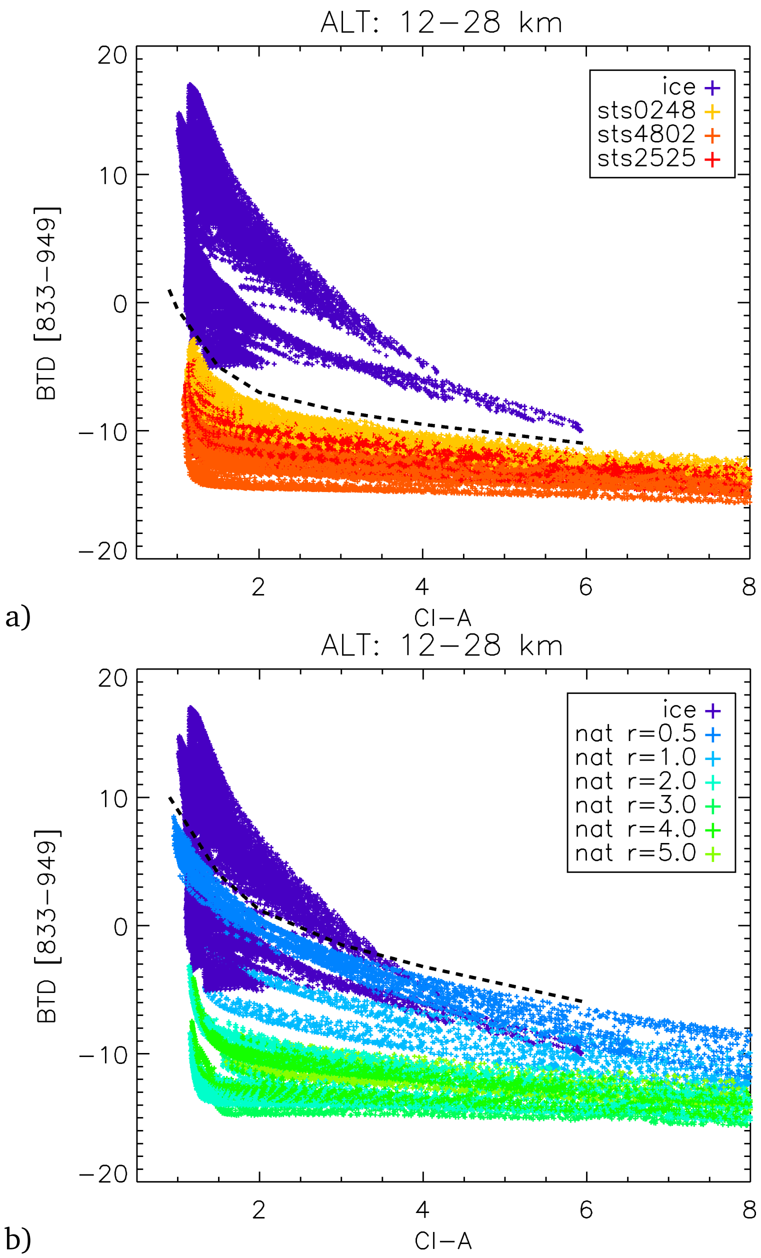

Figure 4.7: Brightness temperature difference (BTD) between the IMW 832.3 - 834.4 cm^{-1} and the IMW 947.5 - 950.5 cm^{-1} versus cloud index (CI-A) (788.2 - 796.25 cm^{-1}/ 832.3 - 834.4 cm^{-1}). Panel a): Separation between ice (dark blue) and STS of different compositions (red and orange). The notation STS0248 stands for 2 % HNO_3 and 48 % H_2SO_4. Panel b): Separation between ice and NAT particles (green to blue) with different mean radii (0.5 - 5 µm) and a width $\sigma = 1.35$ of the log-normal distributions. The separation lines are shown as dashed black lines. The cloud index called CI-A (cloud index of the MIPAS A-band) is equal to CI_S. The plot is taken from Spang et al. (2012)

4.4.2. Results for CRISTA-NF

The results for the CRISTA-NF measurements during the first five flights of the RECONCILE aircraft campaign are displayed in Fig. 4.8. The measurement data are filtered in the same way as described in Sec. 4.3. The different flights are shown colour coded and the two separation lines ice/STS and ice/NAT determined by Spang et al. (2012) are depicted as a solid black line and a dashed black line, respectively.

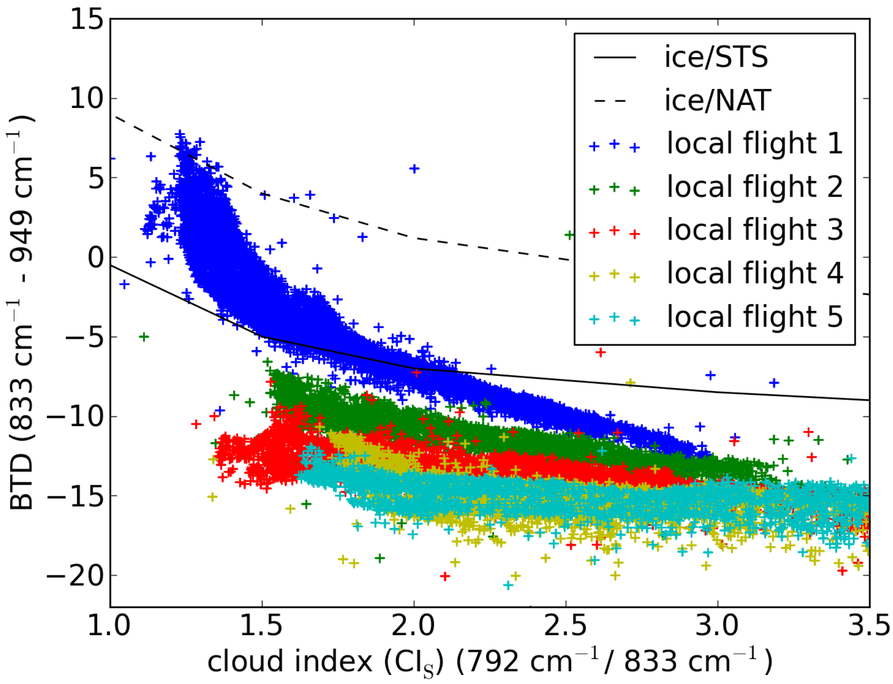

Figure 4.8: Brightness temperature difference (BTD) between the IMW 832.3 - 834.4 cm^{-1} and IMW 947.5 - 950.5 cm^{-1} versus cloud index (CI_S) (788.2 - 796.25 cm^{-1}/ 832.3 - 834.4 cm^{-1}) for the first five CRISTA-NF measurement flights during RECONCILE. The different flights are shown colour coded. The two separation lines ice/STS (solid black line) and ice/NAT (dashed black line) are taken from Spang et al. (2012).

Fig. 4.8 exhibits a clear difference between flight 1 and the other flights. All data points of the local flights 2 to 5 are below the separation line for ice/STS and no ice was observed during this flights. Together with the results of Sec. 4.3 this leads to the conclusion that the polar stratospheric clouds observed in the flights 2 – 5 consisted either of STS or contained larger NAT particles with radii larger than 3 µm.

For flight 1 the results are completely different. A large part of the data points are in the area between the two separation lines. These data points are either caused by ice or by small NAT particles. Since small NAT particles (radii less than 3 µm) can be excluded according to the results presented in Sec. 4.3, the remaining possibility to produce such brightness temperature differences is the presence of ice. The location of the observed polar stratospheric ice cloud is further analysed in the following sections.

4.5. Observation of a polar stratospheric ice cloud during flight 1

The following section presents a detailed investigation of the ice observation separated for the different viewing directions of CRISTA-NF during flight 1. Furthermore, the location of the observed polar stratospheric ice cloud is analysed by means of meteorological data and confirmed by independent measurements.

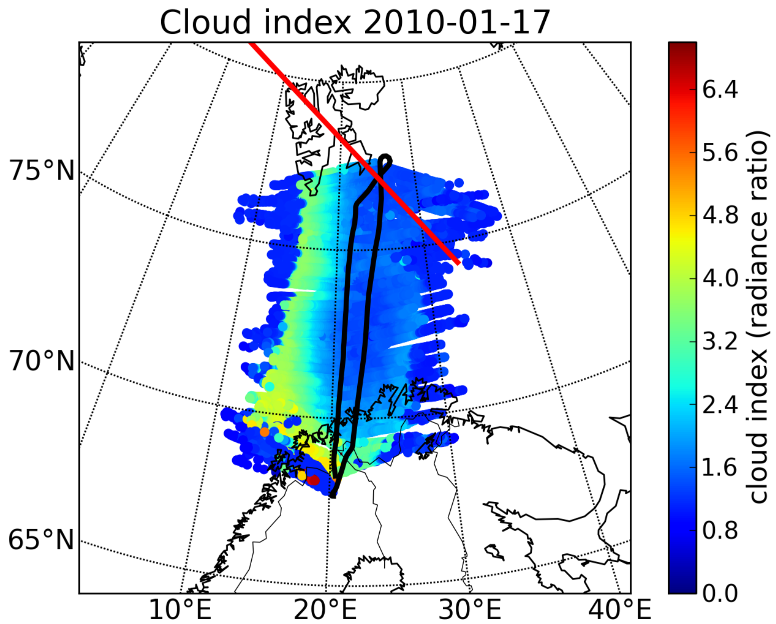

Figure 4.9: Latitude-longitude plot of the CRISTA-NF cloud index during RECONCILE flight 1. The flight path of the aircraft is marked by a solid black line and the red line shows the projected CALIPSO orbit at around 9:30 UTC.

The flight path of the M55-Geophysica during flight 1 is shown in Fig. 4.9. The flight started in Kiruna in northern direction (left leg) and after a turn at approximately 77.5°

North the aircraft flew straight back to Kiruna (right leg). The flight can be separated into two viewing directions of the instrument. During the first half of the flight CRISTA-NF viewed eastward and during the second half westward.

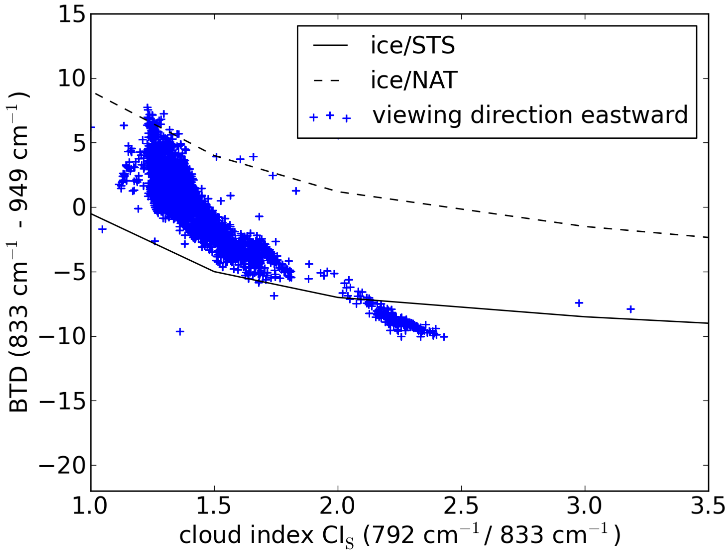

a)

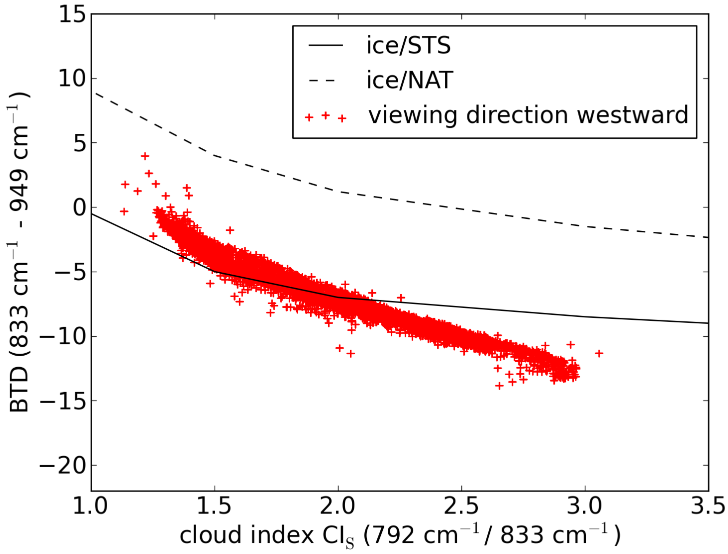

b)

Figure 4.10: Brightness temperature difference (BTD) (IMW 832.3 - 834.4 cm^{-1} - IMW 947.5 - 950.5 cm^{-1}) versus cloud index (CI_S) (788.2 - 796.25 cm^{-1}/ 832.3 - 834.4 cm^{-1}) for the CRISTA-NF measurement flight 1 separated for the viewing directions of the instrument (a) eastward and b) westward). The two separation lines ice/STS (solid black line) and ice/NAT (dashed black line) are taken from Spang et al. (2012).

Fig. 4.10 displays the results for flight 1 separated for the two viewing directions of the instrument (eastward a) and westward b)). During the first half of the flight (Fig. 4.10 a)) almost all data points are in the area between the two separation lines. The few points below ice/STS belong to measurements during the ascent of the aircraft at the beginning of the flight. Thus, nearly all measurements during the first half of the flight in the whole altitude range above the tropospheric clouds show a clear indication of ice.

During the second part of the flight (Fig. 4.10 b)) the situation is different and only part of the data points are above the ice/STS line. These data points belong to the upper tangent heights, whereas the measurements at lower tangent heights (below $\approx 15\,\mathrm{km}$) do not show any indication of ice.

A difference between the two viewing directions in terms of cloud detection is visible in the cross section of the CRISTA-NF cloud index (Fig. 4.3 a)) as well. In the second half of the flight low values of the CI are only visible at tangent heights between flight altitude and $\approx 15\,\mathrm{km}$, as well as in the troposphere (tropospheric clouds). Hence, no PSCs were observed at altitudes below $\approx 15\,\mathrm{km}$. In contrast to that, the CI values during the first half of the flight remain low in the whole altitude range.

The measurements in both parts of the flight, which are strongly influenced by PSCs (CRISTA-NF CI below ≈ 2.8), show also indication of ice. Since the PSCs might be located somewhere along the line of sight (see Sec. 4.1), additional examinations are necessary to make statements about the spatial distribution of the observed polar stratospheric ice cloud.

4.5.1. Location of the polar stratospheric ice cloud

In this section the temperature and water vapour distribution is analysed to obtain information about the potential of ice existence. This enables to locate the observed ice cloud.

Based on laboratory measurements Marti and Mauersberger (1993) found an empirical relation between the vapour pressure over ice and the temperature T_{ice} in the temperature range from 170 K to 250 K. The relation is given by

$$\log p = \frac{A}{T_{ice}} + B, \tag{4.3}$$

where p denotes the vapour pressure in Pa and T_{ice} the temperature in K. $A = -2663.5\,\mathrm{Pa/K}$ and $B = 12.537\,\mathrm{Pa}$ are two constants. At temperatures below the equilibrium temperature T_{ice} water ice can exist. Above T_{ice} ice evaporates, because the vapour pressure over ice is larger than the water partial pressure in this case (Peter, 1997; Peter and Grooß, 2012).

Here the water partial pressure during flight 1 is used to calculate the temperature T_{ice}. The difference between the temperature at a specific location and T_{ice} determines if ice can exist at this location. The temperature T_{an} is taken from ECMWF (European Centre for Medium-Range Weather Forecasts) operational analysis data (0.5° horizontal resolution, 6 hours time resolution). Furthermore, the water partial pressure is calculated from the ECMWF operational data for specific humidity and pressure. Because of the temperature and water vapour distribution during flight 1, the existence of ice is only possible above the flight altitude of the M55-Geophysica. Thus, CRISTA-NF viewed into the polar stratospheric ice cloud from below.

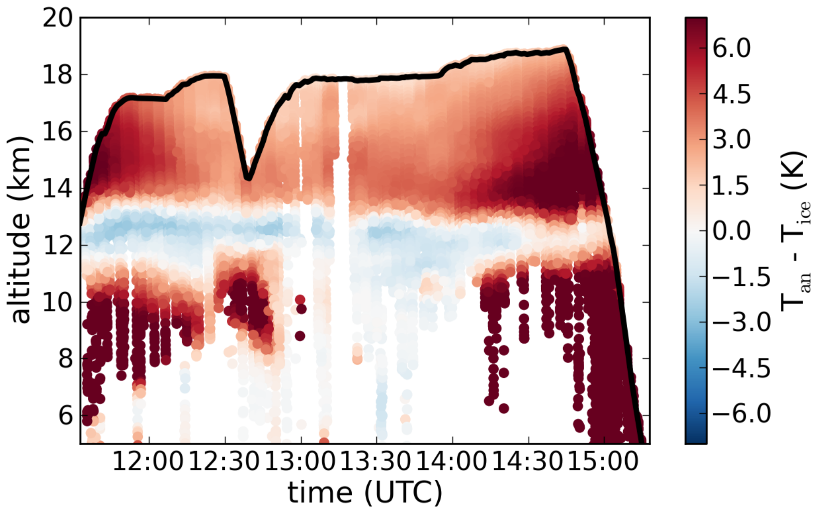

Figure 4.11: Difference between the ECMWF temperature T_{an} and the temperature T_{ice} (calculated according to Marti and Mauersberger (1993) (see equation 4.3)) at the tangent points of the CRISTA-NF measurements. The flight altitude of the aircraft is marked by a solid black line.

Fig. 4.11 shows the temperature difference between T_{an} and T_{ice} at the tangent points of the CRISTA-NF measurements. The ECMWF operational data are interpolated in time and space onto the tangent points. It is clearly visible that the ECMWF temperature is always higher than the temperature T_{ice}, except for the tropopause region. Hence, ice cannot exist at the CRISTA-NF tangent points in the altitude region above ≈ 13 km. Ice that had formed before would evaporate because of the too high temperatures.

Since the observed ice particles could be located somewhere along the LOSs, the whole area around the flight path is analysed. Additionally, the temporal evolution of the temperature and water vapour distribution has to be taken into account.

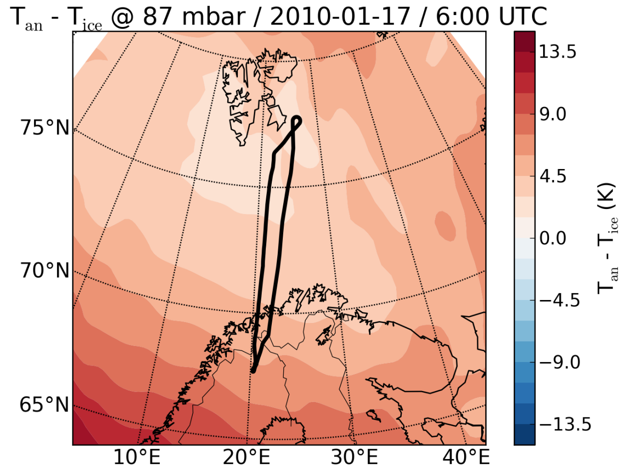

a)

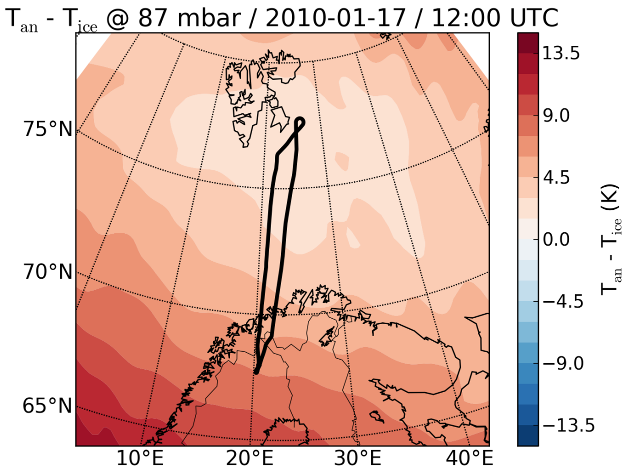

b)

Figure 4.12: Difference between the ECMWF temperature T_{an} and the temperature T_{ice} (calculated according to Marti and Mauersberger (1993) (see equation 4.3)) at 87 mbar (about 16 km) at 6:00 UTC (a)) and 12:00 UTC (b)) on 2010-01-17. The flight path of the aircraft is marked by a solid black line.

Fig. 4.12 shows the difference between T_{an} and T_{ice} at 87 mbar (around 16 km) at 6:00 UTC (before flight) and 12:00 UTC (beginning of flight). The temperature T_{an} is always several degrees higher than the threshold temperature T_{ice} at both times. Thus, the horizontal distribution of the temperature difference indicates that ice cannot exist in the whole region around the flight path at altitudes below flight altitude. Additionally, it can be excluded that

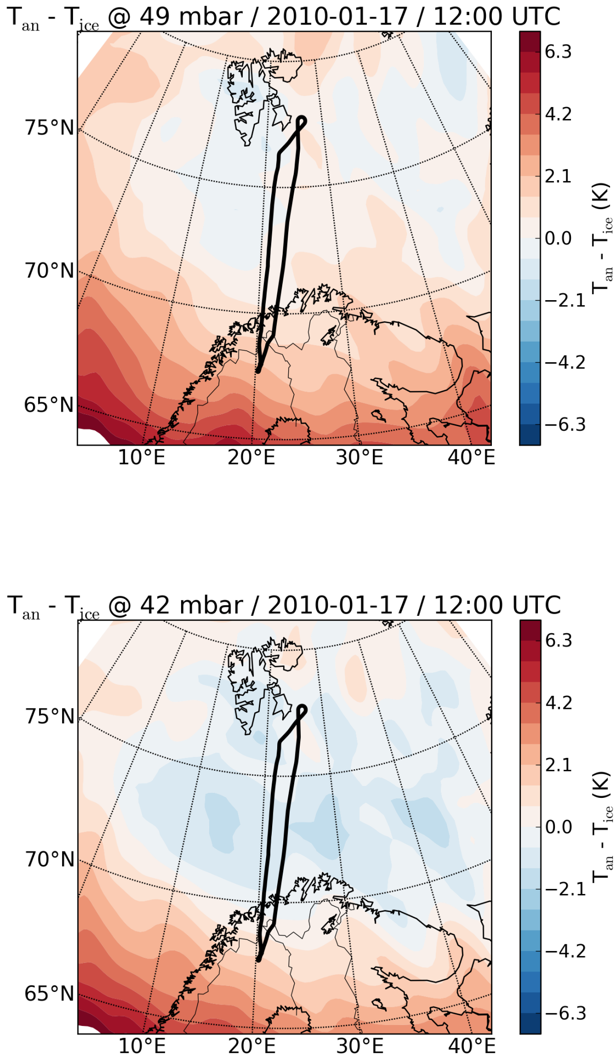

a)

b)

Figure 4.13: Difference between the ECMWF temperature T_{an} and the temperature T_{ice} (calculated according to Marti and Mauersberger (1993) (see equation 4.3)) at the two pressure levels 49 mbar (a)) and 42 mbar (b)) (approximately 20 km and 21 km, respectively)) at 12:00 UTC on 2010-01-17. The flight path of the aircraft is marked by a solid black line.

ice could exist before the flight.

By contrast the temperature and water vapour distribution above flight altitude shows that ice can exist at altitudes above ≈ 20 km. Fig. 4.13 displays the temperature difference between T_{an} and T_{ice} at the two pressure levels 49 mbar and 42 mbar (≈ 20 km and ≈ 21 km, respectively). In panel a) the temperature difference in some regions at higher latitudes is slightly negative, whereas panel b) shows negative values of a few degrees in a large area. These negative temperature differences indicate that ice can exist at these altitudes. Therefore, the presence of an ice PSC above the flight altitude is very likely.

4.5.2. Comparison with CALIOP measurements on CALIPSO

In order to confirm the presence of an ice PSC at altitudes above ≈ 20 km, independent measurements are taken into account. The CALIOP (Cloud-Aerosol LIdar with Orthogonal Polarization) instrument onboard the CALIPSO (Cloud-Aerosol Lidar and Infrared Pathfinder Satellite Observations) satellite provides backscatter and depolarisation measurements and enables the analysis of cloud and aerosol properties (e.g. Winker et al., 2010; Pitts et al., 2010).

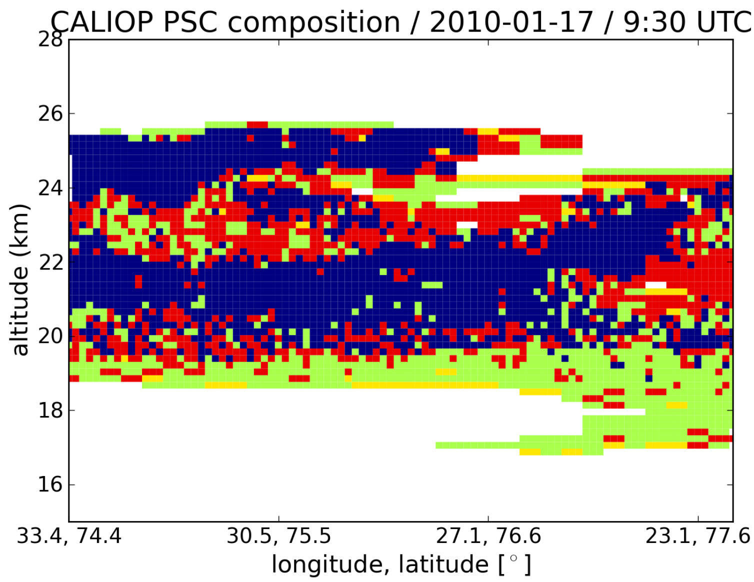

Figure 4.14: PSC observations during one CALIPSO orbit around 9:30 UTC on 2010-01-17 with horizontal spatial coincidence to the CRISTA-NF measurements. The different PSC types are displayed colour coded: ice in blue, STS in green, Mix1 in yellow, and Mix2 in red. CALIOP data: courtesy of M. Pitts

The detection of polar stratospheric clouds is based on the backscatter and depolarisation measurements of CALIOP. By means of a scattering ratio (total volume backscatter divided by the molecular backscatter coefficient) and the aerosol depolarisation ratio (perpendicular component divided by parallel component of aerosol backscatter) PSCs of different compositions can be identified and classified. Four different cloud types are distinguished: ice, STS, and two mixed STS/NAT clouds called Mix1 and Mix2, which contain NAT particles with lower and higher number densities, respectively. The data product is provided with a vertical resolution of 180 m in the altitude range from 30 km down to around 8.5 km and a horizontal spacing of 5 km. A detailed discussion of the PSC detection and classification is given by Pitts et al. (2009).

Fig. 4.14 shows the results of one CALIPSO orbit, which was located in the region of the CRISTA-NF measurements (compare Fig. 4.9 red line). Fortunately, the time difference between the CALIPSO orbit and the CRISTA-NF measurements in the same region is only 3 hours. The results show ice at and above altitudes around 20 km (blue colours), whereas below 20 km mostly STS PSCs (green) are visible. In the altitude range between 20 and 21 km a mixed phase cloud of ice, Mix2 (red), and STS (green) was observed. Above 21 km an ice PSC with a vertical extent of 2 to 3 kilometres is visible. Additionally, a second ice layer was observed at altitudes around 25 km during the first half of the presented time period. Hence, the CALIOP measurements confirm the presence of an ice PSC above the M55-Geophysica flight altitude.

4.5.3. Horizontal extent of the ice cloud

The observed situation is clearly different for the two viewing directions during flight 1. In the first half of the flight all measurements at tangent heights between flight altitude and the tropospheric cloud layer show the influence of ice in the spectra as well as PSCs. In the second part of the flight only the observations at higher tangent heights above about 15 km show these two characteristics. Furthermore, the horizontal distribution of the cold region at $\approx$ 21 km is asymmetric (see Fig. 4.13). The area of negative temperature differences east of the flight path is much larger and still existent in a larger distance to the flight path compared to the area west of the flight path. This asymmetric distribution seems to be in a good agreement with the differences in the observation of the polar stratospheric ice cloud for the different viewing directions of the instrument (see Sec. 4.5). Together this indicates a different horizontal extent of the ice cloud for the regions east and west of the flight path.

For the eastward viewing direction during the first half of the flight (see Fig. 4.3 a) and Fig. 4.9) all line of sights of measurements, which show a clear indication of an ice PSC, intersect the area with negative temperature differences east of the flight path at altitudes around 21 km. Due to the fact that tropospheric clouds are optically very dense the detection of a polar stratospheric cloud, which is located on the LOS behind a tropospheric cloud, is not possible. Thus, the measurements at tangent points below ≈ 13 km show only the presence of tropospheric clouds.

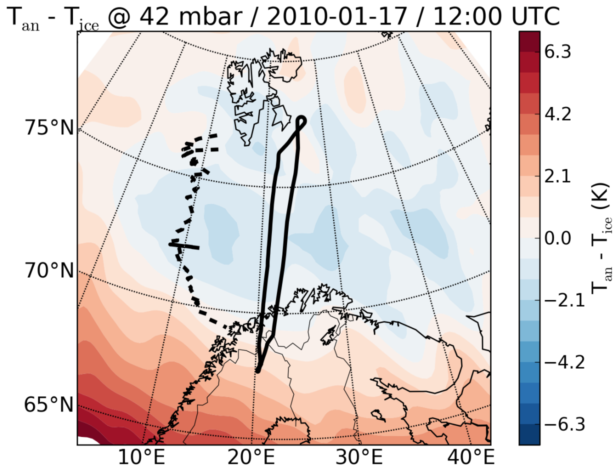

a)

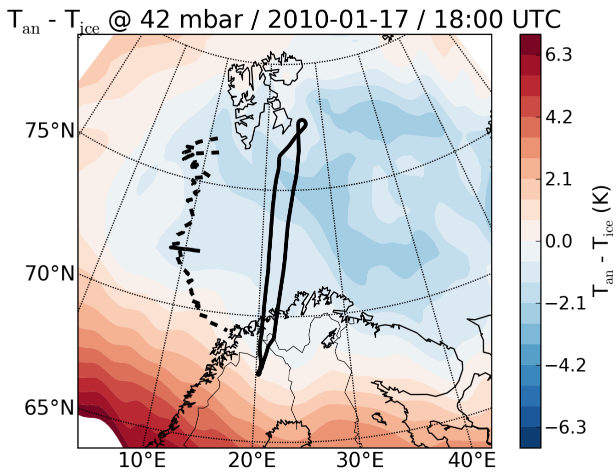

b)

Figure 4.15: Difference between the ECMWF temperature T_{an} and the temperature T_{ice} (calculated according to Marti and Mauersberger (1993) (see equation 4.3)) at 42 mbar (approximately 21 km) at 12:00 UTC (a)) and 18:00 UTC (b)) on 2010-01-17. The flight path of the aircraft is marked by a solid black line. Additionally, the intersection points of LOSs, which correspond to the lowest TPs showing ice influence during the second part of the flight, are displayed as a dashed black line.

To analyse the situation during the second part of the flight in more detail the intersection points of the CRISTA-NF line of sights with the polar stratospheric ice cloud are calculated.

The measurements showing both the influence of ice and the presence of a polar stratospheric cloud have a CI_S of ≈ 2.0 or lower (see Fig. 4.10 b)). Only the line of sights, which correspond to the lowest tangent heights showing this threshold cloud index value, are used for the analysis. The corresponding intersection points of these LOSs with the bottom end of the ice cloud have the largest horizontal distance to the instrument. These intersection points therefore give an estimate of the horizontal extent of the observed ice cloud west of the flight path. The observations of tropospheric clouds are excluded. In this simple approach the vertical distribution of the ice layer is assumed to be identical east and west of the flight path and the bottom end of the ice cloud is supposed to be 21 km (compare with CALIOP measurements in Fig.4.14).

Fig. 4.15 displays the temperature difference between T_{ice} and the ECMWF temperature T_{an} at 42 mbar ($\approx$ 21 km) at 12:00 UTC in panel a) and at 18:00 UTC in panel b). The flight path of the aircraft is shown as solid black line. Additionally, the intersection points of the CRISTA-NF line of sights with the 21 km layer during the second half of the flight are marked by a dashed black line. These intersection points are located at about 10° East. The measurements of CRISTA-NF during this part of the flight took place between 13:15 UTC and 15:00 UTC.

An eastward motion of the region with negative temperature differences of a few degree is clearly obvious in the two plots. Hence, the measurements of CRISTA-NF took place somewhere between this two states. For both times the lines representing the intersection points are located west of the regions showing the most negative temperature differences. In Fig. 4.15 b) almost the whole area west of the intersection points shows positive or only slightly negative temperature differences. The estimate of the horizontal extent of the polar stratospheric ice cloud, which is observable by CRISTA-NF, is therefore in good agreement with the observed temperature and water vapour conditions.

4.6. Summary and outlook

The presented chapter concentrates on the observation and analysis of polar stratospheric clouds during the RECONCILE aircraft campaign in Kiruna (Sweden). The CRISTA-NF instrument is very sensitive with respect to clouds, especially thin clouds like PSCs. Based on the different characteristics of the different PSC types in terms of their influence on the measured infrared spectra two analysis methods are presented to distinguish PSC types.

The first method allows for the detection of PSCs dominated by small NAT particles with radii $< 3\,\mu m$. These PSCs were not observed during the whole RECONCILE campaign. Nevertheless, it is possible that the observed PSCs contained a smaller number of small NAT particles. Other possible scenarios are, for example, the presence of only large NAT particles, which do not cause a spectral feature, or the presence of PSCs composed of both small and large NAT particles. In the latter case the influence of the cloud on the infrared spectrum would be dominated by the large particles. Thus, only PSCs composed of (or clearly dominated by) a large number of small NAT particles can completely be excluded.

The second analysis method is based on a brightness temperature difference and enables the differentiation of ice PSCs from other types of PSCs. During the first RECONCILE flight on January 17 a polar stratospheric ice cloud was detected. These cloud was located above the flight altitude of the aircraft as indicated by the temperature and water vapour conditions during the flight and confirmed by CALIOP measurements. By means of the CRISTA-NF measurements in combination with independent data from CALIOP the horizontal extent of the ice cloud was estimated. The ice cloud observed by CRISTA-NF extended to about 10° East.

The presented results show, that the application of the methods for the CRISTA-NF measurements leads to reliable results, albeit the radiative transfer simulations were performed for the MIPAS-ENV satellite geometry. However, the spectral feature caused by small NAT particles and the clear separation between ice and STS is independent of the viewing geometry.

During the RECONCILE campaign the M55-Geophysica carried more than 20 different scientific instruments, among others, different instruments to detect particles and two lidars (one upward and one downward looking), which measure backscatter and depolarisation signals of particles in the atmosphere. This instrumentation provided the unique opportunity to measure important information about the observed PSCs, like the particles size distributions and the vertical extent of the clouds. Hence, these measurements and related radiative transfer simulations will provide an excellent basis for the development and validation of analysis methods to examine the CRISTA-NF measurements in terms of polar stratospheric clouds in more detail. Furthermore, the CRISTA-NF measurements will help to investigate the composition of the polar stratospheric clouds, since the particle measurements aboard the M55-Geophysica only distinguish particle sizes but not particle types.

5. Retrieval

The infrared limb emission spectra measured by CRISTA-NF provide information on numerous atmospheric quantities such as trace gas volume mixing ratios, temperature, and pressure. The process that extracts this information is commonly denoted as retrieval. In this chapter the basic ideas of the retrieval technique and the setup used for the RECONCILE campaign are briefly presented (see also Ungermann et al., 2012).

The retrieval processor used in this work is the JUelich RApid Spectral SImulation Code version 2 (JURASSIC2; Ungermann, 2011). JURASSIC2 is an improved version of the original retrieval processor JURASSIC, which was used in several former studies (e.g Hoffman et al., 2009; Hoffmann and Alexander, 2009; Weigel et al., 2010). The quality of the retrieval results is assessed by means of different diagnostic quantities. For the first time, results exploiting the full potential in terms of the vertical sampling of the CRISTA-NF measurements are presented.

5.1. Retrieval technique

The infrared spectra, as they would be measured by CRISTA-NF for an atmospheric state, can be simulated by means of a forward model. This forward model F maps an atmospheric state $\boldsymbol{x}$, which here is a vertical profile, onto a vector of radiance values $\boldsymbol{y}$. The atmospheric state $\boldsymbol{x}$ describes the vertical distribution of temperature, pressure, trace gas volume mixing ratios, and aerosol. Such forward models, for example the line-by-line model RFM (Reference Forward Model; Dudhia et al., 2002), are commonly used in atmospheric science.

The JURASSIC2 forward model (JFM) by contrast is no detailed line-by-line model, but uses two approximative methods, the emissivity growth approximation (EGA; e.g. Weinreb and Neuendorffer, 1973; Gordley and Russell, 1981) and the Curtis-Godson approximation (CGA; Curtis, 1952; Godson, 1953). Both methods allow for the calculation of the total transmissivity along a LOS (line of sight), which is determined by means of a 3-D ray-tracing routine (Hase and Höpfner, 1999). The two approaches are based on look-up tables that store emissivity values for different atmospheric states and spectral regions. The RFM and the spectroscopic database HITRAN 2008 (HIgh resolution TRANsmission; Rothman et al., 2009) are used to calculate these look-up tables. All updates until August 2011 are taken into account

Additionally, the radiance results of both methods are combined by means of a regression scheme as described by Weigel (2009) in order to minimise the deviations from detailed line-by-line calculations. A combination of both methods leads to significant smaller systematic errors than one of the methods alone (e.g. Francis et al., 2006).

Since only the radiance values $\boldsymbol{y}$ are known from the CRISTA-NF measurements, the problem in the retrieval process is now to find the corresponding atmospheric state $\boldsymbol{x}$, that leads to those radiance measurements. Thus, this problem is the inversion of the forward model. This problem cannot easily be solved, since it is ill-posed, which means that no solution may exist or that the solution may not be unique. Furthermore, any solution is typically very sensitive to small changes in the measured radiance values caused for example by instrument noise. One way to handle these problems is to replace the original inverse problem by a well-posed approximation. Here, the problem is transferred to a minimisation problem and different constraints on the solution are added. Thus, the cost function J is now minimised to find the solution of the original problem. J is described by

$$\mathrm{J}(\boldsymbol{x}) = (\mathrm{F}(\boldsymbol{x}) - \boldsymbol{y})^{\mathrm{T}} \mathrm{S}_{\epsilon}^{-1} (\mathrm{F}(\boldsymbol{x}) - \boldsymbol{y}) + (\boldsymbol{x} - \boldsymbol{x}_{\mathrm{a}})^{\mathrm{T}} S_{\mathrm{a}}^{-1} (\boldsymbol{x} - \boldsymbol{x}_{\mathrm{a}}), \tag{5.1}$$

where the measurement error covariance matrix is denoted as S_{ϵ}, the a priori state as $\boldsymbol{x}_{\mathrm{a}}$ and the regularisation matrix as $\mathrm{S}_{\mathrm{a}}^{-1}$.

One can divide the cost function into two parts, on the one hand, the measurement term (first term in Eq. 5.1) and, on the other hand, a regularisation term (second term in Eq. 5.1).

The measurement error covariance matrix S_{ϵ} adds constraints on the solution by taking into account the relative size of measurement errors. For the setup discussed here, S_{ϵ} only considers the noise error of the instrument. An uncorrelated error budget of 1 % is used in the retrieval to approximate the true error covariance matrix, like it was done by Weigel (2009). The noise error of the detector is usually below this value of 1 % (e.g. Schroeder et al., 2009; Weigel, 2009), but the choice of a larger error accounts for other stochastic effects during the measurements. In this way uncertainties, e.g. due to minimal wavelength errors, a varying sampling grid of the spectrometer gratings influencing the numerical integration and uncertainties in the elevation angle of a measurement, are added to the detector noise. The measurement term therefore enforces a solution to be selected with a deviation between the measurements and the forward model results, which is as small as possible considering the constraints by the regularisation.

The regularisation term, including the a priori state $\boldsymbol{x}_a$, constrains the possible solutions to physically meaningful solutions. The a priori state $\boldsymbol{x}_a$ describes typical vertical profiles of the derived atmospheric quantities and therefore adds a priori knowledge about the atmosphere to the retrieval problem. Hence, solutions showing for example strong oscillations are practically excluded. Here, the matrix S_a^{-1} is set up by means of a combined Tikhonov regularisation of zeroth and first order (Tikhonov and Arsenin, 1977; Twomey, 1977), which means a constraint on the absolute values and the shape (smoothness) of the derived profiles.

The employment of both terms selects a solution with a minimum considering the constraints by the measurement errors as well as the constraints by taken into account a priori knowledge. The influence of the a priori knowledge on the solution can be analysed by diagnostic quantities (see Sec. 5.5). More detailed information about the used regularisation are given by Ungermann et al. (2012) and Ungermann (2011). The minimisation of J is performed by means of a truncated quasi-Newton iteration and an ad-joint model to calculate the Jacobian Matrix F' (Ungermann et al., 2010). An in depth discussion about this retrieval approach is given e.g. by Rodgers (2000) and Ungermann (2011).

5.2. Retrieval setup

The following section briefly presents the important information about the retrieval setup used for the RECONCILE campaign (see also Ungermann et al., 2012).

The retrieval for the CRISTA-NF measurements during RECONCILE uses only one of the CRISTA-NF detector channels so far, the low resolution spectrometer detector channel 6 (LRS 6). This detector channel covers the spectral range from 776.0 cm^{-1} to 868.0 cm^{-1} and exhibits spectral signatures of many relevant trace gases, like e.g. CO_2, $ClONO_2$, HNO_3, and CFC-11. Fig. 5.1 displays selected spectra of the LRS 6 measured during one altitude scan during RECONCILE flight 11.

By using the limb emission measurements of this detector channel, 11 atmospheric quantities can be derived: CFC-11, $ClONO_2$, HNO_3, O_3, CCl_4, and H_2O as primary targets and additionally aerosol, temperature, PAN, CFC-113, and HCFC-22. In addition to the retrieval setup of Weigel et al. (2010), the trace gas volume mixing ratios of CFC-11, $ClONO_2$, CFC-113, and HCFC-22 are derived. CFC-11 and $ClONO_2$ are included in the retrieval process because of their importance for the analysis of the polar winter atmosphere. Due to a significant improvement of the attitude information by using the MIPAS-STR AHRS measurements, it is no longer necessary to use CFC-11 volume mixing ratios measured by independent instruments to derive attitude information from the CRISTA-NF measurements (compare Weigel et al., 2010). CFC-113 and HCFC-22 are derived to reduce their systematic influence on the errors of the other trace gases, since climatological profiles of these trace gases are not accurate enough.

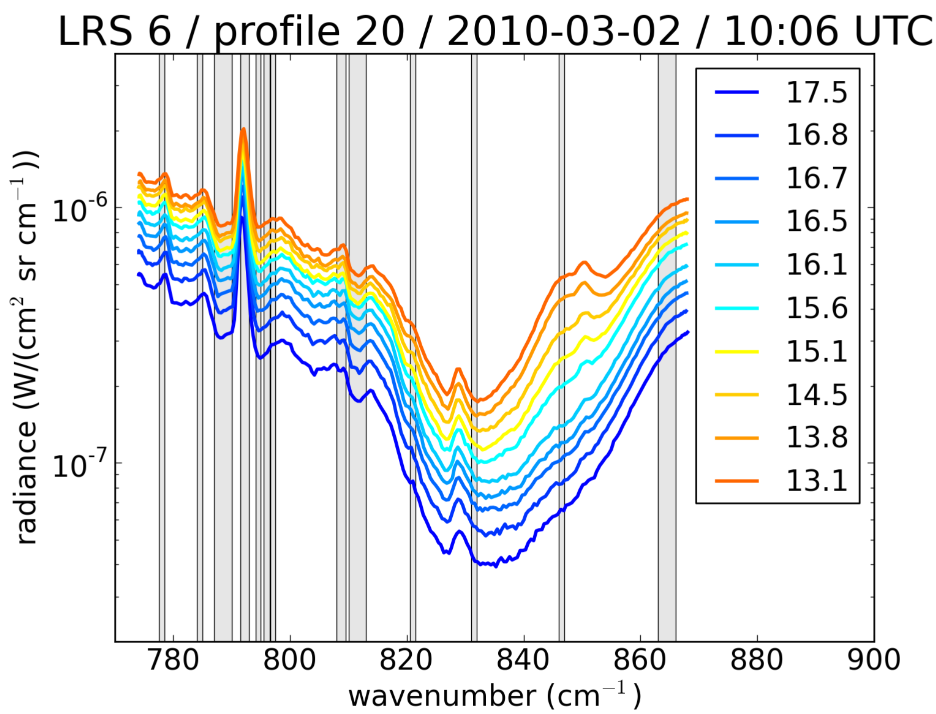

Figure 5.1: Selected CRISTA-NF spectra measured during the altitude scan 20 of the RECONCILE flight 11. The corresponding tangent height (in km) is shown colour coded and the IMWs used in the retrieval process are displayed as grey boxes.

The retrieval uses only the spectrally integrated radiance values in specific spectral windows, which are called integrated micro windows (IMWs). The whole retrieval process for the RECONCILE campaign is based on 13 of such IMWs. Most of them are selected in a way that one trace gas is the main contributor to the total radiance in the specific IMW. The employed IMWs are partly identical to the ones used by Weigel et al. (2010) and partly updated. The new IMW for $ClONO_2$ is similar to the spectral range used in former successful analyses of CRISTA satellite measurements (e.g. Riese et al., 1999). Tab. 5.1 displays the used IMWs and the corresponding main target. Additionally, the IMWs are shown as grey boxes in Fig. 5.1.

Table 5.1: Summary of the integrated micro windows used in the retrieval process and the corresponding main targets.

integrated micro window	spectral range (cm^{-1})	main target
1	777.5 - 778.5	O_3
2	784.0 - 785.0	H_2O
3	787.0 - 790.0	offset
4	791.5 - 793.0	temperature
5	794.1 - 795.0	PAN
6	795.5 - 796.5	O_3
7	796.6 - 797.5	CCl_4
8	808.0 - 809.0	HCFC-22
9	810.0 - 813.0	$ClONO_2$
10	820.5 - 821.5	HCFC-22
11	831.0 - 832.0	aerosol
12	846.0 - 847.0	CFC-11
13	863.0 - 866.0	HNO_3

The retrieval quantities are derived in different altitude regions. All quantities, which exhibit a maximum in their volume mixing ratios above the flight altitude, i.e. O_3, $ClONO_2$ and HNO_3, are retrieved in the altitude range between 0 and 60 km. The remaining quantities are retrieved in the range between 0 and 25 km. The employed retrieval grid in the altitude range up to 65 km has three different vertical spacings: 250 m below 20 km, 1 km between 20 and 30 km and 2 km above. The retrieval sampling in the altitude range of the CRISTA-NF measurements is therefore similar to the vertical sampling of the measurements.

Before the retrieval, the CRISTA-NF measurements are filtered and only measurements fulfilling certain criteria are used. Thus, profiles showing a change in the scanning direction (usually from top to down) during one altitude scan or large gaps in the vertical sampling are excluded. Furthermore, measurements during cloudy or optically dense conditions are sorted out. For the last requirement the cloud index (see Sec. 4.1) is used with a threshold value of 3.5.

Another criterion is used after the retrieval process to filter the retrieved profiles with respect to defects (mostly caused by strong aircraft movements). A retrieved profile $\boldsymbol{x}_\mathrm{f}$ is considered to be correct and without defects, if the fit of simulated spectra to the measurements is below the threshold value of 0.65. A smaller value indicates a good agreement between simulation and measurements, whereas a larger values indicates an erroneous profile. The fit is described in the first term of the cost function J (Eq. 5.1) and the criterion is therefore defined as $(\mathrm{F}(\boldsymbol{x})-\boldsymbol{y})^{\mathrm{T}}\mathrm{S}_{\epsilon}^{-1}(\mathrm{F}(\boldsymbol{x})-\boldsymbol{y}) < 0.65$. This value of 0.65 is ad-hoc chosen to get a compromise between too many filtered profiles and too many erroneous profiles.

Furthermore, the determined angle offsets between the CRISTA-NF instrument and the MIPAS-STR instrument (see Sec. 3.5 and App. A.4), which provides the accurate attitude measurements used for the LOS determination, are validated in the following way. Different retrievals are performed, each of them with another fixed elevation angle offset in the range from 0.1° to −0.1°. The elevation angle offset showing the best fits of the measurements to the simulations in average over the whole flight is assumed to be the correct additional offset. For the RECONCILE flights 10 and 11 the additional angle offset determined by this approach is 0.0°, which confirms that the offsets obtained during the calibration process are correct. Nevertheless, an error margin of ± 0.02° is assumed (details see Ungermann et al., 2012).

Table 5.2: Summary of the a priori information and background trace gases used in the retrieval process. The MIPAS reference climatology by Remedios et al. (2007) is used here. The ECMWF ERA-Interim data are provided every 6 hours with a horizontal resolution of 1.125°.

quantity	absolute values	standard deviation
O_3	climatology	climatology
H_2O	ECMWF ERA-Interim	climatology
HNO_3	climatology	climatology
CFC-11	climatology	climatology
CCl_4	climatology	climatology
$ClONO_2$	climatology	climatology
HCFC-22	climatology	climatology
CFC-113	climatology	climatology
PAN	zero profile	estimates by Glatthor et al. (2007)
temperature	ECMWF ERA-Interim	1 K
aerosol	climatology	climatology
pressure	ECMWF ERA-Interim	0.1%
CO_2	climatology (taken into account annual increase)	climatology
HNO_4	climatology	climatology
CFC-114	climatology	climatology
OCS	climatology	climatology

The forward simulation in the retrieval additionally includes contributions of the background trace gases CO_2, HNO_4, OCS, and CFC-114 to the radiance values. The latter gases are taken into account because of their minor, but not negligible, contribution to the total radiance, whereas the knowledge of the CO_2 volume mixing ratios is essential for the derivation of temperature. Tab. 5.2 summarises the sources for these background gases and for the a priori state $\boldsymbol{x}_{\mathrm{a}}$ employed in the regularisation.

Furthermore, the vertical FOV of CRISTA-NF ($\approx 3\,\mathrm{arcmin}$) is taken into account in the forward simulation and approximated by a Gaussian with a full width at half maximum (FWHM) of the same size (compare Riese et al., 1999).

The retrieval errors are estimated considering the errors caused by the instrument gain and offset, the forward model error, the spectroscopic line data uncertainties, and the uncertainties in the background gases.

The instrument gain uncertainty is determined by means of the black body emission measurements during the calibration procedure. A comparison between the calibrated radiance measured by CRISTA-NF and the theoretical radiance of the black body source leads to a gain uncertainty in the used detector channel LRS 6 of 2 %. This uncertainty describes the systematic relative instrument error. The value of 2 % is higher than in former studies by Weigel (2009), which is caused by the more complicated calibration with window compared to the calibration without window during the AMMA-SCOUT-O3 campaign (see Appendix A.2). The forward model errors are estimated by comparisons of the used forward model (JFM) and an exact line-by-line model (see App. B.2). All uncertainties of the retrieval results caused by such uncertainties in the radiance values are estimated in a linearised manner. The squares of all single errors are summed up and the square root of the sum is introduced as total error.

Furthermore, an additional error caused by the smoothing is calculated as

$$\mathrm{S}_{\mathrm{smoothing}} = (\mathrm{A} - \mathrm{I})\mathrm{S}_{\mathrm{a}}(\mathrm{A} - \mathrm{I})^{\mathrm{T}}, \tag{5.2}$$

where I denotes the identity matrix and A the averaging kernel matrix. In the following sections the combination of the total and the smoothing error is denoted as total+smooth error and used for the error estimates of the retrieval results. Additional information about the error derivation is given e.g. by Rodgers (2000) and Ungermann et al. (2012).

5.3. Retrieval results

In the following section the retrieval results for the CRISTA-NF measurements during one altitude scan during RECONCILE flight 11 (2010-03-02) are presented. The altitude scan was performed inside the polar vortex at about 10:45 UTC. The resulting trace gas profiles of the six primary retrieval targets are displayed in Fig. 5.2.

The retrieval results derived from the CRISTA-NF measurements are shown in blue and the a priori profiles employed in the retrieval process are shown in red. As expected, the derived volume mixing ratios of the different trace gases are only reliable in the altitude range between flight altitude (or the uppermost tangent height, if this is below flight altitude) and the lowest tangent height of the measurements. Below this lowest tangent height, the retrieved profiles of all trace gases are increasingly biased towards the a priori profiles, because of the missing measurements at these altitudes. Above flight altitude, the derived profiles follow mostly the shape of the a priori profiles and the absolute volume mixing ratios of the results get closer to the a priori volume mixing ratios. The vertical structure of the atmosphere above flight altitude cannot be derived as there is no sufficient contrast in sensitivity of the upward looking measurements to different layers in this altitude range. Only the total column above the aircraft can be derived to some extent.

Furthermore, the retrieval errors above flight altitude and below the lowest tangent height of a valid measurement largely increase, except for cases, where volume mixing ratios of nearly zero are present. This behaviour is caused by an increase of the smoothing error (see Fig. 5.7), since the a priori influence is increasing at these altitudes.

The volume mixing ratios of the gases CFC-11 and CCl_4 (Fig. 5.2 a) and e)) decrease with increasing altitude, as it is expected for trace gases with a tropospheric source. Both profiles clearly show lower volume mixing ratios and more small scale structures than the a priori profiles. The profiles of both trace gases agree well in terms of these small scale structures, like e.g. the local minimum around 12 km and the local maximum around 13 km, although the structures are more obvious in the CFC-11 profile because of the better vertical resolution (see Fig. 5.6 b)).

The volume mixing ratios of O_3, $ClONO_2$, and HNO_3 (Fig. 5.2 b), c), and d)) mostly increase with increasing altitude. Compared to the a priori profiles the volume mixing ratios of the derived profiles show mostly higher values and are more structured in the altitude range between flight altitude and the lowest tangent height of the measurements.

The derived profile for H_2O shows the same behaviour as the a priori profile, but lower volume mixing ratios at altitudes below around 11 km. Above 10 km the retrieved volume mixing ratios are nearly constant at 5 ppmv.

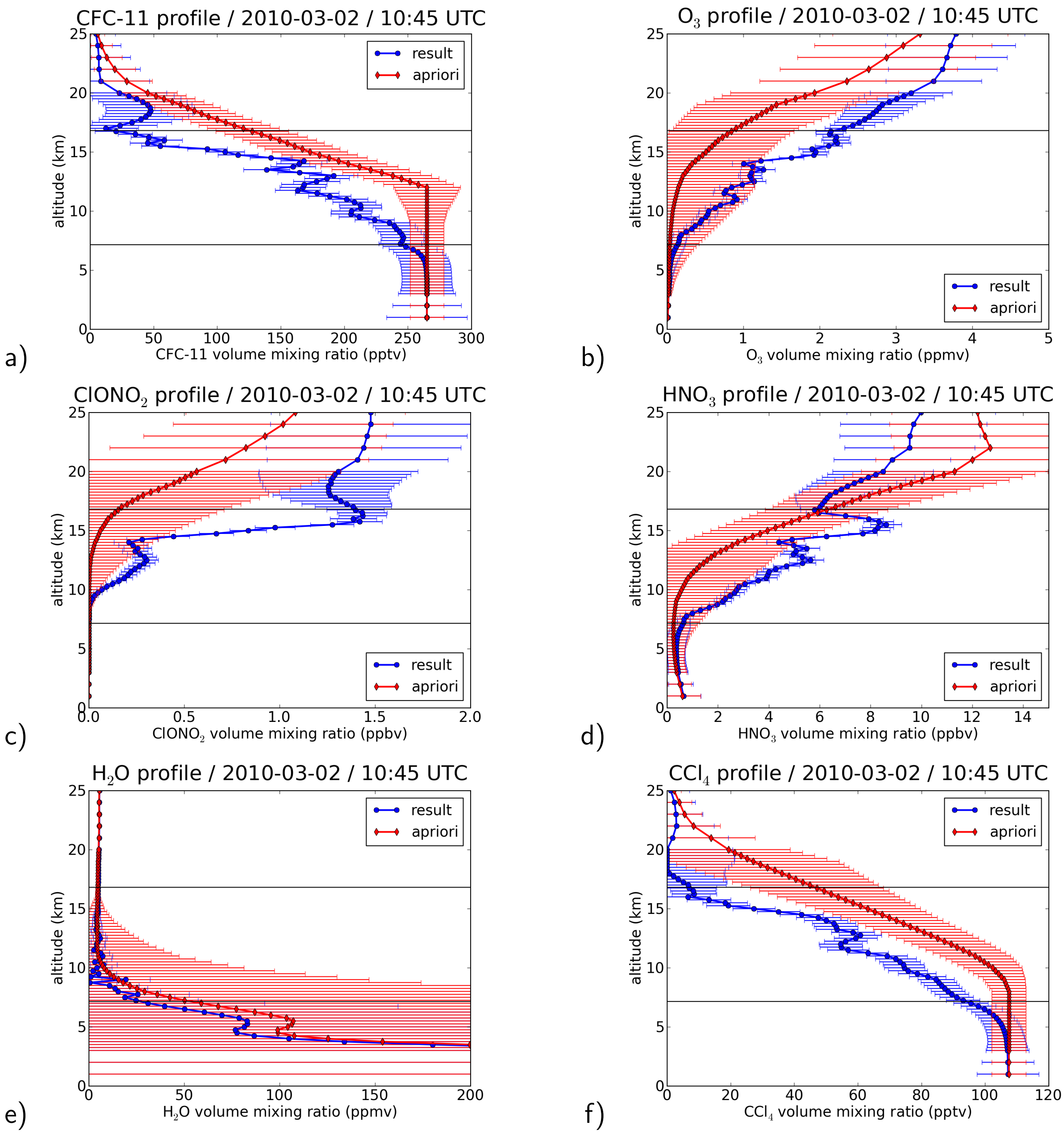

Figure 5.2: Retrieval results for the altitude scan 60 during RECONCILE flight 11 at 10:45 UTC on 2010-03-02. The CRISTA-NF retrieval results are displayed in blue and the a priori profiles in red. The black bars show the flight altitude and the lowest tangent point of a valid measurement. The error bars show the total+smooth error.

The a priori profiles are mostly taken from a climatology (compare Tab. 5.2) and therefore typically very smooth. In contrast to that, the retrieved profiles show numerous small scale structures illustrating the specific meteorological situation during the measurements. The differences between the retrieved and a priori profiles often exceed the errors. This indicates the independence of the retrieval results from the a priori state.

5.4. Exploitation of the full potential of the vertical sampling

In the retrieval process for the RECONCILE campaign all CRISTA-NF measurements during an altitude scan are taken into account and the full potential of the instrument with respect to the vertical sampling is exploited for the first time, which is a further development compared to former studies (e.g. Weigel, 2009; Weigel et al., 2010). This section presents analyses to assess the validity of this new approach and the reliability of the derived results.

The scanning direction of the CRISTA-NF spectrometer gratings is reversed after each spectrum. The two different spectra types are hereafter denoted as forward (fwd) and backward (bwd) spectra according to increasing or decreasing wavelength during the corresponding grating scan, respectively. In former studies by Weigel et al. (2010) the two spectra types were analysed separately because of detector relaxations. These detector relaxations denote a non-stationary behaviour of the detectors after illumination changes and are therefore dependent on the different scanning directions (e.g. Riese et al., 1999).

Fig. 5.3 shows altitude profiles of the spectrally integrated radiance in three representative IMWs for the laboratory and the post-flight wavelength calibration. The profiles are displayed separately for the two scanning directions to assess the impact of potential detector relaxations on the measurements.

Fig. 5.3 a) illustrates the two most important inadequacies of the laboratory calibration. On the one hand, the great difference between the integrated radiance for fwd and bwd spectra shows that both spectra types have to be calibrated separately. The use of one set of calibration parameters, like the one obtained from the laboratory calibration, for both spectra types is inadequate, since the relation between the output voltages of the gratings and the corresponding wavelength is extremely different for the two scanning directions. On the other hand, the comparison of the absolute values of the integrated radiance between the laboratory and the post-flight wavelength calibration exhibits a deviation as well, especially in the IMW 791.5 - 793.0 cm^{-1}. This deviation clearly shows that the absolute wavelength values of the laboratory wavelength calibration are incorrect as well. As a consequence the radiance is integrated over a somewhat shifted spectral region. Thus, a post-flight calibration is necessary to correct these deviations.

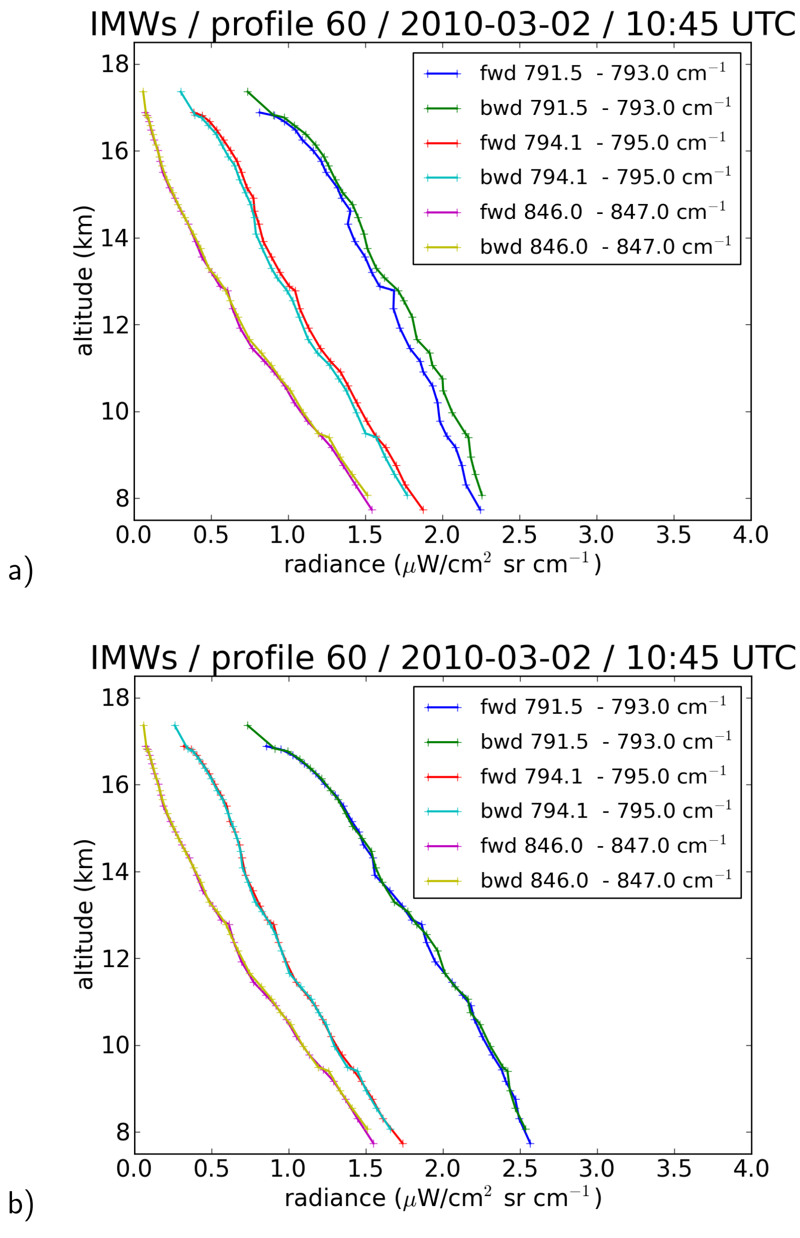

Figure 5.3: Altitude profiles of the spectrally integrated radiance in three representative IMWs, 791.5 - 793.0 cm^{-1}, 794.1 - 795.0 cm^{-1} and 846.0 - 847.0 cm^{-1}. The radiance values are displayed separately for forward and backward spectra. Panel a) shows the results for the laboratory wavelength calibration and panel b) after the post-flight wavelength calibration.

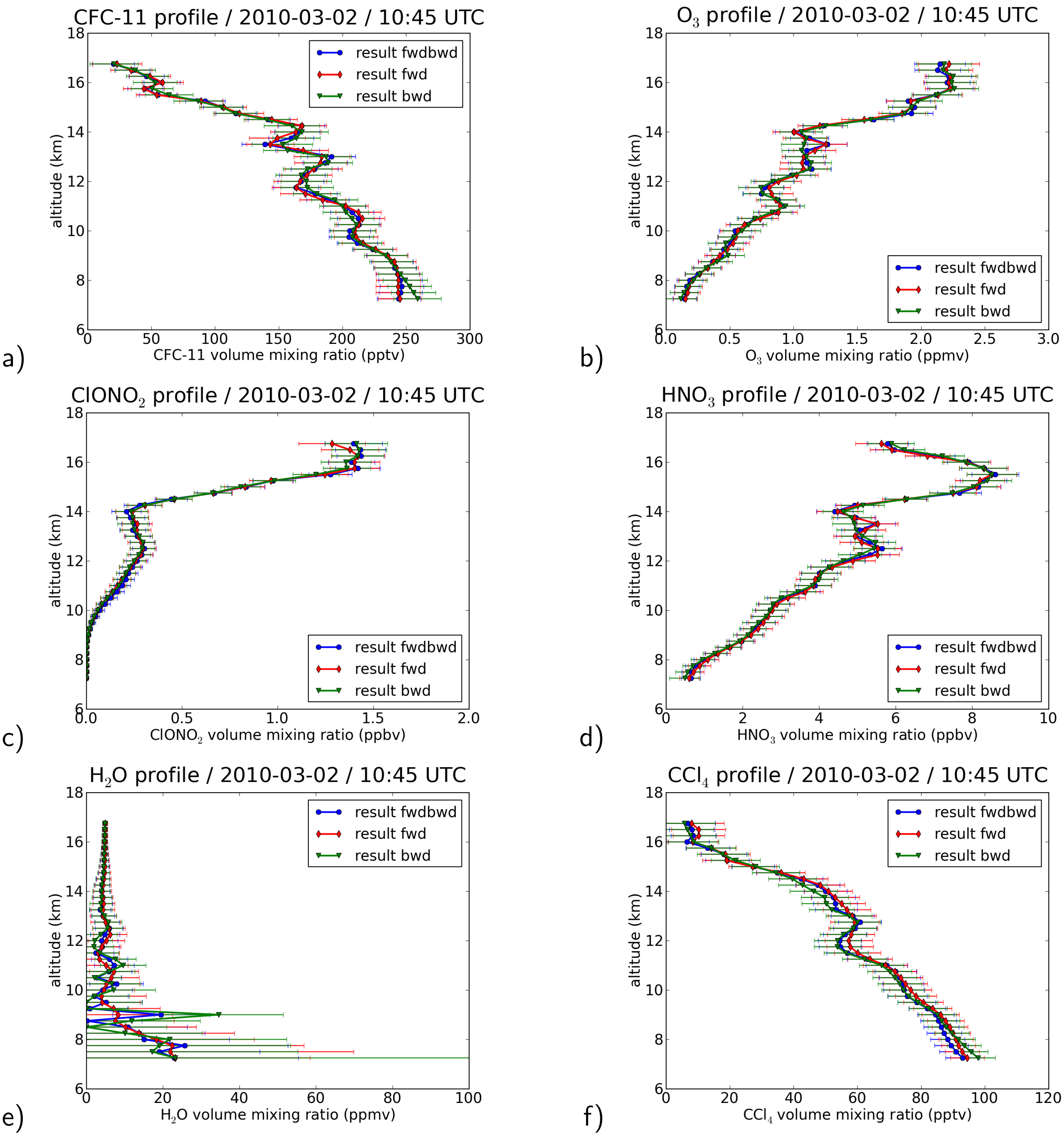

Figure 5.4: Comparison between the retrieval results for the combination of fwd and bwd spectra (blue) and the retrieval results for fwd (red) and bwd spectra (green) alone. The results are shown between flight altitude and the lowest tangent point of valid a measurement. The error bars show the total+smooth error.

After this refinement, only negligible systematic differences between forward and backward spectra are left (Fig. 5.3 b)) and no indication for detector relaxations is visible.

The altitude profiles of the integrated radiance in the remaining IMWs (not displayed here) exhibit a similar behaviour. Hence, the two spectra types can be used simultaneously in the retrieval process. In order to account for minimal remaining differences, one radiance offset per profile for each spectra type is derived during the retrieval process separately.

After these comparisons of the integrated radiance values the derived results are compared. For this purpose, two retrievals are performed, one using only measurements of forward spectra and one only those of backward spectra.

Fig. 5.4 displays the results of these different retrievals separately. Additionally, the retrieval results for the combination of forward and backward spectra are displayed. All three retrieval results show nearly the same volume mixing ratios for the six primary retrieval targets in the altitude range between flight altitude and the lowest tangent height of the measurements and agree well within the errors. Most of the differences occur in regions, where structures with a small vertical extent are present indicated by local maxima or minima. The measurements of forward and backward spectra have each a vertical sampling of $\approx 500\,\mathrm{m}$, but the two measurements grids are shifted by $\approx 250\,\mathrm{m}$. A small scale structure is therefore observed at different altitudes depending on the spectra type, which leads to slightly different retrieval results. All small scale structures are only fully captured in the results for the combination of forward and backward spectra. This illustrates that the best possible vertical resolution can only be achieved by using the combined data set and therefore the full vertical sampling of the measurements. Thus, the results derived from the combined data set are used in the following analyses.

5.5. Retrieval diagnostics

This section presents different diagnostic quantities to assess the quality of the retrieval results (see also Ungermann et al., 2012). The diagnostics follow largely the explanations by Rodgers (2000). Furthermore, the retrieval errors are analysed in more detail by showing the contributions of the single errors to the total error.

The retrieval result can be calculated by

$$\boldsymbol{x}_{\mathrm{f}} = \mathrm{A}\boldsymbol{x}_{\mathrm{t}} + (\mathrm{I} - \mathrm{A})\boldsymbol{x}_{\mathrm{a}} + \mathrm{G}\epsilon, \tag{5.3}$$

where I is the identity matrix, G the gain matrix, and ϵ the measurement error. The mathematical definition of A and G is given in App. B.1. Equation 5.3 is a linearisation, which implies that derived diagnostics are linearised as well.

The averaging kernel matrix A can be used to derive useful diagnostic quantities. The matrix A describes the contribution of the true atmospheric state $\boldsymbol{x}_{\mathrm{t}}$ to the retrieval result and is used to obtain information about the vertical resolution of the retrieval result and the measurement contribution, which is a measure for the a priori influence.

Neglecting a priori influence and measurements errors, the averaging kernel matrix maps the true atmospheric state $\boldsymbol{x}_{\mathrm{t}}$ onto the retrieval result $\boldsymbol{x}_{\mathrm{f}}$. Each row of the averaging kernel matrix gives the sensitivity of one derived retrieval quantity at one retrieval grid altitude to the full true atmospheric state. It therefore describes the contribution of different atmospheric layers to the result at a specific altitude.

An example of such averaging kernel matrix rows for the retrieval quantity CFC-11 is given in Fig. 5.5. The displayed averaging kernel matrix rows show only the contribution of the retrieved quantity itself, since this is the main contributor.

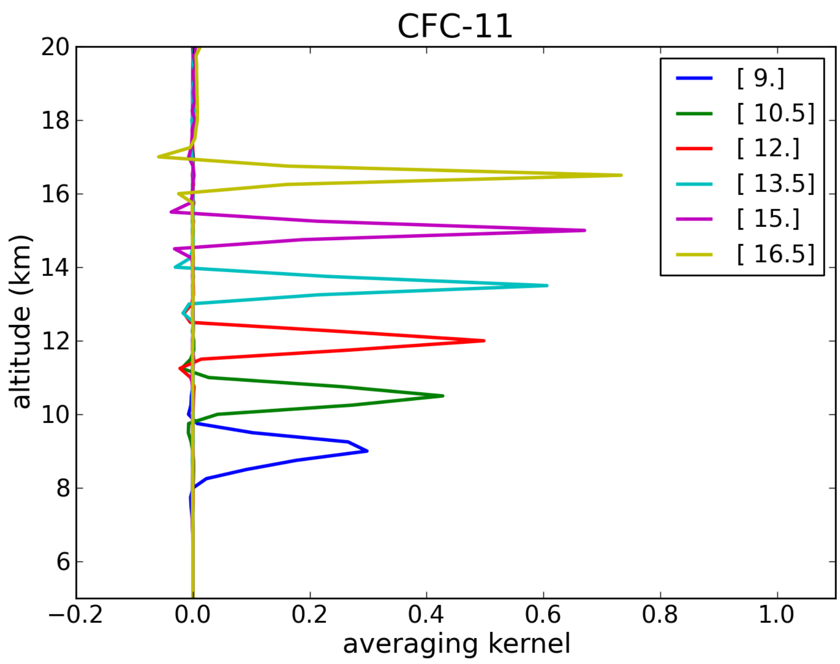

Figure 5.5: Selected averaging kernel matrix rows for the retrieval quantity CFC-11. The retrieval grid altitude (in km) is displayed colour coded.

The FWHM (full width at half maximum) of the averaging kernel matrix rows is introduced as a measure for the retrieval resolution. A narrow peak illustrates a good resolution of the retrieval result, since the result is mainly influenced by the true state at the corresponding grid altitude and the contribution of the adjacent atmospheric layers is comparably small. In Fig. 5.5 the narrowest peak occurs at the highest grid altitude of 16.5 km. Thus, the best resolution for CFC-11 is given just below flight altitude, where the vertical extent of the FOV is smallest. The FWHM is increasing with decreasing altitude, which illustrates the worsening resolution with decreasing altitude. The influence/contribution of adjacent atmospheric layers on/to the retrieval result is therefore increasing with decreasing altitude.

Another diagnostic quantity derived from the averaging kernel matrix rows is the measurement contribution. It is calculated as the sum over the averaging kernel matrix rows and gives a measure of the relative contribution of measurements and a priori to the retrieval result. The measurement contribution ideally is 1, which implies that the retrieval result is only determined by measurements. A measurement contribution of 0 by contrast implies that the retrieval result is only influenced by and thereby usually is equal to the a priori.

The derived measurement contributions for the different trace gases for one altitude scan during RECONCILE flight 11 are displayed in Fig. 5.6 a). The measurement contribution of the derived trace gases CFC-11, O_3, HNO_3, and CCl_4 in the altitude range between flight altitude and the lowest tangent height of the measurements is very close to 1, which indicates the good quality of the retrieval results and the independence from the a priori state. Above flight altitude and below the lowest tangent height of the measurements the measurement contributions show values, which differ extremely from 1, because of the increasing influence of the a priori state on the result at these altitudes.

In contrast, the measurement contributions of $ClONO_2$ and H_2O show a different behaviour. The measurement contribution of H_2O is nearly 1 between the lowest tangent height and 13 km. Above 13 km a bump with a maximum value of about 1.2 (at 14 km) is visible and the measurement contribution decreases above this bump with further increasing altitude. The measurement contribution of $ClONO_2$ shows a similar behaviour, but for the opposite altitude direction. At the lowest altitudes of the measurements the measurement contribution is nearly zero, followed by a steep increase to a maximum at 11.5 km. Above this altitude the measurement contribution stays mostly near 1. The very low values of the measurement contributions of H_2O and $ClONO_2$ are caused by very low signals at altitudes, where low volume mixing ratios of these trace gases are present. This indicates that the a priori knowledge is better than the information contained in the measurements. The bumps are most likely an artifact in the transition region between low measurement contribution and a measurement contribution of around 1.

One way to remove these bumps in the measurement contributions is to not retrieve

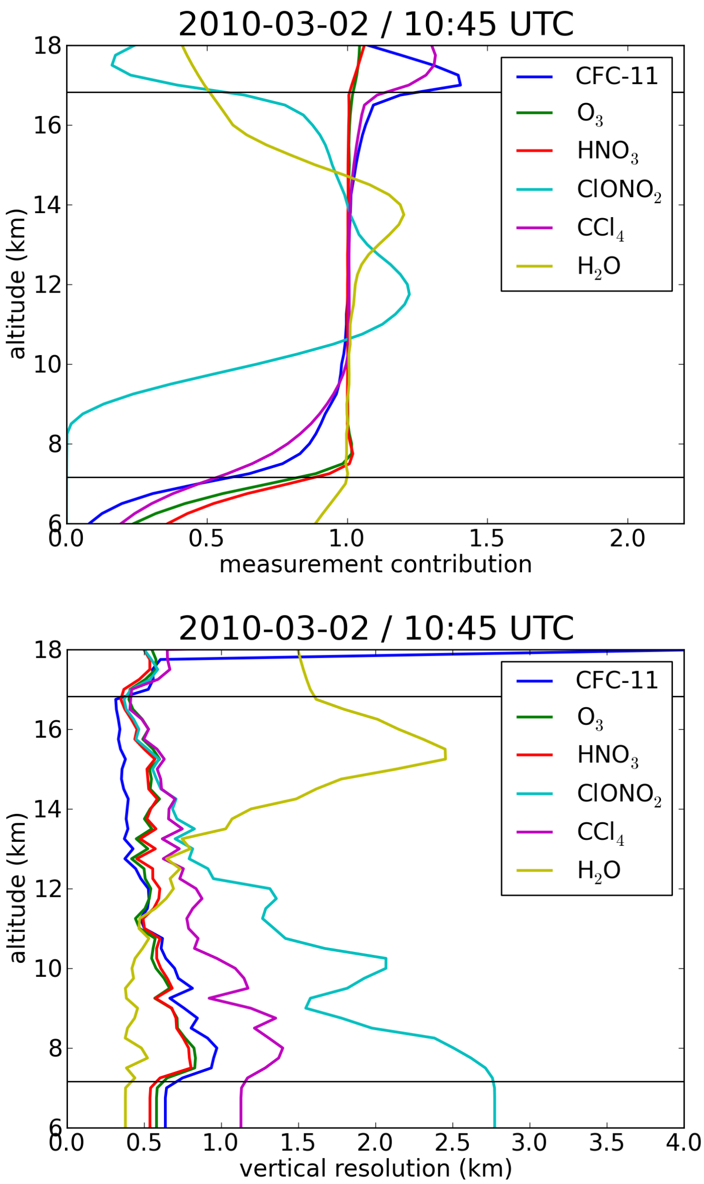

a)

b)

Figure 5.6: Measurement contribution (a)) and vertical resolution (b)) of the retrieval results for one altitude scan during RECONCILE flight 11 at 10:45 UTC on 2010-03-02. The different trace gases are displayed colour coded. The black bars show the flight altitude and the lowest tangent point of a valid measurement.

$ClONO_2$ below 10 km and H_2O above 12 km. Unfortunately, the abrupt change from derived volume mixing ratios to the a priori values causes artifacts in the results of the other trace gases. Hence, this possibility is not applied and the increase above 1 is accepted, since the volume mixing ratios of $ClONO_2$ and H_2O in the affected altitude range are close to the detection limit and therefore statistically insignificant.

The FWHM of the averaging kernel matrix rows is shown in Fig. 5.6 b). For the trace gases CFC-11, O_3, and HNO_3 the vertical resolution at flight altitude is better than 500 m and worsens with decreasing altitude to values still below 1 km in the whole altitude range of the measurements. The vertical resolution of CFC-11 is of unprecedented quality for a limb sounder: it is below ≈ 500 m for a few kilometres below flight altitude. The vertical resolution of CCl_4 is slightly worse with maximum values of about 1.5 km at the lowest altitudes. The overall worsening of the vertical resolution of these trace gases is a consequence of the larger vertical FOV at lower altitudes and a decrease of the transmissivity of the atmosphere with decreasing altitude.

The vertical resolution of $ClONO_2$ and H_2O is highly correlated to the measurement contribution of these trace gases. Hence, the vertical resolution is better than 1 km at altitudes, where a measurement contribution of nearly 1 is present. In the altitude range, where the measurement contribution is very low because of the lack of signal, the vertical resolution reaches maximum values of around 2.5 km.

The estimated total+smooth errors consists of many different contributions. Fig. 5.7 displays the retrieval errors of the retrieved trace gas volume mixing ratios separately for the different contributions. The total+smooth error is displayed in black and the single contributions in different colours. The uncertainties caused by the uncertainties in the spectroscopic line data of all trace gases besides the displayed one are neglected, since the contribution to the total+smooth error is very small. The displayed error caused by the uncertainties of the background gases considers all involved background gases (CO_2, HNO_4, CFC-114, OCS). The squares of the single errors, each caused by the uncertainty of a single background gas, are summed up and the square root of the result is displayed as the complete error caused by the background gases.

The proportion to which each error source contributes to the total+smooth error is nearly the same for all trace gases. The leading errors are the smoothing and the noise error, followed by the error caused by the uncertainties of the spectroscopic line data. The remaining errors have only a smaller contribution to the total+smooth error, whereby the error caused by the uncertainties of the background gases has the largest contribution. Above flight altitude and below the lowest tangent height of the measurements the total+smooth error is extremely dominated by the smoothing error, because of the increasing influence of the a priori state.

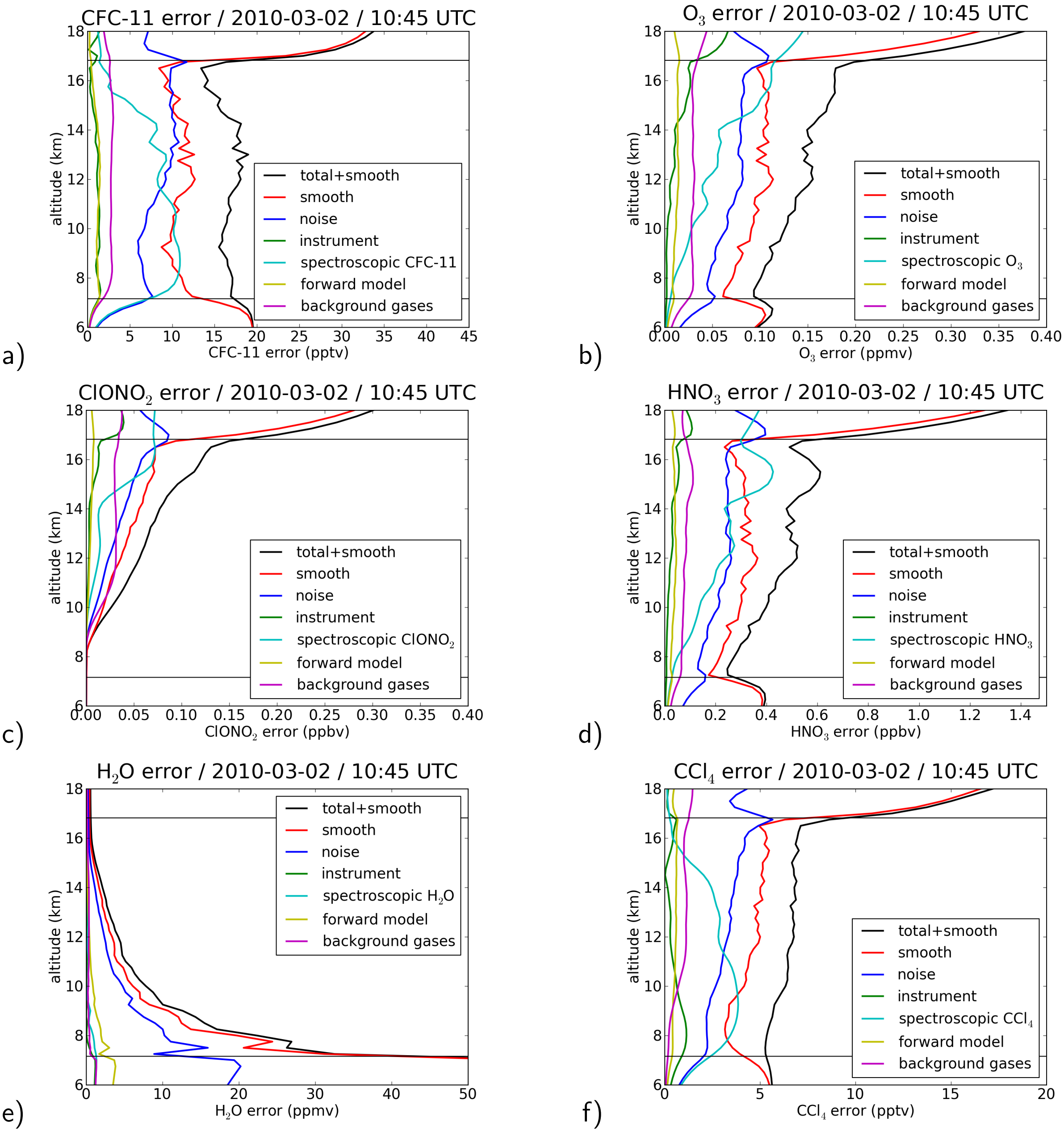

Figure 5.7: Errors of the retrieval results for one altitude scan during RECONCILE flight 11 at 10:45 UTC on 2010-03-02. The different errors, which contribute to the total+smooth error, are displayed in different colours and the total+smooth error in black. The black bars show the flight altitude and the lowest tangent point of a valid measurement.

6. RECONCILE Spitsbergen flights

At the beginning of March there was the opportunity to reach the polar vortex with the M55-Geophysica. Two flights were carried out on March 2, one from Kiruna to Spitsbergen and the second one back to Kiruna. In both flights the aircraft crossed the edge of the polar vortex and measurements inside as well as outside the polar vortex were performed. In this chapter the CRISTA-NF retrieval results for the trace gases CFC-11, ozone, $ClONO_2$, and HNO_3 for the flight back to Kiruna are presented and discussed. This flight took place under favourable measurement conditions (mostly cloud free and only few aircraft manoeuvres). Additionally, several interesting structures were observed by CRISTA-NF during this flight. The results for the other flight are presented in App. C.

CFC-11 is an inert trace gas with a lifetime of around 45 years in the stratosphere (e.g. Montzka, 2012). It is only photolysed in the stratosphere and not involved in any other chemical reactions. The volume mixing ratios (VMRs) of CFC-11 therefore decrease with increasing altitude in the stratosphere. On timescales of days to weeks, the distribution of CFC-11 is only determined by advection and mixing. CFC-11 is therefore well suited to study these types of processes.

Ozone is one of the most studied stratospheric trace gases, especially in the polar winter and spring time because of the ozone depletion inside the vortex (see Sec. 2.3).

$ClONO_2$ and HNO_3 are involved in the ozone chemistry and the de- and renitrification of the stratosphere and therefore of great interest. $ClONO_2$ is one of the important chlorine reservoir species in the stratosphere and the distribution is strongly related to the activation and deactivation of chlorine in the polar stratosphere in winter and spring (see Sec. 2.3). The distribution of HNO_3 depends among other things on the formation, sedimentation and evaporation of NAT particles and the corresponding de- and renitrifaction of the stratosphere (see Sec. 2.2). Both trace gases, $ClONO_2$ and HNO_3, therefore have an impact on the ozone chemistry and the proceeding ozone depletion in the polar vortex.

6.1. Situation during flight 11

This section concentrates on the situation during the second flight on March 2 (hereafter flight 11). The flight path and the measurement conditions in terms of cloud coverage are presented. Furthermore, the meteorological situation during the flight is analysed by means of potential vorticity.

6.1.1. Flight path and measurement conditions

Flight 11 started at the airport of Longyearbyen on Spitsbergen and ended in Kiruna (Sweden). Fig. 6.1 shows the flight path as projection onto the Earth's surface as a black line. The flight started at approximately 9:30 UTC in Longyearbyen towards northeast. After a turn at around 82° N the aircraft flew straight to Kiruna. Hence, flight 11 consisted of two different legs, one toward northeast and one southwards. Since CRISTA-NF looks perpendicular to the flight direction to the right side, this corresponds to the viewing directions of the instrument towards southeast and towards west, respectively.

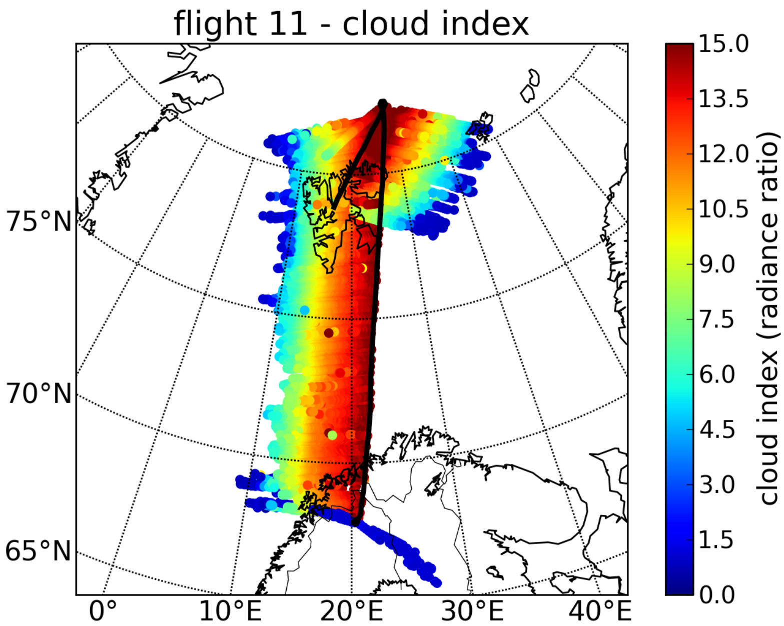

Figure 6.1: Latitude-longitude plot of the CRISTA-NF cloud index during flight 11. The flight path of the aircraft is marked by a solid black line.

Fig. 6.2 shows the flight altitude of the aircraft. The highest altitudes of around 19 km were reached at the end of the flight, because of less fuel and therefore less weight compared to the beginning of the flight.

The quantity displayed by coloured symbols in Fig. 6.1 and Fig. 6.2 is the cloud index (see Sec. 4.1). The CI is depicted at the tangent points of the CRISTA-NF measurements and shows the optical conditions during the measurements. A small value of the cloud index indicates the presence of clouds or optically dense conditions, whereas a large value shows cloud free conditions. A good threshold to differentiate between these two conditions is a value of 3.5.

In flight 11 cloud free conditions were present from flight altitude down to ≈ 8 km. Below 8 km tropospheric clouds were observed during the first half of the flight. The measurements during mostly cloud free conditions and the favourable flight path of the aircraft with only few aircraft manoeuvres give a good basis for highly precise retrievals. In the retrieval process all spectra showing a cloud index below 3.5 were flagged and not used (see Sec. 5.2).

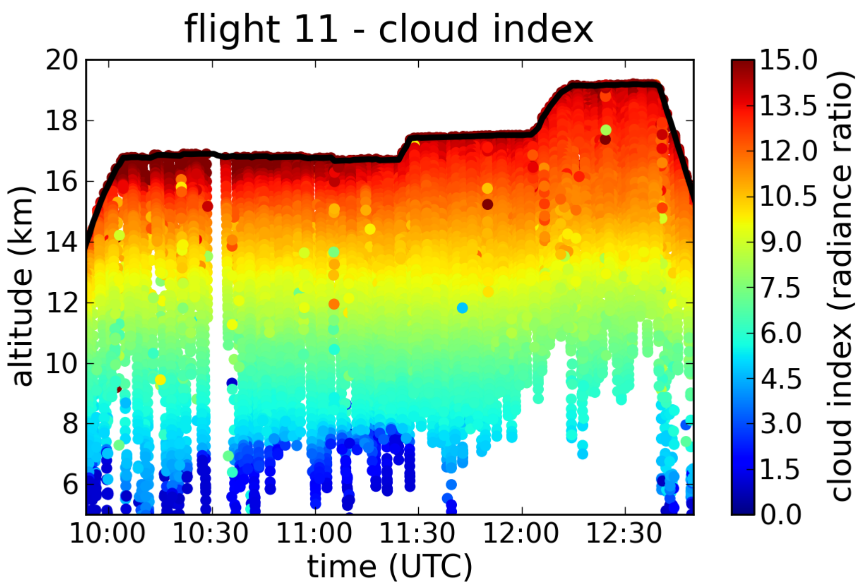

Figure 6.2: Vertical cross section of the CRISTA-NF cloud index during flight 11. The flight path of the aircraft is marked by a solid black line.

6.1.2. Meteorological situation

The potential vorticity (PV) is a very useful quantity to analyse the meteorological situation during a flight and to differentiate between different air masses, especially in the vicinity of the polar vortex (e.g. Hoskins et al., 1985; Nash et al., 1996; Müller and Günther, 2003). The potential vorticity is given by

$$\mathrm{PV} = -g(\zeta + f)\frac{\partial \theta}{\partial p}, \tag{6.1}$$

where g is the gravitational acceleration, ζ the relative vorticity, f the Coriolis parameter, θ the potential temperature and p the pressure. The potential temperature θ is defined as

$$\theta = T\left(\frac{p_0}{p}\right)^{R/c_p}. \tag{6.2}$$

T denotes the temperature, p_0 a reference pressure (1000 hPa), R the gas constant for dry air and c_p the specific heat at constant pressure. PV is a conserved quantity in the stratosphere for a few weeks and therefore useful to analyse dynamical processes. In general the potential vorticity increases from the equator towards the pole and has the highest values inside the polar vortex.

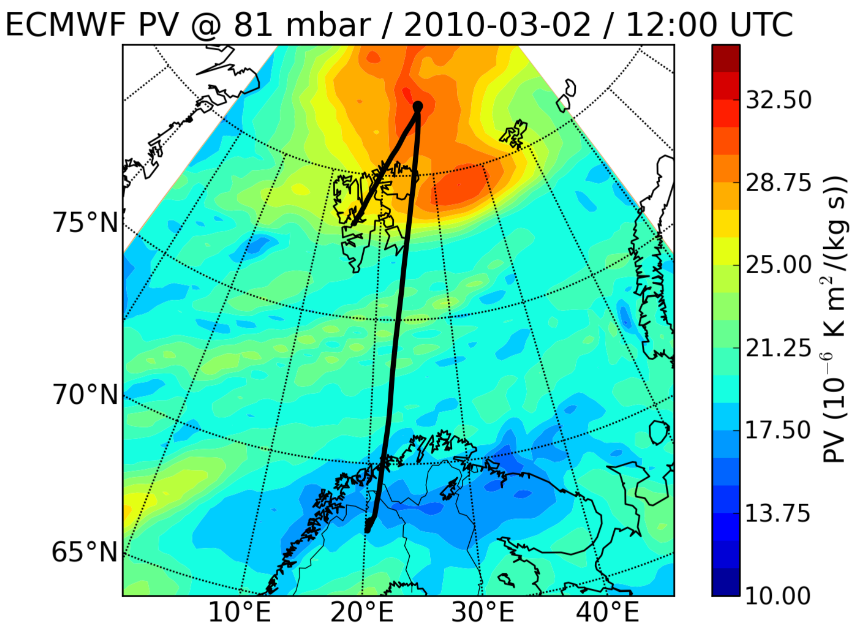

Figure 6.3: ECMWF potential vorticity at 81 mbar at 12:00 UTC on 2010-03-02. The flight path of the aircraft is marked by the solid black line.

Fig. 6.3 shows the potential vorticity at a pressure level of 81 mbar at 12:00 UTC. The flight path of the aircraft is displayed as black line. The pressure level corresponds to the atmospheric pressure at the flight altitude of the aircraft at the beginning of the flight ($\approx$ 17 km).

A large area with high values of potential vorticity is visible close to Longyearbyen and shows the polar vortex. Hence, the flight started inside the polar vortex and crossed the edge of the vortex on the way to Kiruna.

Due to the altitude dependence of potential vorticity, which is increasing with increasing altitude, the values of PV at different altitudes are not comparable to each other. Thus, a quantity called modified potential vorticity (mPV; Lait, 1994; Müller and Günther, 2003) is used here to analyse the conditions at the tangent points of the CRISTA-NF measurements.

6.1.3. Modified potential vorticity

The goal of the introduction of the new quantity modified potential vorticity is to remove the altitude dependence of PV. This can be achieved by scaling the potential vorticity with a quantity, which is decreasing with altitude, like the potential temperature θ:

$$\mathrm{mPV} = \mathrm{PV}\left(\frac{\theta}{\theta_0}\right)^{-\epsilon} \tag{6.3}$$

The values of the reference potential temperature θ_0 and ϵ used here are 420 K and 4.5, respectively, and therefore equal to the values used for the calculation of modified PV in CLaMS (see Sec. 7.3). The quantity θ_0 is introduced to obtain a dimensionless scaling factor. Detailed information about the derivation of modified PV and further analyses are given by Müller and Günther (2003). The authors showed that modified PV is a useful and valid quantity in the potential temperature range from 350 K up to 1400 K. All plots showing modified PV or related quantities are displayed in this range in the following sections. In the case of flight 11 a potential temperature of 350 K is nearly equivalent to an altitude of 10.5 km.

Fig. 6.4 displays the modified potential vorticity at the tangent points of the CRISTA-NF measurements for flight 11 in the altitude range from flight altitude down to 10.5 km. The values of mPV are calculated utilising ECMWF operational analysis data (0.5° horizontal resolution, 6 hour time resolution) following Eq. 6.3. The data are interpolated in time and space onto the CRISTA-NF tangent points.

Two distinct areas with high values of mPV can be seen. One area is located at the beginning of the flight between flight altitude and 15 km. The values of mPV are mostly higher than 20 PVU (potential vorticity units: $10^{-6}\,\mathrm{K\,m^2/(kg\,s)}$) in this area, which indicates the polar vortex. The second area with high values of mPV is located at the end of the flight below 16 km. The values of mPV between 16 and 20 PVU in this structure indicate air masses

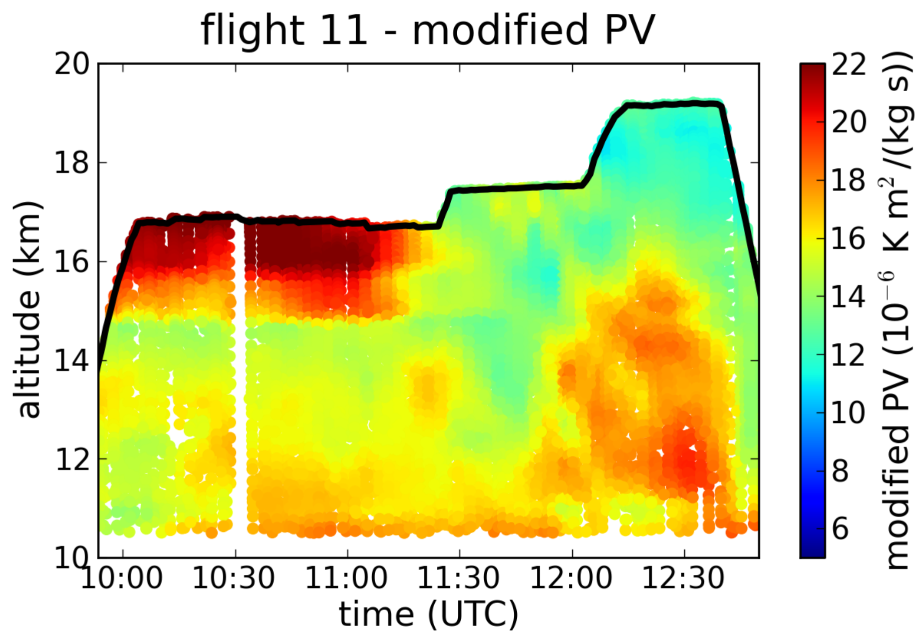

Figure 6.4: Cross section of modified PV at the CRISTA-NF tangent points for flight 11. The altitude of the aircraft is marked by a solid black line.

with a great amount of air masses originating from the polar vortex.

Apart from the structures with high mPV values, an area with significant lower values of mPV ($<$ 12 PVU) is visible below the flight path ($\approx$ 17 - 19 km) at the end of the flight. These low values indicate air masses, which probably originate from mid or low latitudes.

The distribution of mPV shows several structures and illustrates the interesting situation in terms of the dynamics of the atmosphere during flight 11.

6.2. CRISTA-NF retrieval results

In this section the retrieval results of the CRISTA-NF measurements for CFC-11, O_3, $ClONO_2$, and HNO_3 are presented. By means of these trace gases the origin of the observed air masses is analysed and situations illustrating de- and renitrification are shown. In order to assess the quality and reliability of the CRISTA-NF results, a comparison with independent measurements is presented first.

6.2.1. Validation

The payload of the M55-Geophysica contained more than 20 different scientific instruments during the RECONCILE aircraft campaign. Some of these instruments measure volume mixing ratios of trace gases, which belong to the CRISTA-NF retrieval targets. A comparison between those measurements and the retrieval results is therefore possible and presented in this section to validate the results (see also Ungermann et al., 2012).

Comparison with in-situ instruments

The two important in-situ instruments aboard the M55-Geophysica for the validation of the CRISTA-NF observations are the High Altitude Gas AnalyzeR (HAGAR; Riediger et al., 2000; Werner et al., 2010) and the Fast OZone ANalyzer (FOZAN; Ulanovsky et al., 2001).

HAGAR provides CFC-11 volume mixing ratios every ≈ 90 seconds at flight altitude and the FOZAN instrument provides ozone volume mixing ratios with a very high time resolution of 1 second. Both instruments performed well during the RECONCILE flight 11, which enables comparisons between the in-situ measurements and the retrieval results of CRISTA-NF for this flight.

Fig. 6.5 shows the CRISTA-NF retrieval results for ozone and the FOZAN measurements at flight altitude for flight 11. The measurements of the FOZAN instrument have a relative error of less than 10 % (Ulanovsky et al., 2001) and the total+smooth errors of the CRISTA-NF results are marked by error bars.

The measurements of both instruments mostly agree within the errors, but a small negative bias of the CRISTA-NF results is visible. However, this bias is usually not larger than the errors. Additionally, larger differences are obvious at some points, for example the deviation around 12:45 UTC, where FOZAN measures significant higher volume mixing ratios. These differences are caused due to the different measurement techniques of the instruments. FOZAN measures ozone volume mixing ratios at the location of the aircraft, whereas CRISTA-NF measures the integrated radiance along the line of sight. The derived volume mixing ratios for CRISTA-NF are therefore a spatial average around the tangent point of the measurement. Structures with a small horizontal extent are consequently not fully resolved.

Furthermore, a shift in the observation time of filaments is visible, for example around 11:15 UTC and 11:45 UTC. This time shift is a consequence of the horizontal distribution of the crossed filaments and the viewing geometry of CRISTA-NF perpendicular to the flight path to the right side.

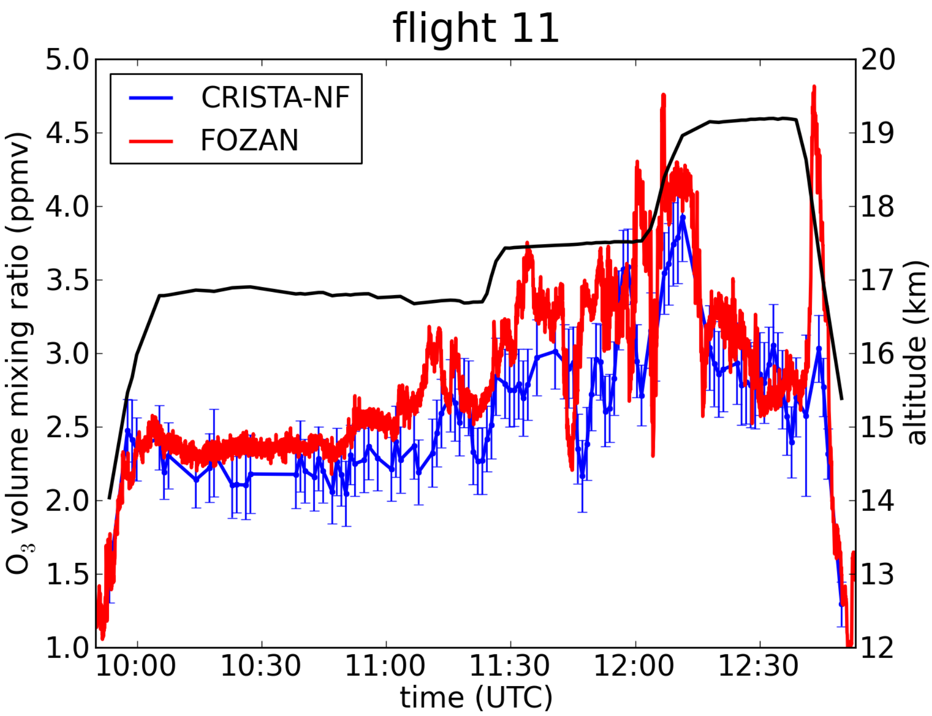

Figure 6.5: Comparison between the CRISTA-NF retrieval results for ozone (blue) and in-situ measurements by FOZAN (red) at flight altitude for flight 11. The errors bars for CRISTA-NF show the total+smooth error. The flight altitude is depicted as solid black line with an axis on the right side. FOZAN data: courtesy of A. Ulanovsky and F. Ravegnani

The horizontal distribution of ozone, displayed in Fig. 6.6, clearly shows that the observed filaments are not orthogonal to the flight path of the aircraft. Hence, the aircraft enters a filament and the change in volume mixing ratios is immediately observed by FOZAN. Because the largest part of the LOS of CRISTA-NF is outside the filament at this time, it takes some time before the LOS is mostly inside the filament and the change in volume mixing ratios is observed by CRISTA-NF as well.

Fig. 6.7 shows the comparison between the HAGAR CFC-11 measurements and the CRISTA-NF retrieval results for CFC-11. In general both measurements show the same behaviour and agree within the errors most of the time.

Similar to the comparison for ozone, an obvious time shift is visible, for example around 11:45 UTC and 12:00 UTC. As described above, the time shift is the consequence of the non-orthogonal filaments with respect to the flight path. This can be seen in the horizontal distribution of potential vorticity as well (compare Fig. 6.3).

Another difference is visible from 10:45 UTC to 11:15 UTC, where only HAGAR measures

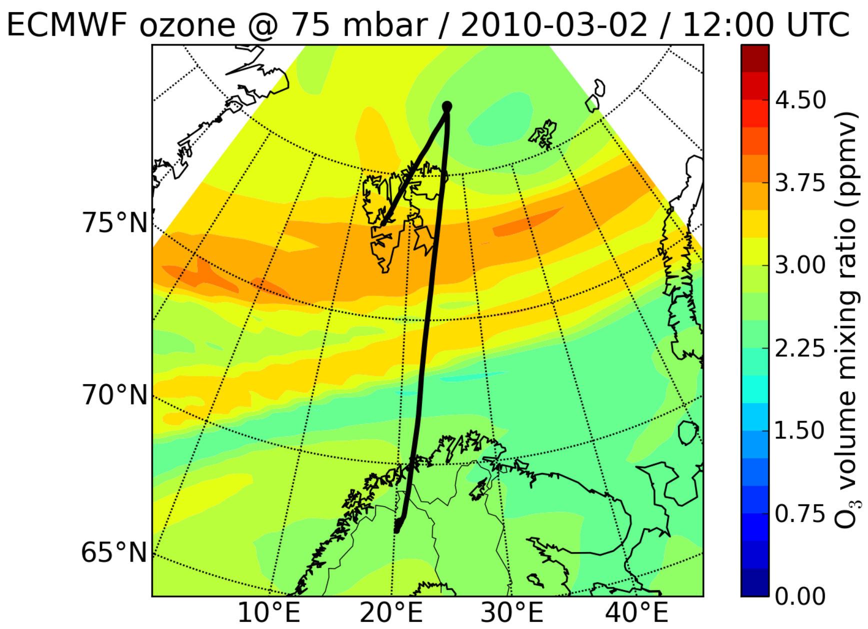

Figure 6.6: ECMWF ozone volume mixing ratios at 75 mbar at 12:00 UTC on 2010-03-02. The flight path of the M55-Geophysica during flight 11 is depicted as solid black line.

nearly constant CFC-11 volume mixing ratios. The steep increase at 11:15 UTC in the HAGAR measurements indicates the edge of the polar vortex. Thus, the M55-Geophysica left the polar vortex at around 11:15 UTC. Before leaving the polar vortex CRISTA-NF observed not only air masses from inside the vortex but the signal contained already a contribution from air masses from outside, which leads to the higher CFC-11 volume mixing ratios. The horizontal distribution of potential vorticity (Fig. 6.3) and the illustration of the viewing geometry (Fig. 6.1) confirms this. The polar vortex is indicated by high values of potential vorticity and CRISTA-NF viewed from areas with high values to areas with low values.

However, the overall good agreement of the in-situ measurements and the CRISTA-NF retrieval results shows that the CRISTA-NF retrieval results for CFC-11 and ozone are quantitatively and qualitatively reliable.

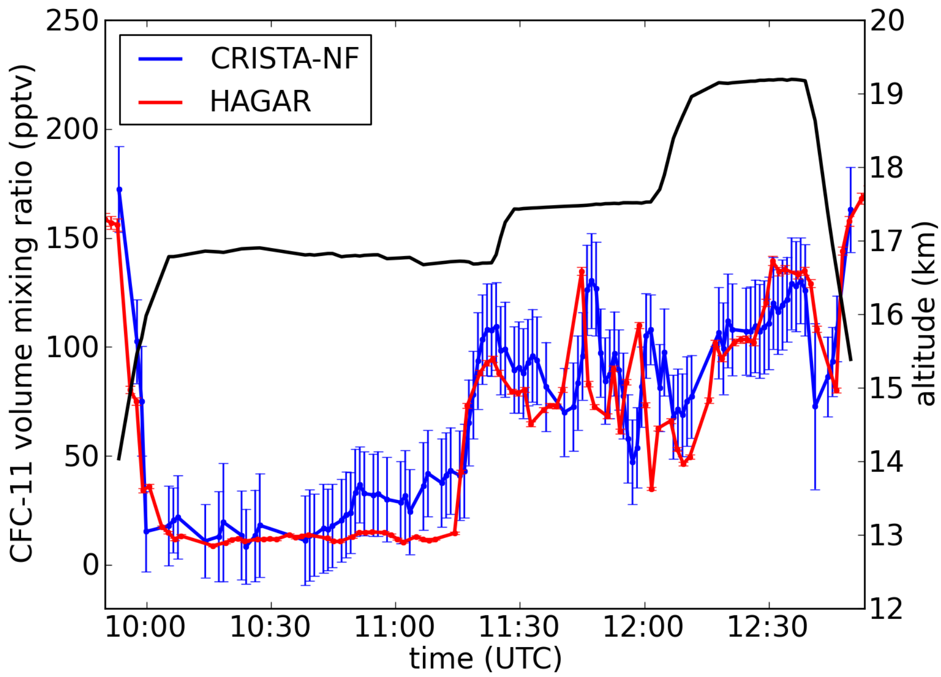

Figure 6.7: Comparison between the CRISTA-NF retrieval results for CFC-11 (blue) and in-situ measurements by HAGAR (red) at flight altitude for flight 11. The errors bars show the total+smooth error for CRISTA-NF and the absolute accuracy for HAGAR. The flight altitude is depicted as solid black line with an axis on the right side. HAGAR data: courtesy of E. Hösen and C.M. Volk

Comparison with other remote sensing instruments

In addition to CRISTA-NF, another infrared limb sounder, the Michelson Interferometer for Passive Atmospheric Sounding-STRatospheric aircraft (MIPAS-STR; e.g. Piesch et al., 1996; Keim et al., 2008), was operated aboard the M55-Geophysica. The volume mixing ratios of all CRISTA-NF primary retrieval targets shown in this chapter, namely CFC-11, ozone, $ClONO_2$, and HNO_3, are also derived from the MIPAS-STR measurements. The results of the two instruments for one selected altitude scan at 10:44 UTC during flight 11 are compared here.

Both instruments view perpendicular to the flight path to the right side and observe nearly the same air masses, albeit with a different sampling rate (vertically and horizontally) and a different FOV. The vertical sampling of MIPAS-STR is 1 km from flight altitude down to 8 km and 1.5 km below 8 km. According to the measurement mode, MIPAS-STR provides a horizontal sampling along the flight track between 25 and 45 km. The FOV is 0.44° (full cone) and therefore in the vertical much larger than the FOV of CRISTA-NF ($\approx 0.05°$). The retrieval grid for MIPAS-STR has a vertical spacing of 500 m. This decreased vertical sampling and the larger vertical FOV of MIPAS-STR lead to a vertical resolution of the retrieval results of ≈ 1 to 2 km, which is in many cases only half as good as the vertical resolution of the CRISTA-NF retrieval results (compare Sec. 5.5). The complete MIPAS-STR retrieval process is discussed in detail by Woiwode et al. (2012).

Fig. 6.8 shows the CRISTA-NF (blue) and MIPAS-STR (red) retrieval results for the trace gases CFC-11, O_3, $ClONO_2$, and HNO_3 in panels a) - d). The results are shown between flight altitude and the lowest tangent height of a valid measurement. Note that the MIPAS-STR retrieval error is estimated in a different way than for CRISTA-NF (e.g. no smoothing error; Woiwode et al., 2012).

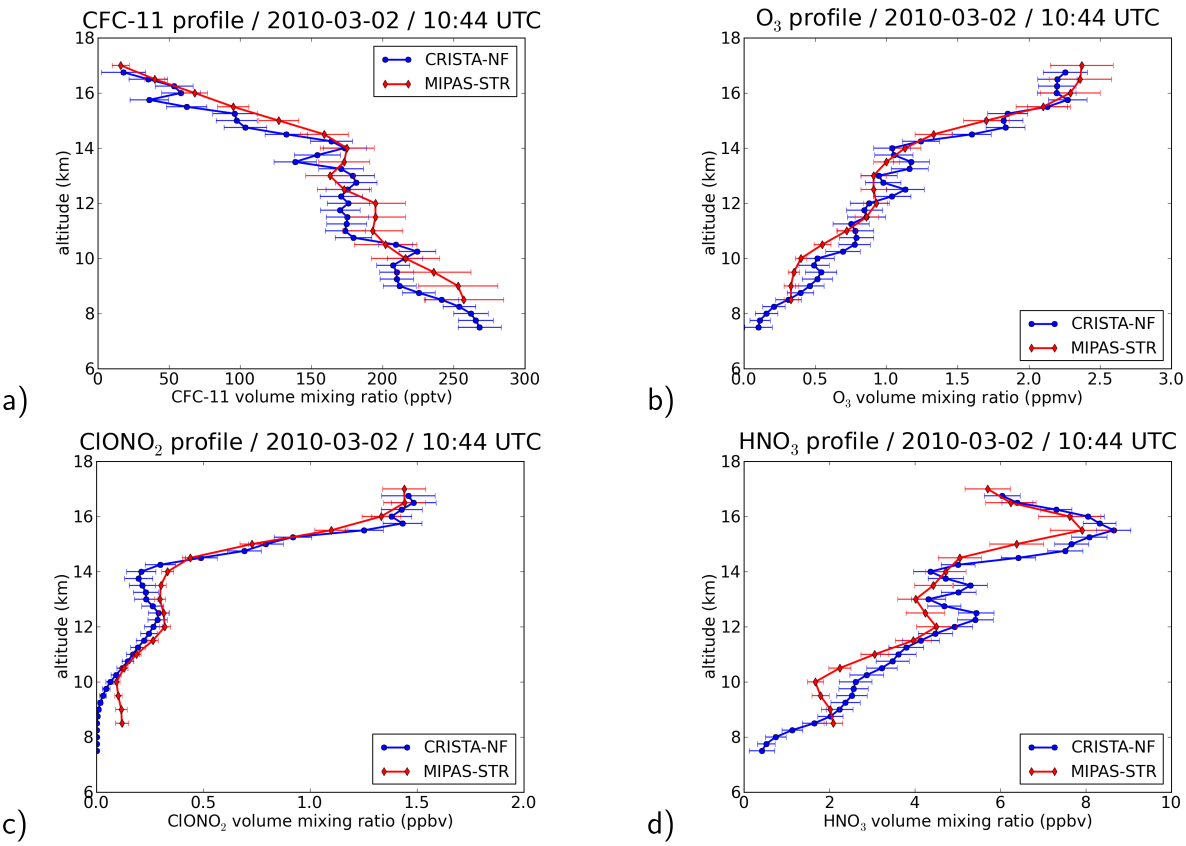

Figure 6.8: Comparison between the CRISTA-NF and MIPAS-STR retrieval results for CFC-11, O_3, $ClONO_2$, and HNO_3 (a) - d)) for one altitude scan at 10:45 UTC in flight 11. The errors bars show the CRISTA-NF total+smooth error and the MIPAS-STR retrieval error, respectively. MIPAS-STR data: courtesy of W. Woiwode and H. Oelhaf

The results for CFC-11 are displayed in panel a). Both results agree mostly within the error bars, albeit some differences are obvious. Between 16 km and 14.5 km CRISTA-NF measures slightly lower volume mixing ratios and the dip around 15.5 km observed by CRISTA-NF is not resolved by MIPAS-STR. In the altitude range between 14.5 km and 12 km both instruments observe several small scale structures indicated by local minima and maxima of the CFC-11 volume mixing ratios. But the vertical positions of the minima and maxima are different for both instruments and CRISTA-NF observes 2 local maxima and one local minimum, whereas MIPAS-STR only observes one maximum and one minimum. The altitude difference between a local maximum and the adjacent local minimum in the CRISTA-NF result is sometimes below 1 km, which is smaller than the MIPAS-STR vertical sampling and the vertical resolution of the MIPAS-STR results. This indicates that the differences are at least partly caused by the different sampling rate and FOV of the instruments. Nevertheless, both results in this altitude range mostly agree within the error bars. Below 12 km the CRISTA-NF results for CFC-11 are partly lower than the MIPAS-STR results. But the differences are usually smaller than the retrieval errors. In general, both retrieval results show absolute values in the same range and no systematic bias is visible.

Panel b) displays the retrieval results for ozone. Both depicted profiles agree well and the derived absolute values show no systematic differences. However, some small differences caused by small scale structures, which are not fully resolved by MIPAS-STR, are visible. The ozone profile of MIPAS-STR more or less looks like a smoothed version of the CRISTA-NF ozone profile.

The profiles for $ClONO_2$ are shown in panel c). The agreement of both instruments is excellent, except for the dip at 14 km, where CRISTA-NF observes slightly lower volume mixing ratios. But this is again a smoothing effect caused by the decreased vertical sampling and the larger FOV of MIPAS-STR.

Panel d) displays the results for HNO_3. The overall shape of the profile is captured nearly identically by both instruments, albeit the absolute values differ. CRISTA-NF observes higher HNO_3 volume mixing ratios compared to MIPAS-STR and maxima in the volume mixing ratios with a larger vertical extent.

Taking into account the different measurement geometry of both instruments the agreement between the CRISTA-NF and MIPAS-STR retrieval results is very good. This indicates that the CRISTA-NF retrieval results are quantitatively as well as qualitatively reliable.

6.2.2. Retrieval results for flight 11

The cross sections (2-dimensional curtain of all derived profiles) of the retrieved trace gases CFC-11, $ClONO_2$, and O_3 are shown in Fig. 6.9. The retrieval results are depicted on the retrieval grid of 250 m spacing in the altitude range from flight altitude down to the lowest tangent height of a valid measurement in the corresponding profile. Regions with different viewing directions of the instrument are separated by a dashed grey line. All following cross sections of retrieval results are presented in the same manner.

The corresponding total+smooth errors are displayed in Fig. 6.10. The range of the colour bar for the error is one tenth of the range of the colour bar for the result. Same colours at the same position in both plots therefore show a relative error of 10 %.

The total+smooth error for CFC-11 varies mostly between 15 pptv to 25 pptv and the relative error is typically between 10 and 15 %, even smaller than 10 % below 11 km. Only in the structures with very low CFC-11 VMRs, like the area at the beginning of the flight (see Fig. 6.9 a)), the relative error increases and reaches at some points at flight altitude 100 %. Nevertheless, the CFC-11 VMRs are reliable, as shown by the comparisons with the HAGAR and MIPAS-STR measurements (see. 6.2.1). The relative errors for $ClONO_2$ and ozone are mostly between 10 and 15 %, except for some regions, in which the derived VMRs are very low (blue colours in Fig. 6.9 b) and c)).

The cross section of CFC-11 (Fig. 6.9 a)) displays three distinct structures with low CFC-11 VMRs. Firstly, a large area in the first half of the flight between flight altitude and approximately 15 - 16 km showing extremely low CFC-11 volume mixing ratios is visible. Secondly, there are two additional structures with comparable low VMRs at the end of the flight. One of these structures is located at an altitude around 15 km and the second one at $\approx$ 17 km. Both are separated from each other by a thin layer showing high CFC-11 VMRs. This thin layer exhibits a vertical extent of 1 km or less, which is reliable with respect to the vertical resolution. The observation of such a layer illustrates the very high vertical resolution of the CRISTA-NF retrieval results, especially for CFC-11.

In the area at the beginning of the flight the CFC-11 volume mixing ratios drop below 20 pptv at the highest altitudes and are therefore significant lower than the volume mixing ratios outside this area at comparable altitudes. Taking into account the distribution of mPV (see Fig. 6.4), which shows the highest values (mostly greater than 20 PVU) in the same region, this confirms the presence of the polar vortex. As a consequence of the subsidence of air masses inside the vortex during winter and spring time (see Sec. 2.1), air masses with low CFC-11 VMRs are transported downward. This leads to the observed differences between

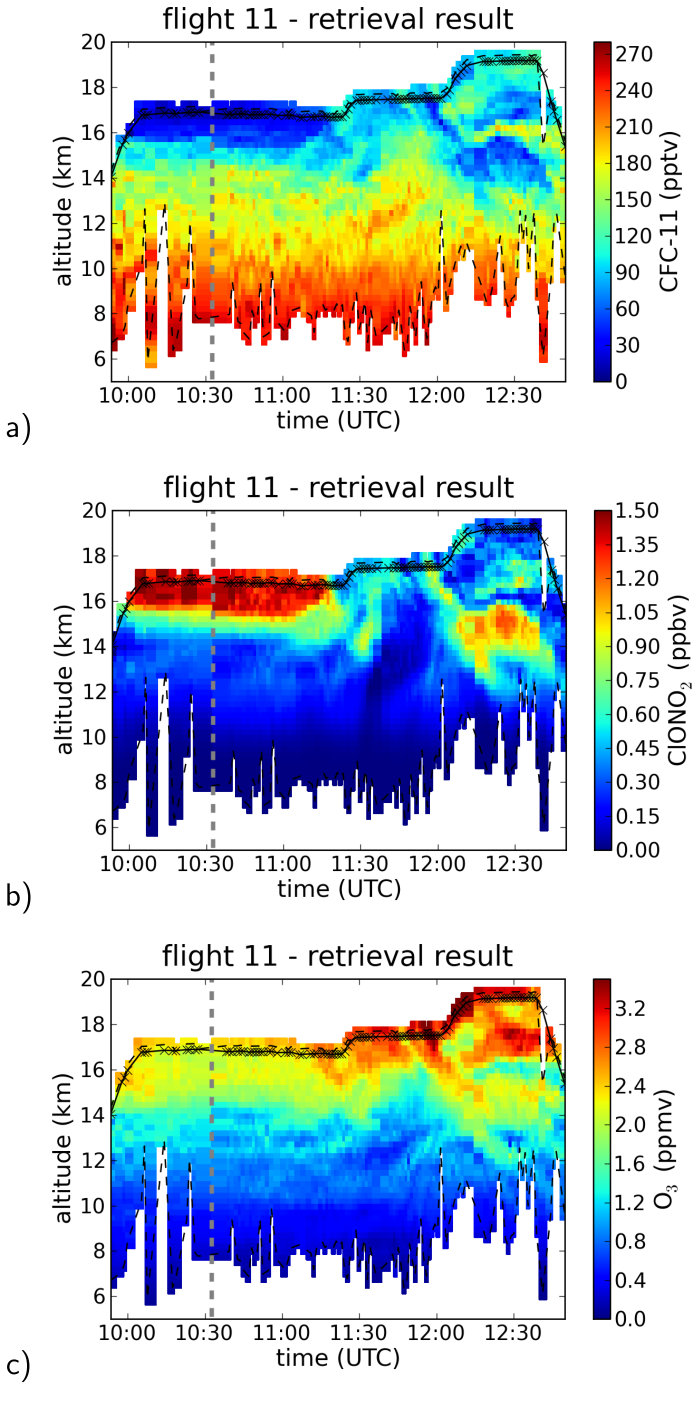

Figure 6.9: Retrieval results of the CRISTA-NF measurements for the trace gases CFC-11 (a)), $ClONO_2$ (b)), and O_3 (c)) for flight 11 . The solid black line shows the flight altitude and the dashed black lines the lowest and highest tangent height of a valid measurement. The position (time) of each profile is marked by a black cross. Different viewing directions of the instrument are separated by a grey dashed line.

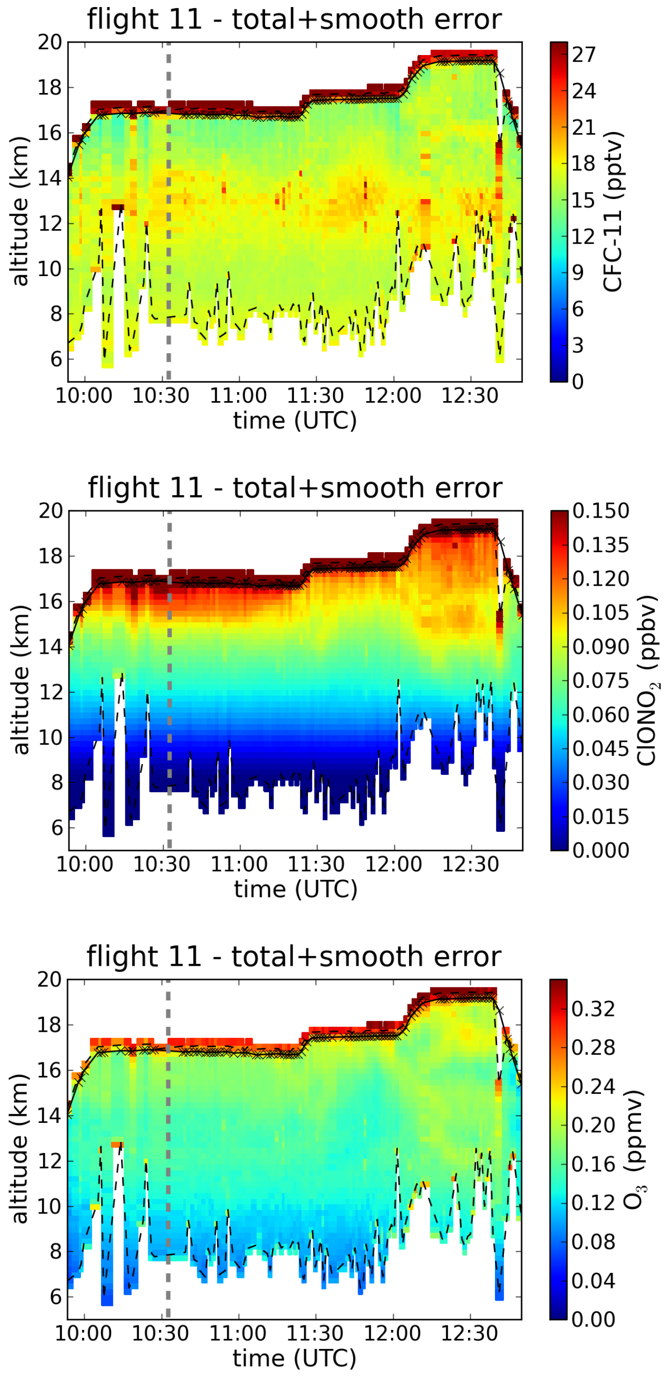

a)

b)

c)

Figure 6.10: Cross sections of the total+smooth errors for the trace gases CFC-11 (a)), $ClONO_2$ (b)), and O_3 (c)) for flight 11. The solid black line shows the flight altitude and the dashed black lines the lowest and highest tangent height of a valid measurement. The position (time) of each profile is marked by a black cross. Different viewing directions of the instrument are separated by a grey dashed line.

the CFC-11 VMRs inside and outside the vortex.

The situation at the end of the flight is more complicated. Although both structures show nearly the same CFC-11 VMRs, only the lower structure is located in an area with high values of mPV (see Fig. 6.4). The upper structure is located in an area, where only moderate values of mPV are present. This leads to the assumption that only the lower structure contains air masses with a high fraction of vortex air masses. The air masses in the upper structure are mainly of non-vortex origin. Meteorological data show that the two observed structures at the end of the flight are vertical sections through filaments.

Additionally, some structures with high CFC-11 VMRs are visible, for example in the area immediately below flight altitude at the end of the flight. The distribution of mPV (see Fig. 6.4) shows the lowest values in the same area, which together indicates, that the observed air masses most likely originate from mid or low latitudes.

The distribution of $ClONO_2$ is shown in Fig. 6.9 panel b). In the area identified as polar vortex, the $ClONO_2$ VMRs reach maximum values of around 1.5 ppbv. As described in Sec. 2.3 the active chlorine in vortex air masses is converted back into its reservoir species $ClONO_2$ and HCl after the presence of polar stratospheric clouds and the very cold temperatures inside the vortex. Which reservoir species is formed depends on the amount of available ozone, because the Cl/ClO ratio depends on this. More available ozone leads to a larger amount of ClO. Since the ozone destruction is typically smaller in the Arctic than in the Antarctic, the amount of ClO is larger in the Arctic. In addition, less NO is available, which reacts with ClO and forms Cl. Thus, the Cl/ClO ratio is much smaller in the Arctic than in the Antarctic. The formation of HCl by the reaction of Cl and CH_4 is therefore suppressed or slowed down in the Arctic in the time right after the onset of chlorine deactivation. The available ClO reacts with NO_2 and forms $ClONO_2$. A detailed discussion of the chlorine partitioning is given e.g. by Douglass et al. (1995) and Grooss et al. (1997). The authors showed that for ozone volume mixing ratios below ≈ 0.5 ppmv a rapid increase of HCl occurs, whereas for ozone VMRs above ≈ 0.5 ppmv the formation of $ClONO_2$ is favoured.

Santee et al. (2008) showed measurements illustrating this process for the winter of 2004/05. The $ClONO_2$ volume mixing ratios reached the highest values in early to mid-March. The maximum volume mixing ratios were even higher than at the beginning of the winter. The formation of HCl is suppressed or slowed down at the beginning of deactivation and the typical summer equilibrium between $ClONO_2$ and HCl builds up in the following months. Since the CRISTA-NF measurements took place at the beginning of March and the ozone volume mixing ratios were larger than 0.5 ppmv, very high $ClONO_2$ volume mixing ratios are therefore expected inside the polar vortex, because of the favoured formation of $ClONO_2$.

The cross section of O_3 (Fig. 6.9 c)) shows lower or equal VMRs inside the polar vortex region compared to outside at comparable altitudes. These lower/equal O_3 VMRs are caused due to the ozone destruction inside the polar vortex (see Sec. 2.3). Without ozone destruction and according to the subsidence of air masses inside the vortex together with the vertical ozone distribution (maximum above the flight altitude), one would expect higher ozone VMRs inside the polar vortex than outside. Since ozone is destroyed and the VMRs remain low until the break off of the polar vortex, these high values do not occur.

Both filaments at the end of the flight show significant differences in the $ClONO_2$ and ozone volume mixing ratios. Inside the lower filament comparable low ozone VMRs and high $ClONO_2$ VMRs are present. In contrast, the upper filament exhibits significant higher ozone and lower $ClONO_2$ VMRs. This difference confirms the assumption that only the lower filament contains a great fraction of air masses originating from the polar vortex.

Furthermore, the $ClONO_2$ and ozone VMRs are low in the area immediately below flight altitude at the end of the flight and in the thin layer between the two filaments. This is in very good agreement with the observed high CFC-11 VMRs in the same regions and additionally confirms that the air masses are of different origin than the polar vortex.

In summary, the distributions of all trace gases provide a consistent picture. The polar vortex and different structures are clearly visible in all retrieval results, which is also in a good agreement with the distribution of modified potential vorticity. The observed situation is analysed in more detail in the following sections.

6.2.3. Polar vortex

The subsidence of air masses inside the polar vortex and the mixing barrier caused by the high speed of the zonal wind at the vortex edge can be seen best in the comparison of selected profiles inside and outside the vortex. Here CFC-11 is used for the comparison, since the distribution of this inert trace gas is mainly determined by advection and mixing and not by chemical processes.

Fig. 6.11 shows two selected profiles of CFC-11 VMRs derived from the CRISTA-NF measurements for two altitude scans during flight 11. The first altitude scan is performed inside the polar vortex (blue) at 10:27 UTC (near the turning point of the aircraft) and the second scan is performed outside the vortex at 11:50 UTC (red). The potential temperature is used as new height coordinate, because horizontal mixing and advection in the stratosphere are adiabatic processes and typically occur along surfaces of equal potential temperature.

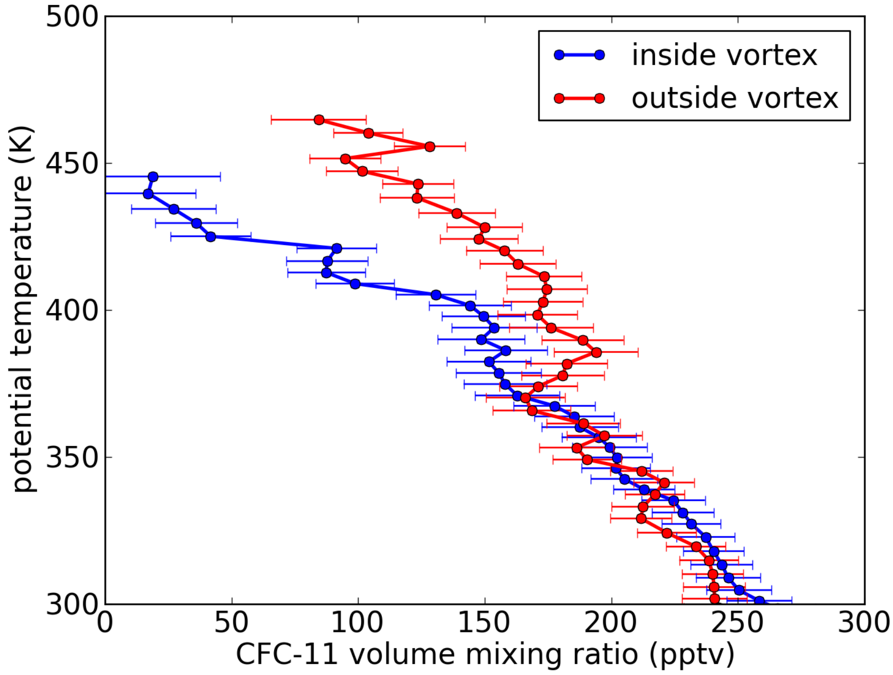

Figure 6.11: Selected CFC-11 profiles for two altitude scans during flight 11. The first altitude scan at 10:27 UTC (blue) is located inside the polar vortex and the second one at 11:50 UTC (red) outside the vortex. Results are shown between flight altitude and the lowest tangent height of a valid measurement. The error bars show the total+smooth error of the CRISTA-NF retrieval results.

At the highest altitudes both profiles differ from each other. A maximum difference of about 80 pptv can be seen at 450 K. This difference is a consequence of the diabatic descent of air masses inside the vortex. The vertical displacement between air masses inside and outside the vortex is about 45 K at 80 pptv. In geometric altitude (not separately shown) the air masses are displaced by about 1.7 km. The high speed of the zonal wind at the vortex edge forms a mixing barrier and the air masses inside the vortex are isolated from air masses outside the vortex. Hence, mixing of air masses inside and outside the vortex rarely occurs and the differences remain.

Below 410 K both profiles mostly agree within the error bars, albeit there still seems to be a systematic difference. Going further down, both profiles are nearly identical below 370 K. Thus, the bottom edge of the vortex, above of which both profiles are significantly different, is located at 410 K and in geometric altitude at about 15 km.

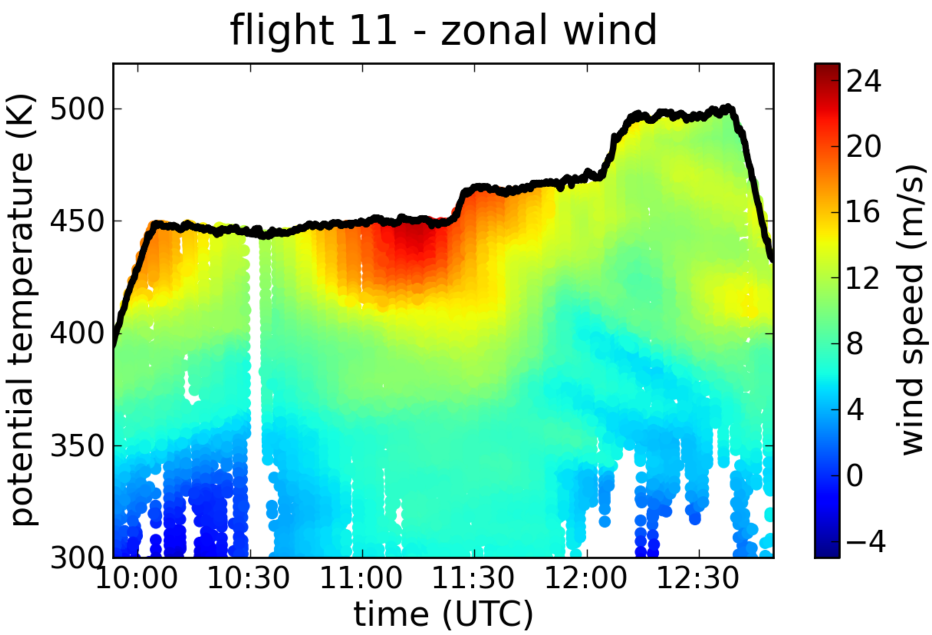

Figure 6.12: Cross section of zonal wind at the CRISTA-NF tangent points for flight 11. The altitude of the aircraft is marked by a solid black line.

Further insight in vortex structure and mixing barrier can be obtained from the zonal wind speed at different altitudes. Fig. 6.12 displays the zonal wind at the tangent points of the CRISTA-NF measurements of flight 11. Positive values indicate westerlies and negative values easterlies.

The highest wind speeds of about 23 m/s are visible at the vortex edge at around 11:15 UTC at the highest altitudes. This maximum in the zonal wind speed agrees very well with the steep increase of the CFC-11 VMRs observed at flight altitude at the same time (compare Fig. 6.7), which also shows the vortex edge. Thus, at the highest altitudes a strong mixing barrier exists isolating the air masses inside the vortex from outside.

The speed of the zonal wind is decreasing with decreasing altitude in this region. Thus, the strength of the mixing barrier decreases as well. Consequently, the horizontal mixing of air masses increases. Below 370 K the wind speeds are lower than 10 m/s and the mixing barrier is very weak. Thus, the CFC-11 VMRs of both profiles (inside and outside) are nearly the same below 370 K. The CRISTA-NF observations clearly illustrate the altitude dependence of the mixing barrier and show that isolated air masses only exist above a certain altitude level.

6.2.4. Ozone-CFC-11-relation

The relationships between stratospheric trace gases depend on the region (e.g. polar vortex, tropics) and thus, different curves form in a scatter plot showing VMRs of one trace gas vs. VMRs of another trace gas (Plumb, 2007). In this section the ozone-CFC-11-relation is used to distinguish between vortex and non-vortex air masses. Inside the polar vortex this relation changes during the winter because of ozone depletion, which leads to an even larger contrast to the relation outside the vortex (Müller et al., 2005). Hence, the ozone-CFC-11-relation is well suited to analyse the two observed filaments with low CFC-11 VMRs at the end of flight 11 (see Fig. 6.9 panel a)) in terms of their amount of vortex air masses.

The volume mixing ratios of ozone and CFC-11 inside the filaments are displayed in a scatter plot in Fig. 6.13. The measurements inside the lower filament are depicted in red and those inside the upper filament in green. All measurements are filtered with respect to time, tangent height and a threshold for the CFC-11 volume mixing ratio of 100 pptv to analyse only the measurements inside the filaments.

In order to get a comparison to air masses inside and outside the vortex two additional ozone-CFC-11-relations are shown, one for each region. The relation outside the vortex shows volume mixing ratios of measurements between 11:30 UTC and 12:00 UTC (black circles) and the relation inside the vortex volume mixing ratios of measurements around the aircraft turn between 10:15 UTC and 10:45 UTC (blue circles).

The relations inside and outside the polar vortex are the same for CFC-11 volume mixing ratios greater than about 130 pptv because of the horizontal mixing in the troposphere and the lowermost stratosphere at altitudes, where no mixing barrier is present. For volume mixing ratios smaller than 130 pptv the relations differ from each other due to the different composition of the air masses and the ozone loss inside the polar vortex.

The ozone-CFC-11-relation of the lower filament mostly lies on the vortex relation. Only a few points are significantly different. Thus, the air masses inside this filament contain a large amount of vortex air masses, otherwise both relations would separate. In contrast to that, the ozone-CFC-11-relation of the upper filament cannot be distinguished from the relation outside the vortex but clearly separates from the relation of the lower filament. This underlines the difference of the air masses inside the two observed filaments.

Thus, this analysis confirms the statements made above that only the lower filament contains a large amount of air masses originating from the polar vortex. The air masses inside the upper filament are definitively of other origin.

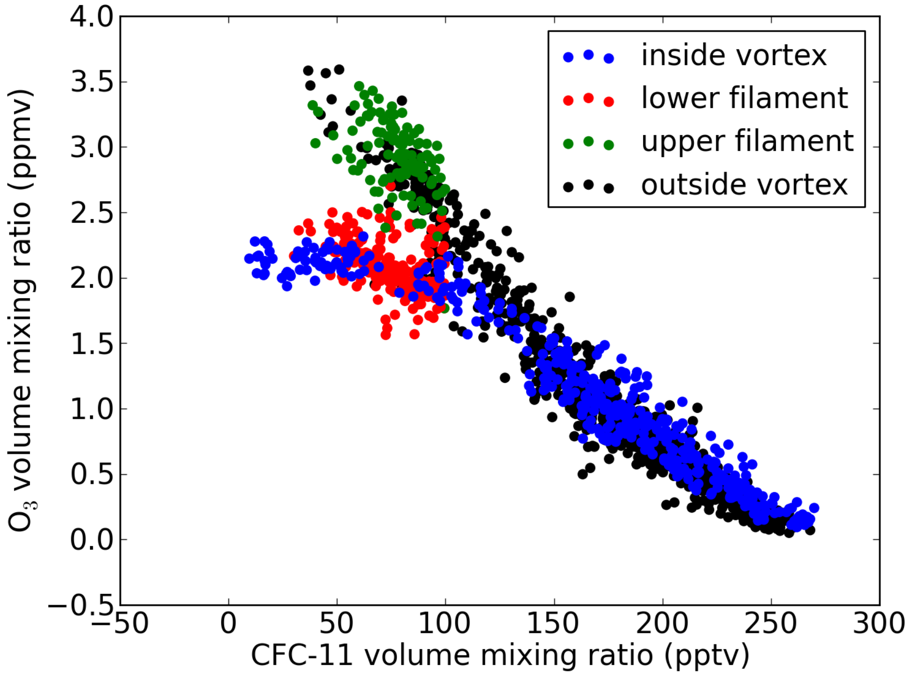

Figure 6.13: Scatter plot of ozone VMR vs. CFC-11 VMR for flight 11 for the four regions: inside vortex (blue), lower filament (red) and upper filament (green) at the end of the flight, outside vortex (black).

6.2.5. De- and renitrification during flight 11

During the polar winter inside the polar vortex crystalline NAT particles can form and sediment. Since this NAT particles consist of HNO_3 and H_2O (ratio typically 1:3), HNO_3 is transported downward. At lower altitudes and higher temperatures the NAT particles evaporate and gaseous HNO_3 is released. As a result, gaseous HNO_3 is taken from higher altitudes (denitrification) and transported to lower altitudes (renitrification) (see Chap. 2).

Fig. 6.14 shows the retrieval results for HNO_3 for flight 11 and the corresponding total+smooth error. Inside the polar vortex at the beginning of the flight such de- and renitrification layers can be seen. The HNO_3 VMRs around flight altitude in this region are significantly lower than in the altitude region a few kilometres below. The observed layer with higher HNO_3 VMRs exhibits a vertical extent of around 2 km.

In addition to the de- and renitrification layers inside the polar vortex the cross section of HNO_3 shows very high volume mixing ratios in the air masses containing a high fraction of vortex air masses (lower filament at the end of the flight). The maximum values are about

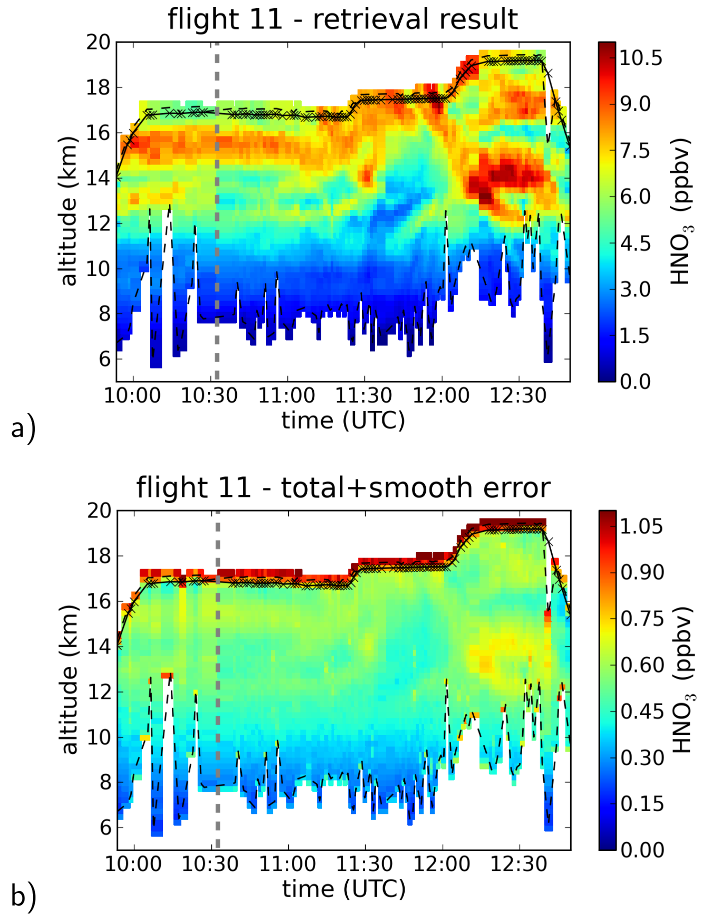

Figure 6.14: Retrieval result of the CRISTA-NF measurements for HNO_3 (a)) for flight 11 and corresponding total+smooth error (b)). The solid black line shows the flight altitude and the dashed black lines the lowest and highest tangent height of a valid measurement. The position (time) of each profile is marked by a black cross. Different viewing directions of the instrument are separated by a grey dashed line.

10.5 ppbv.

Fig. 6.15 shows the HNO_3 VMRs for two selected altitude scans inside and outside the vortex to illustrate the differences in these regions. If neither de- nor renitrification has occurred, one would expect a profile which is monotonically increasing with increasing altitude in the observed altitude range. This is obviously only the case for the profile outside the vortex above 380 K. The maximum at 365 K is caused by a small structure with high HNO_3 VMRs (compare cross section in Fig. 6.14 a)).

The profile inside the polar vortex shows a local maximum at 420 K as a consequence of the sedimentation and evaporation of NAT particles. Above this altitude the VMRs decrease with further increasing altitude and at 450 K the HNO_3 VMRs inside the vortex are significantly

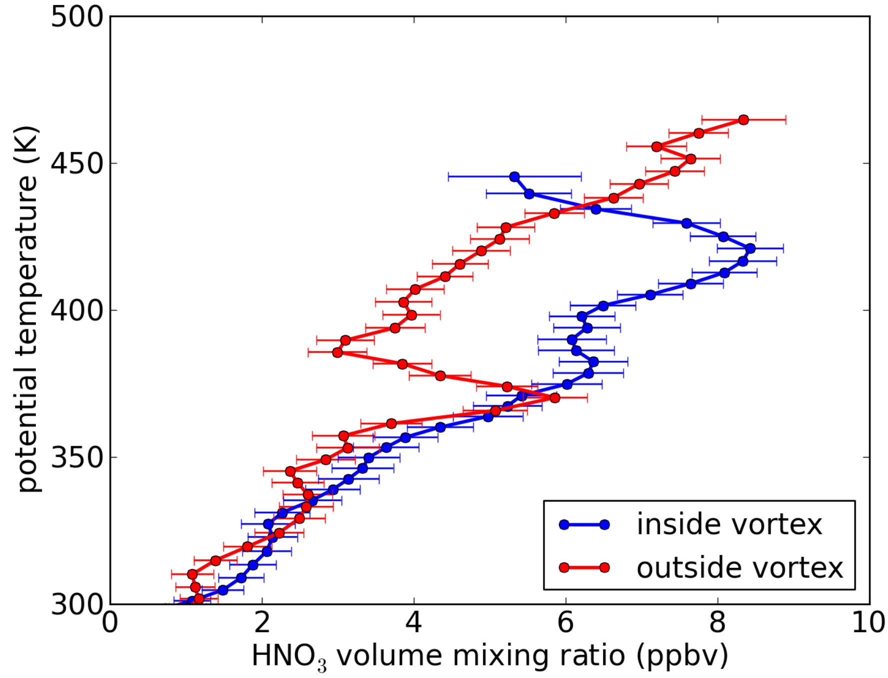

Figure 6.15: Selected HNO_3 profiles for two altitude scans during flight 11. The first altitude scan at 10:27 UTC (blue) is located inside the polar vortex and the second one at 11:50 UTC (red) outside the vortex. The results are displayed between flight altitude and the lowest tangent height of a valid measurement. The error bars show the total+smooth error of the CRISTA-NF retrieval results

lower than outside. This lower HNO_3 VMRs at the highest altitudes can only be explained by a denitrification of the stratosphere. Thus, the CRISTA-NF observations clearly illustrate the de- and renitrification in the stratosphere during winter and spring.

6.3. Summary

The CRISTA-NF retrieval results for the trace gases CFC-11, O_3, $ClONO_2$, and HNO_3 for the RECONCILE flight 11 are presented and discussed in this chapter. By means of independent measurements (HAGAR, FOZAN, and MIPAS-STR) the quality of the derived volume mixing ratios is analysed. All of the comparisons show that the CRISTA-NF retrieval results are both qualitatively and quantitatively reliable and provide a good basis for further analyses.

The cross sections of the trace gases exhibit different structures, some of them with a vertical extent of 1 km or less, which illustrates the high vertical resolution of the retrieval results. Different observed air masses and regions such as the polar vortex and a vortex filament can be identified and distinguished by means of the measurements. The O_3-CFC-11-relation is used to clearly identify this vortex filament and differentiate it from another observed filament of other origin. Furthermore, the subsidence of air masses inside the polar vortex and the mixing barrier at the vortex edge are illustrated using the distribution of the inert trace gas CFC-11 and the zonal wind. Comparisons of CFC-11 profiles inside and outside the vortex show a vertical displacement of this trace gas of about 1.7 km inside the vortex compared to outside. The bottom edge of the vortex is located at about 15 km. Finally, the de- and renitrification of the stratosphere is shown by means of HNO_3 profiles inside the polar vortex.

Taken together, all obtained results show the quality and reliability of the CRISTA-NF retrieval results and the capability of the measurements to study the lowermost stratosphere. The unprecedented vertical resolution and high quality of the results provide an ideal basis for detailed comparisons, especially with model simulations, and the validation of model concepts. Several comparison with model results and examinations of the model performance with respect to different atmospheric processes are therefore presented in the next chapter.

7. Comparison with CLaMS

The CRISTA-NF retrieval results exhibit a very good resolution (vertical and horizontal along flight track) and are therefore well suited to analyse the performance of a model in terms of transport processes (advection and mixing). Furthermore, the capability of a model to simulate chemical processes inside the polar vortex can be studied by means of different important stratospheric trace gases, like e.g. O_3, $ClONO_2$, and HNO_3. Additionally, a model concept, which enables the analysis of the air mass origin, is presented in this chapter and validated by means of the CRISTA-NF results. The Chemical Lagrangian Model of the Stratosphere (CLaMS) is used in the following sections for these analyses and the performance of the model is assessed.

7.1. CLaMS description and setup

This section gives a short summary of the model properties and important procedures and presents the setup used for the simulations of the results shown.

CLaMS is a chemistry and transport model (CTM) based on a Lagrangian approach to simulate the transport of trace gases. The employment of such a Lagrangian transport scheme enables the simulation of small scale structures as they are observed in the stratosphere, but often not resolved in Eulerian models because of numerical diffusion (McKenna et al., 2002b). The first version of CLaMS was formulated by McKenna et al. (2002b,a) as a 2-dimensional model on isentropic surfaces. An ensemble of air parcels on a time-dependent irregular grid is simulated. The Lagrangian transport of these air parcels consists of two steps, an advection step and a mixing step. In the advection step the air parcels move along trajectories, which are calculated based on meteorological wind fields. The subsequent mixing is obtained by utilising a dynamically adaptive grid. After each advection step the distances of each air parcel to its prior nearest neighbours are determined and compared to the critical distances $r^c_\pm$. If the distance between two air parcels is smaller than r^c_-, the air parcels are merged and the characteristics of the new air parcel are the mean characteristics of the two former ones. Furthermore, a new mixed air parcel is inserted between two air parcels if these air parcels move away from each other and the distance after the advection step is larger than r^c_+. The critical distances are defined as

$$r^c_\pm = r_0 \exp(\pm\lambda_c \Delta t), \tag{7.1}$$

where r_0 gives the mean separation between all air parcels (horizontal resolution of the model), λ_c is the Lyapunov exponent and Δt the time step. The Lyapunov exponent gives the expansion rate and is used to adjust the mixing in CLaMS, whereby a smaller value induces more mixing and vice versa. As a consequence of this scheme, mixing in CLaMS only occurs in regions of flow deformation. A detailed description of the Lagrangian transport is given by McKenna et al. (2002b) and Konopka et al. (2004).

Konopka et al. (2004) extended the isentropic version of CLaMS to three dimensions by application of cross isentropic transport. The cross isentropic velocities of the air parcels are determined by means of radiative heating/cooling rates. In the 3-dimensional version the model atmosphere is divided in horizontal layers and the adaptive regridding is performed in each of this layers as described above. The employment of cross isentropic transport is, for example, necessary to simulate the subsidence of air masses inside the polar vortex (e.g. Konopka et al., 2004).

The introduction of a hybrid vertical coordinate ζ, which is equal to the potential temperature in the stratosphere and parallel to the pressure isolines in the troposphere, enables the extension of the model to the tropopause region and the troposphere (Konopka et al., 2007).

The chemistry scheme used here is an updated version of the scheme described by McKenna et al. (2002a). A number of 48 chemical species and 144 reactions (84 binary, 13 ternary, 36 photolysis, 11 heterogeneous) are considered in the model.

The nucleation, sedimentation and evaporation of NAT particles in CLaMS is obtained utilising a Lagrangian denitrification scheme as described by Grooß et al. (2005). The integration of this scheme allows the simulation of de- and renitrification processes in the polar stratosphere.

The setup used for the CLaMS simulations presented in the following sections is summarised in Tab. 7.1. All simulations are initialised and started on December 1, 2009. The initialisation of the atmospheric trace gases is partly obtained by means of globally distributed measurements by satellite instruments such as MLS (Microwave Limb Sounder;

Table 7.1: Summary of the CLaMS setup.

model parameter	setting
horizontal resolution (mean separation of air parcels)	70 km
horizontal range	0°– 90°North
vertical levels	50
vertical resolution	≈ 500 m
vertical range	300 K > ζ < 900 K
meteorological wind fields	ECMWF ERA interim data (1°× 1°)
heating/cooling rates	ECMWF clear sky radiative heating rate
time step Δt	24 hours
Lyapunov exponent λ_c	1.5 d^{-1}
NAT nucleation rate	$8{\cdot}10^{-5}\,cm^{-1}\,h^{-1}$
	(10 times larger as in Grooß et al. (2005)

Waters et al., 2006), ACE-FTS (Atmospheric Chemistry Experiment - Fourier Transform Spectrometer; Bernath et al., 2005) and MIPAS-ENV (Michelson Interferometer for Passive Atmospheric Sounding-ENVisat; Fischer et al., 2008)). Remaining trace gases are initialised using different correlations or partitioning of trace gases within chemical families.

7.2. Advection and mixing

In this section the CLaMS results for CFC-11 for flight 11 are presented and compared with the retrieval results of the CRISTA-NF measurements to assess the performance of the model in terms of advection and mixing. Since CFC-11 is an inert trace gas, the spatial distribution on time scales of weeks to month is mainly determined by these processes.

CLaMS results at two different times, shortly before the flight and shortly after the flight, are used for the comparison. The results are interpolated in time and space onto the CRISTA-NF retrieval grid. All CLaMS results shown in this chapter are prepared in the same manner. A convolution is not necessary, since the vertical resolution of both data sets is very similar.

Fig. 7.1 displays the cross sections of the CRISTA-NF retrieval result and the CLaMS result for CFC-11. The main structures observed by the CRISTA-NF instrument, the polar vortex and the two filaments with low CFC-11 VMRs at the end of the flight, are well reproduced by CLaMS. Even the thin layer with higher mixing ratios located between the two filaments and the air masses with enhanced CFC-11 VMRs immediately below flight altitude at the end of the flight are clearly visible.

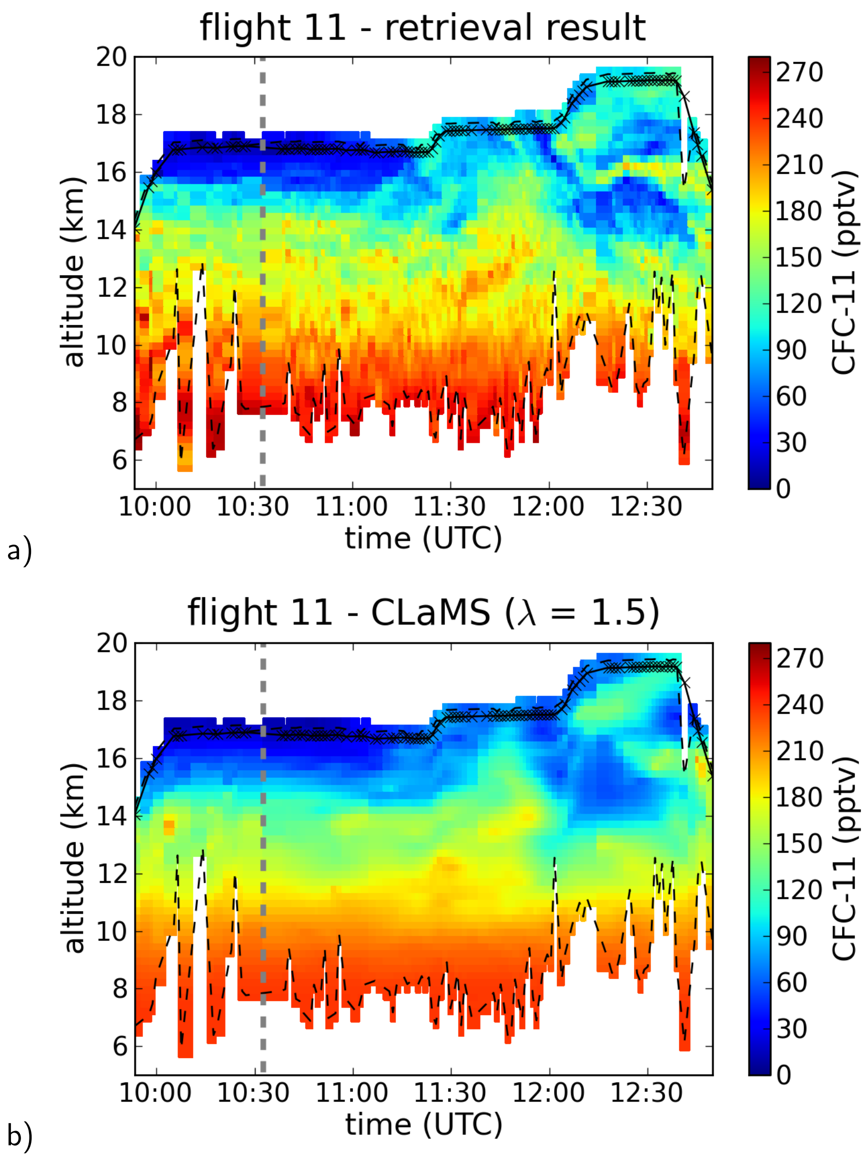

Figure 7.1: Comparison between CRISTA-NF (a)) and CLaMS (b)) results for CFC-11 for flight 11. The solid black line shows the flight altitude and the dashed black lines the lowest and highest tangent height of a valid measurement. The position (time) of each profile is marked by a black cross. Different viewing directions of the instrument are separated by a grey dashed line.

Nevertheless, some small differences can be seen, for example, in the vortex edge region at around 11:20 UTC between 17 km and 14 km, where some small scale structures with higher CFC-11 volume mixing ratios are missing in the model result. Taking into account the different horizontal resolution of both results (CRISTA-NF ≈ 15 km; CLaMS ≈ 70 km), some of these small differences might be at least caused by the decreased horizontal resolution of

CLaMS and the interpolation onto the CRISTA-NF retrieval grid. However, the CFC-11 cross sections agree very well and only marginal differences are visible.

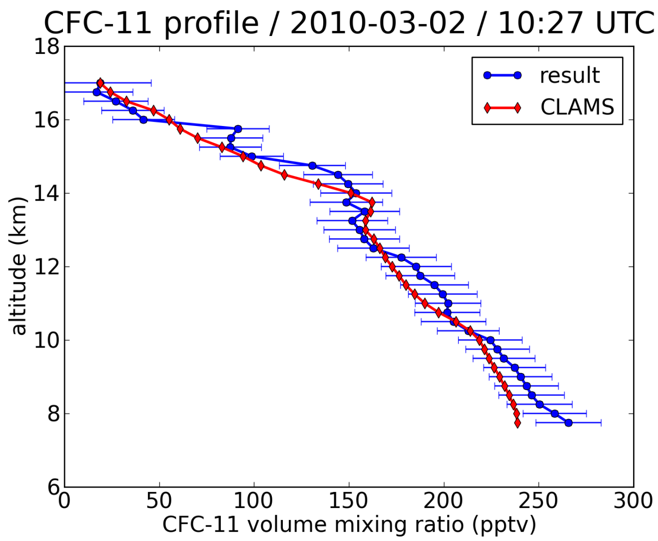

a)

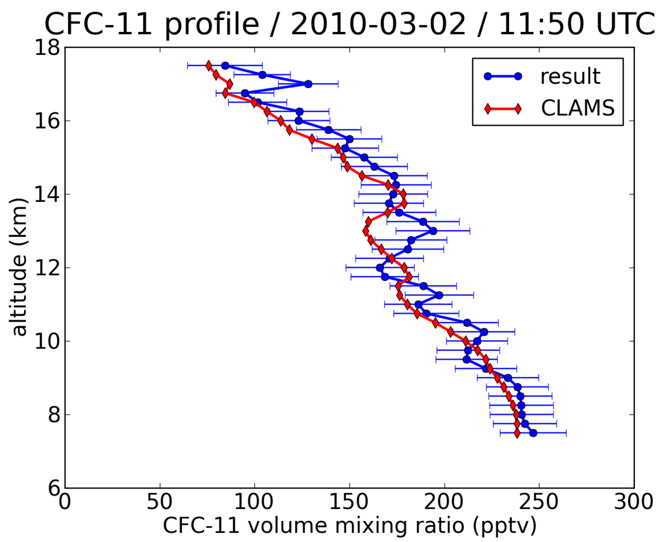

b)

Figure 7.2: Comparison between CRISTA-NF (blue) and CLaMS (red) results for CFC-11 for two altitude scans. The first altitude scan at 10:27 UTC (a)) is located inside the polar vortex and the second one at 11:50 UTC (b)) outside the vortex. Results are shown between flight altitude and the lowest tangent height of a valid measurement. The error bars show the total+smooth error of the CRISTA-NF retrieval results

In order to compare the absolute values in more detail, the results for two selected altitude scans are shown in Fig. 7.2. One altitude scan was performed inside the polar vortex at 10:27 UTC and the other was performed outside the vortex at 11:50 UTC. The profiles are displayed between flight altitude and the lowest tangent height of a valid CRISTA-NF measurement. The CRISTA-NF retrieval result and the CLaMS result mostly agree within the errors. The profiles differ from each other only at a few points. For example, the local maximum and minimum observed by CRISTA-NF at 13 km and 12 km in the altitude scan outside the vortex (Fig. 7.2 b)) are shifted in the CLaMS result by 1 km. This shift is caused by the different location and extent of the structure with enhanced CFC-11 VMRs, which is located between 11 km and 14 km at around 11:30 UTC (compare Fig. 7.1). Nonetheless, the agreement of the results in terms of both absolute values and observed structures illustrates the good performance of CLaMS with respect to transport processes.

7.3. Air mass origin

A model concept based on artificial tracers and capable to analyse the origin of air masses is presented in this section and the CRISTA-NF observations of the polar vortex and the vortex filament are used to validate this model concept. Furthermore, the effect of a vortex split event on the composition of these artificial tracers is shown.

A whole set of artificial tracers (or passive tracers), each of them representing a different type of air mass (e.g. vortex, tropics), is used in CLaMS. The tracers of each air parcel are initialised according to the value of modified potential vorticity (mPV; see Müller and Günther, 2003, Sec. 6.1.3) of the air parcel. Since these tracers are completely inert, they are only advected and mixed in the model and these processes are simulated very well by CLaMS (compare Sec. 7.2). At a later time the composition of an air parcel in terms of the artificial tracers can be used to analyse the origin of the air masses. A detailed description of this concept is given by Günther et al. (2008).

Tab. 7.2 summarises the mPV boundaries for each tracer. If an air parcel fulfils the boundary conditions, the corresponding tracer is set to 1 and all other tracers to 0. The values of the artificial tracers therefore give the fractions of the different types of air masses, whereby a value of 1 denotes 100%. The tracers are denoted as passive tracers P0 – P3 in this section.

The analysis of the CRISTA-NF measurements clearly showed the observation of the polar vortex and a vortex filament during flight 11. The results for the passive tracer P3, which represents vortex air masses, highly depend on the date of the tracer initialisation. Fig. 7.3 shows the CLaMS passive tracer for vortex air masses for two different dates of initialisation. On the one hand, the passive tracers are initialised on December 1 (panel a)) and, on the other hand, the tracers are initialised on January 1 (panel b)). The tracers are dis-

Table 7.2: Summary of the modified potential vorticity boundaries for the artificial tracers and the corresponding type of air masses.

passive tracer	mPV boundary (in PVU)	type of air masses
P0	0 – 8	low latitude
P1	8 – 14.7	mid latitude
P2	14.7 – 19.8	outer vortex edge / high latitude
P3	> 19.8	vortex

played in the altitude range from flight altitude down to 10.5 km, since Müller and Günther (2003) showed that the concept of modified potential vorticity is valid down to 350 K (here ≈ 10.5 km). Thus, all passive tracers in this section are shown in the same altitude range.

Both tracers exhibit large differences, especially inside the polar vortex and the vortex filament. The vortex tracer initialised on December 1 reaches values around 0.5 inside the polar vortex at the beginning of the flight, which corresponds to a fraction of vortex air masses of only 50 %. The tracer initialised on January 1 by contrast shows values larger than 0.9 inside the vortex. Additionally, the vortex filament, which is located at around 14 km at the end of the flight, can clearly be seen in the distribution of the vortex tracer initialised on January 1 (values around 0.75) but hardly be identified in the distribution of the vortex tracer with the earlier initialisation. Thus, the vortex tracer initialised on January 1 shows the same results as obtained from the CRISTA-NF measurements.

The observed differences between the two vortex tracers can be explained by taken into account the evolution of the polar vortex in winter 2009/10. In early December 2009 the vortex splitted into two parts and a stable vortex formed again at end of December. Furthermore, a second split event occurred in February 2010. A detailed description of the evolution of the polar vortex is given by Dörnbrack et al. (2012). The composition of the polar vortex therefore changed in December between the two dates of initialisation because of in-mixing of air masses into the vortex. The vortex characteristics on December 1 and January 1 thus are largely different.

The results of the CRISTA-NF measurements are all obtained with regards to the polar vortex at the beginning of March. Obviously, December 1 is not a reasonable reference date for comparison because of the composition change during December. The vortex characteristics on January 1 after the split and mixing event by contrast are evidently comparable to the vortex characteristics at the beginning of March. Thus, the second split event in February had no significant effect on the vortex composition until begin of March. The presented results clearly show the importance of the date of the tracer initialisation for an analysis of

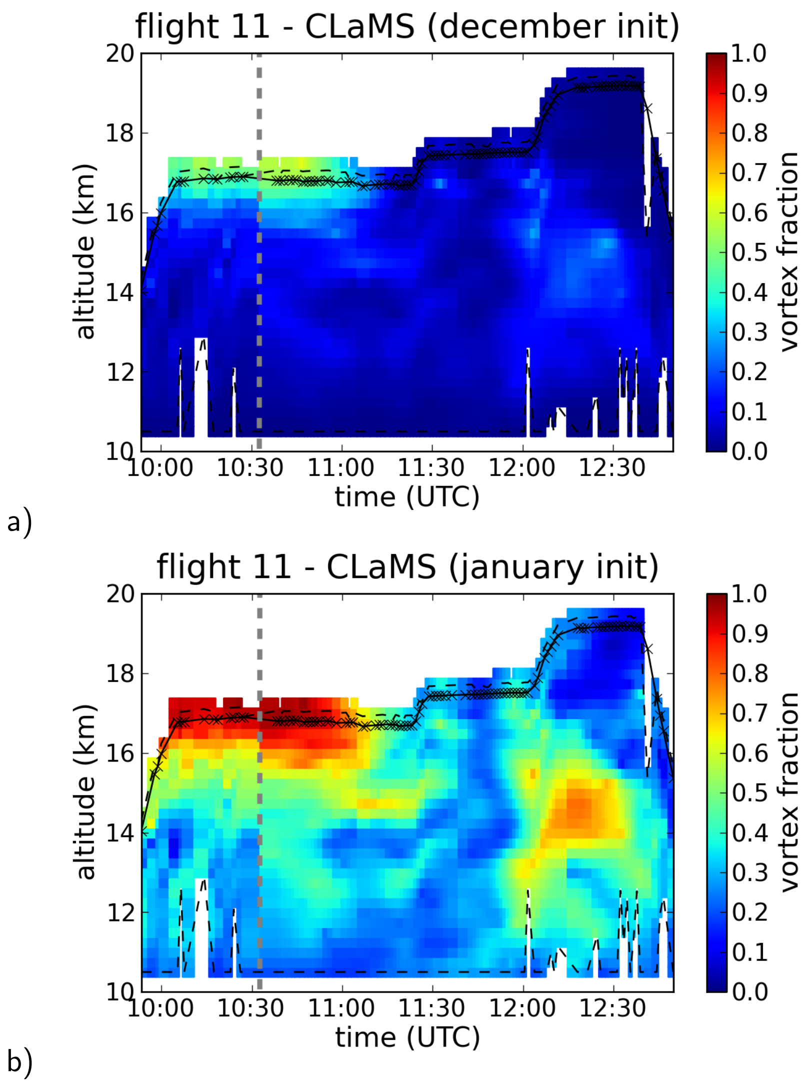

Figure 7.3: CLaMS vortex tracer (P3) for flight 11. Panel a) shows the vortex tracer initialised on December 1 and panel b) the vortex tracer initialised on January 1. The solid black line shows the flight altitude. The position (time) of each profile is marked by a black cross. Different viewing directions of the instrument are separated by a grey dashed line.

the polar vortex and vortex filaments, since the reference date and the vortex characteristics at this date are crucial factors. Hence, the passive tracers initialised on January 1 are used hereafter to obtain additional information about the composition of the observed air masses during flight 11 in terms of the origin.

A comparison between the tracers of the two dates of initialisation can be used to quantify the effect of the split and mixing event in December on the air mass composition. Fig. 7.4 shows the difference in the vortex fraction between the January and December initialisation.

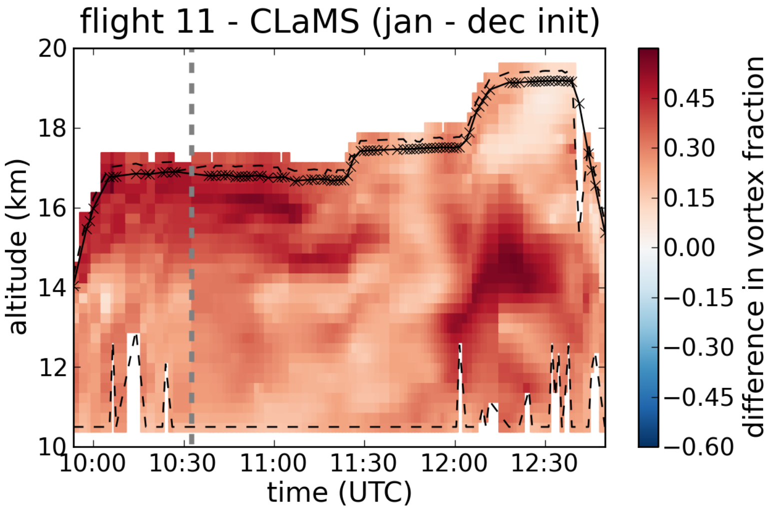

Figure 7.4: Difference in the vortex fraction between January and December initialisation for flight 11. The solid black line shows the flight altitude. The position (time) of each profile is marked by a black cross. Different viewing directions of the instrument are separated by a grey dashed line.

The largest differences in the vortex fraction can be seen in the area of the polar vortex below flight altitude at the beginning of the flight and in the vortex filament at the end of the flight. The differences are around 0.5 in these regions. Since the polar vortex was stable after January 1, which is indicated by the high values of the vortex fraction (larger 0.9) of the January initialisation, the difference inside the vortex is almost only caused by the air masses mixed into the vortex during December. Thus, the air masses mixed into the vortex partly account for 50 % of the total air masses inside the vortex after the split event.

Since the sum of all passive tracers in each air parcel is always 1, the positive change in the vortex tracer has to be compensated by a negative change in the other tracers. The observed changes in the other tracers therefore show the proportion to which these other tracers contributed to the in-mixed air masses. Fig. 7.5 shows the change in the high and mid latitude fraction between the December and January initialisation, respectively, divided by the change in the vortex fraction. The changes in the high and mid latitude fraction are multiplied by the factor -1 to obtain a positive contribution. The change in the low latitude fraction is close to zero and therefore negligible.

Inside the polar vortex around flight altitude high latitude air masses are the main contributor to the in-mixed air masses. The contribution of high latitude air masses partly exceeds 0.7 at flight altitude, whereas the contribution of mid latitude air masses is around 0.3.

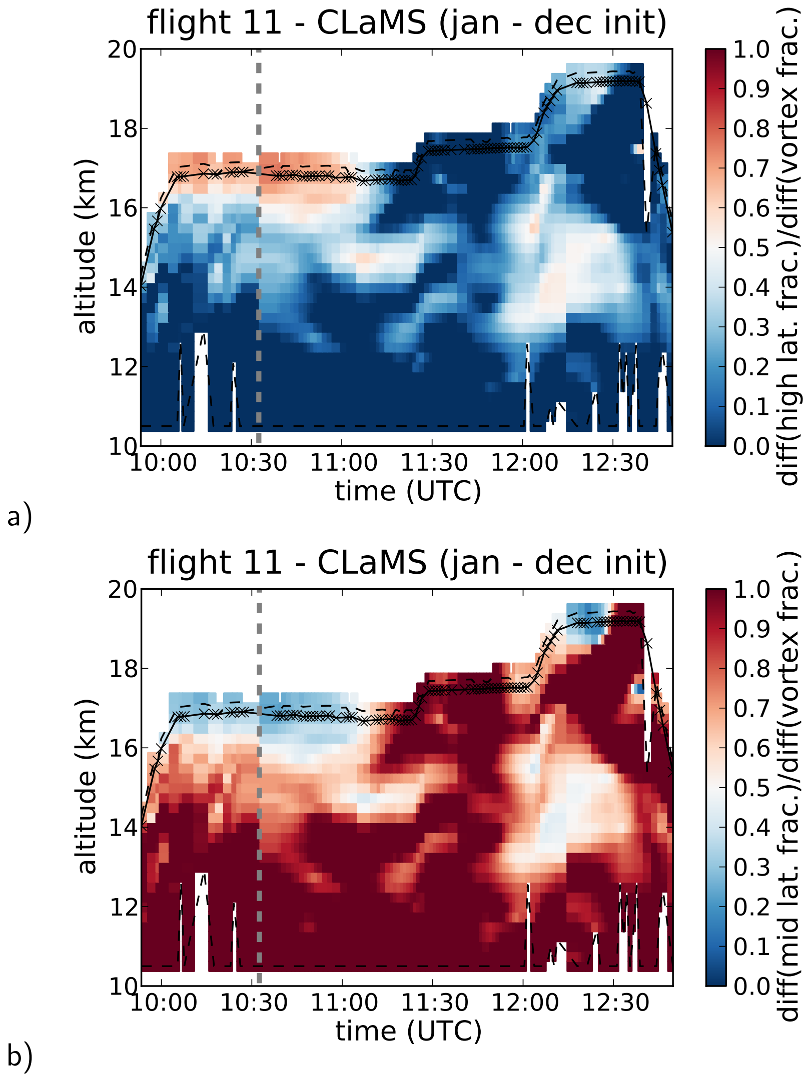

Figure 7.5: Difference in the high latitude fraction (a)) and mid latitude fraction (b)) between January and December initialisation divided by the difference in the vortex fraction for flight 11. The differences in the high and mid latitude fraction are multiplied by -1 to obtain a positive contribution. The solid black line shows the flight altitude. The position (time) of each profile is marked by a black cross. Different viewing directions of the instrument are separated by a grey dashed line.

Thus, at these altitudes high latitude air masses account for around 70 % and mid latitude air masses for around 30 % of the air masses mixed into the vortex. Since the change in the low latitude fraction is close to zero, air masses of this origin were not mixed into the vortex during December.

In addition to the analysis of the split and mixing event, other passive tracers can be used to explain the whole observed situation during flight 11 and obtain additional information about the air mass origin. Fig. 7.6 shows the low latitude fraction (passive tracers initialised on January 1) for flight 11. Several structures with high values are clearly visible. The first one is located in the middle of the flight between 15 km and 11 km. The low latitude fraction in this region partly exceeds 0.6, which means that more than 60% of the air masses originate from low latitudes. This structure corresponds to a structure with high CFC-11 VMRs (larger than 200 pptv) at around 11:45 UTC (compare panel a) in Fig. 7.1) and is therefore in good agreement with the observations.

At the end of the flight two additional structures with values around 0.6 can be seen at 16 km and immediately below flight altitude. In the same areas the CFC-11 VMRs of the CRISTA-NF retrieval result show values mostly larger than 150 pptv. The comparable high CFC-11 VMRs immediately below flight altitude and in the thin layer between the two structures with low CFC-11 VMRs are therefore mainly a consequence of the transport of low latitude air masses toward the pole.

Moreover, this explains the observation of the upper filament with low CFC-11 VMRs, which is not a vortex filament. This filament is only visible in the observations, because the surrounding air masses are mainly of low latitude origin. This leads to the observed contrast between the air masses inside and outside the filament. Overall, the observed structures in the distributions of the passive tracers are in very good agreement with the observations by CRISTA-NF.

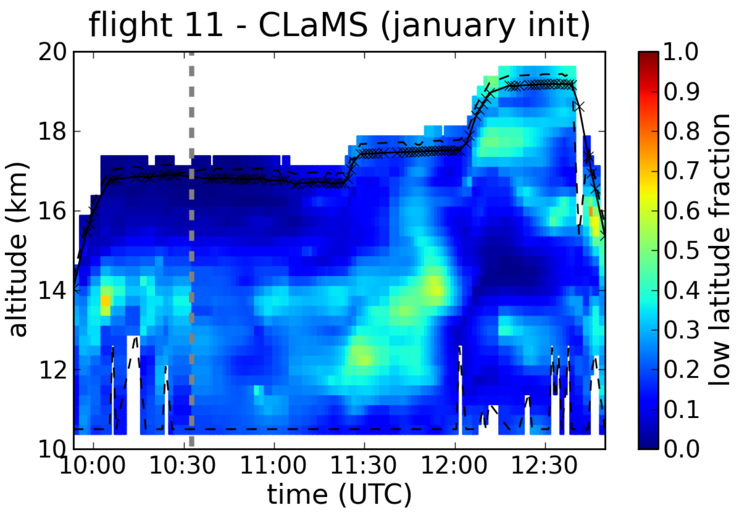

Figure 7.6: CLaMS low latitude tracer for flight 11 initialised on January 1. The solid black line shows the flight altitude. The position (time) of each profile is marked by a black cross. Different viewing directions of the instrument are separated by a grey dashed line.

7.4. Ozone chemistry and chlorine activation

This section proceeds with the comparison between the CRISTA-NF and CLaMS results for ozone and $ClONO_2$. By means of these comparisons the simulation of ozone chemistry and chlorine activation and deactivation inside the polar vortex by CLaMS is analysed.

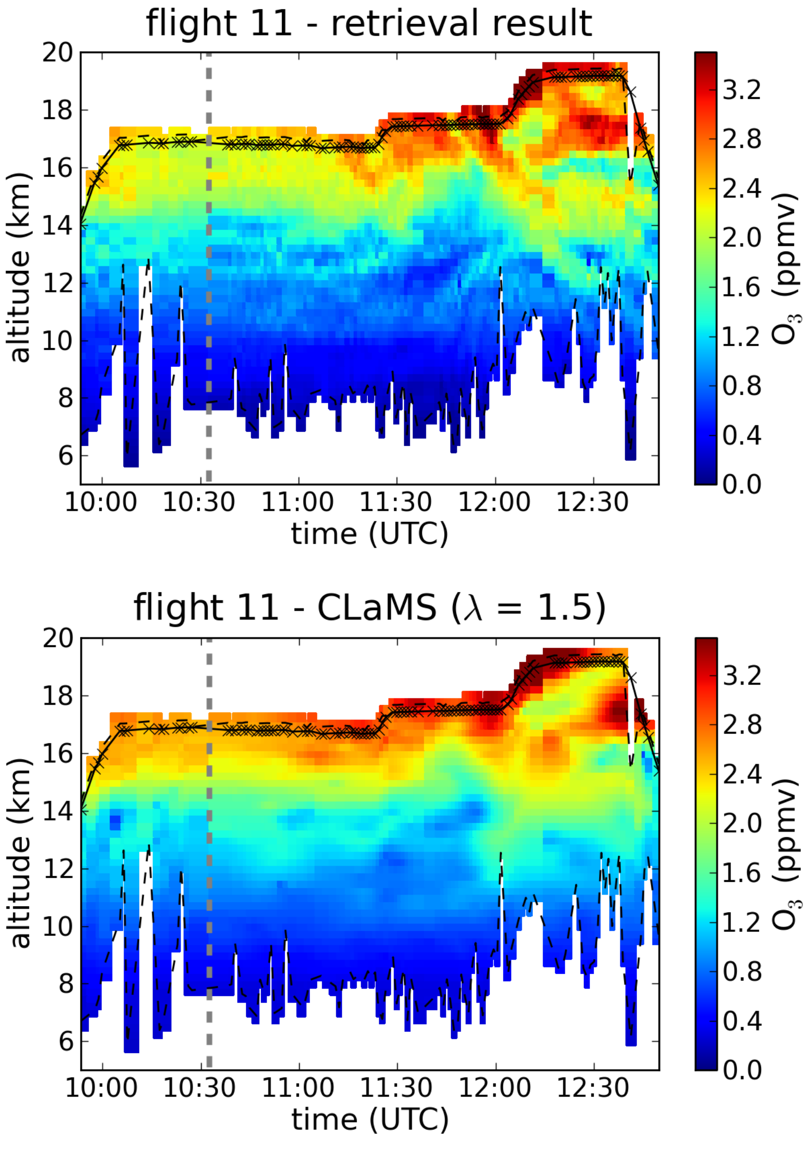

Figure 7.7: Comparison between CRISTA-NF (a)) and CLaMS (b)) results for O_3 for flight 11. The solid black line shows the flight altitude and the dashed black lines the lowest and highest tangent height of a valid measurement. The position (time) of each profile is marked by a black cross. Different viewing directions of the instrument are separated by a grey dashed line.

Fig. 7.7 shows the cross sections of the ozone volume mixing ratios for CRISTA-NF and CLaMS for flight 11. The agreement of both results for the most parts of the flight is very good. Nevertheless, similar as for CFC-11, differences in some small scale structures are visible. Additionally, the largest disagreement can be seen in the polar vortex at the beginning of the flight. Significant higher ozone VMRs are visible in the CLaMS results in this area. This might be an indication for an underestimation of the ozone depletion inside the polar vortex by CLaMS.

In order to obtain a closer look, the results for two selected altitude scans, one inside the polar vortex and one outside, are shown in Fig. 7.8. The profiles of the CRISTA-NF and the CLaMS results for the altitude scan outside the vortex (Fig. 7.8 b)) agree very well, especially at altitudes above 14 km. Below this altitude the same shift in the local maxima and minima as observed for CFC-11 is visible. However, the CLaMS results in regions outside the vortex are reliable in terms of the absolute values. The ozone profiles inside the polar vortex (Fig. 7.8 a)) below 15 km are nearly identical and the differences in the absolute values are mostly consistent within the error bars. Above 15 km the ozone VMRs of the CLaMS result are significantly higher and the differences are larger than the errors.

Since differences only occur inside vortex air masses and the ozone VMRs in these air masses are connected to the ozone depletion, this indicates an underestimation of the ozone loss by CLaMS. The ozone depletion by chlorine catalysed cycles is one of the main processes determining the ozone VMRs inside the vortex (see Sec. 2.3). Hence, the available amount of active chlorine is very important for modelling ozone destruction. An underestimation of the chlorine activation would lead to less ozone depletion inside the polar vortex.

The comparison between the CRISTA-NF and CLaMS results for $ClONO_2$, which is one of the important chlorine reservoir species, is shown in Fig. 7.9. The agreement in most parts of the flight is very good and all main structures can be seen in both results. Nonetheless, some small differences are visible, like the lower $ClONO_2$ VMRs in the lower filament at the end of the flight in the CLaMS result. Additionally, the vertical extent of the area with high volume mixing ratios at the beginning of the flight is not fully captured by CLaMS.

Fig. 7.10 depicts the comparison of $ClONO_2$ profiles inside and outside the vortex to assess the reliability of the absolute values of the CLaMS result in more detail. The profiles of CRISTA-NF and the CLaMS results outside the vortex (Fig. 7.10 b)) differ from each other in the altitude range above 12 km. A positive bias of the CLaMS result, which is mostly larger than the errors, is clearly visible, albeit the shape of the profile is reproduced well. Inside the polar vortex (Fig. 7.10 a)) both profiles agree mostly within the error bars, except for

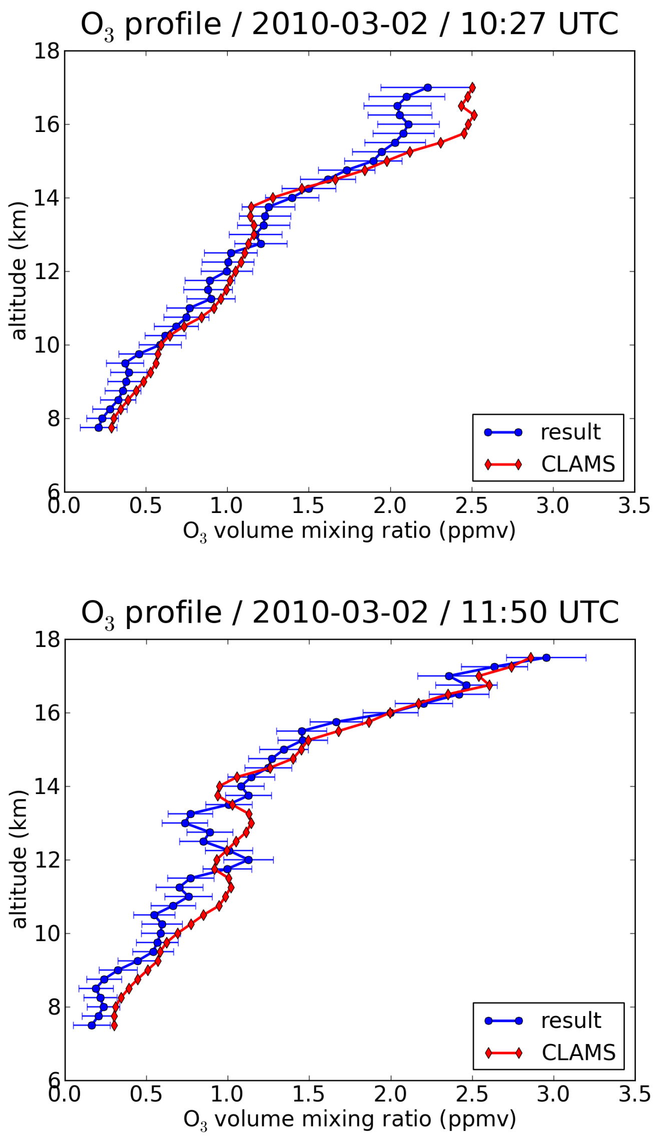

a)

b)

Figure 7.8: Comparison between CRISTA-NF (blue) and CLaMS (red) results for O_3 for two altitude scans. The first altitude scan at 10:27 UTC (a)) is located inside the polar vortex and the second one at 11:50 UTC (b)) outside the vortex. Results are shown between flight altitude and the lowest tangent height of a valid measurement. The error bars show the total+smooth error of the CRISTA-NF retrieval results

the altitude range between 15 km and 16.5 km. In this altitude range the $ClONO_2$ VMRs of the CLaMS result are significantly lower than those of the CRISTA-NF retrieval result.

The observed differences might indicate small deficiencies in the simulation of the chlorine activation and deactivation by CLaMS. But additional information would be necessary to analyse this in detail. Apart from $ClONO_2$, HCl is the second important chlorine reservoir

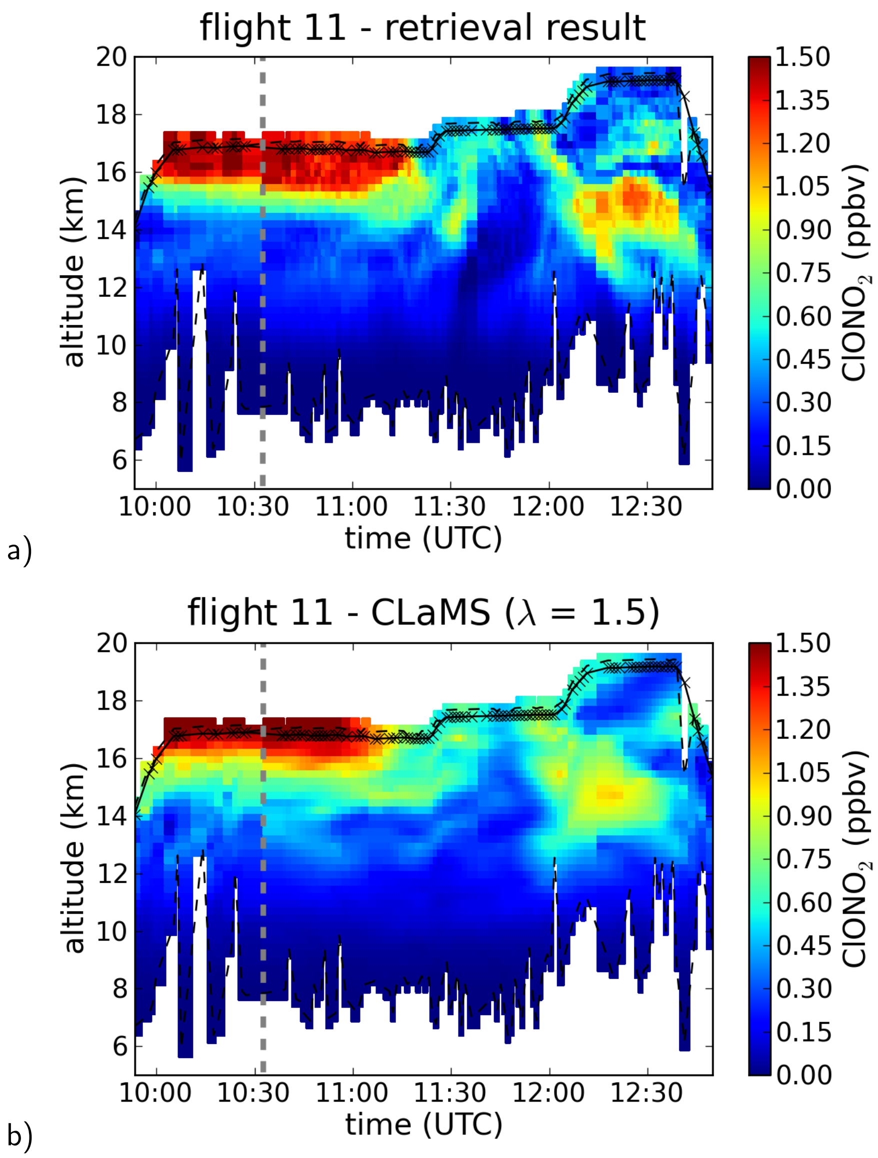

Figure 7.9: Comparison between CRISTA-NF (a)) and CLaMS (b)) results for $ClONO_2$ for flight 11. The solid black line shows the flight altitude and the dashed black lines the lowest and highest tangent height of a valid measurement. The position (time) of each profile is marked by a black cross. Different viewing directions of the instrument are separated by a grey dashed line.

species in the stratosphere, which unfortunately cannot be derived from the CRISTA-NF measurements. Furthermore, the time evolution of both chlorine reservoir species would have to be taken into account to find clear evidences for possible problems in the chlorine activation/deactivation in CLaMS. Unfortunately, such information cannot be obtained from the CRISTA-NF measurements. Moreover, deficiencies in the initialisation of $ClONO_2$ or HCl

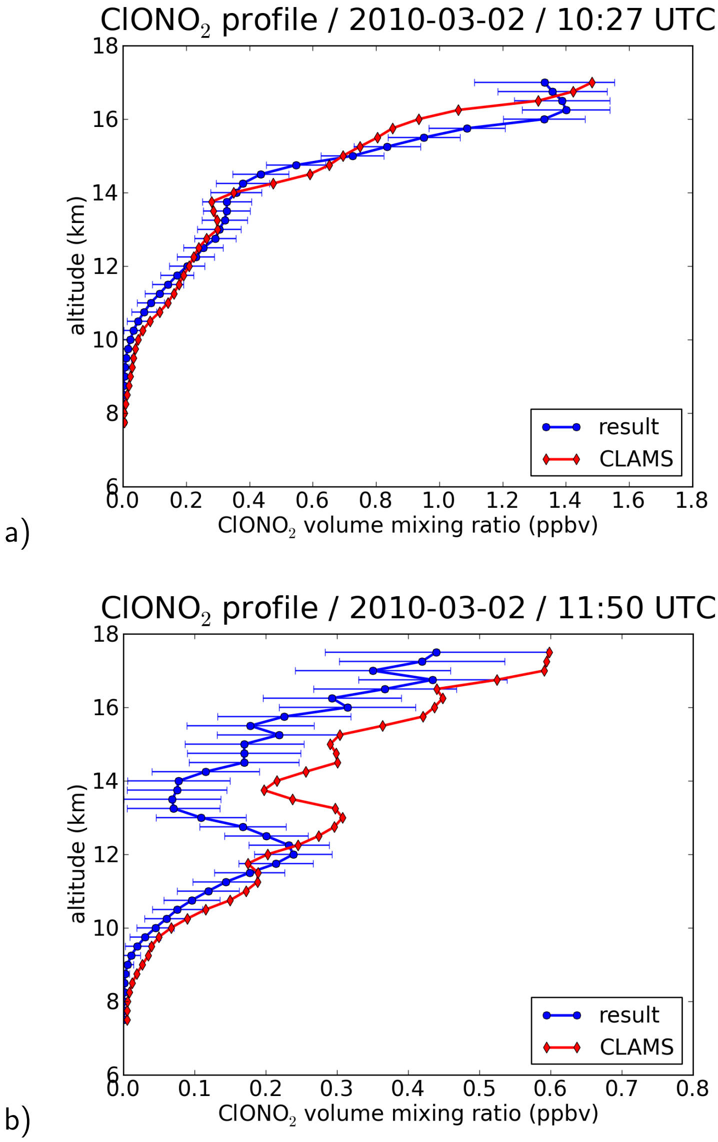

Figure 7.10: Comparison between CRISTA-NF (blue) and CLaMS (red) results for $ClONO_2$ for two altitude scans. The first altitude scan at 10:27 UTC (a)) is located inside the polar vortex and the second one at 11:50 UTC (b)) outside the vortex. Results are displayed between flight altitude and the lowest tangent height of a valid measurement. The error bars show the total+smooth error of the CRISTA-NF retrieval results

could play a role, too.

Comparisons between CLaMS results and satellite measurements for HCl and $ClONO_2$ (altitude range: 400 K – 550 K, time period: begin of December to end of March) show a good agreement for $ClONO_2$ but larger differences for HCl in January. The HCl VMRs of the CLaMS results are significantly higher than those of the satellite measurements, which indicates an underestimation of the chlorine activation from the reservoir species HCl (personal communication: J.-U. Grooß). Thus, this underestimation is the reason for the underestimation of ozone depletion by CLaMS. Since the chlorine deactivation in the Arctic polar vortex at the beginning is mainly driven by the formation of $ClONO_2$ (e.g. Douglass et al., 1995; Grooss et al., 1997; Santee et al., 2008), an underestimation of the chlorine activation from the reservoir species HCl could lead to lower $ClONO_2$ VMRs at the beginning of the deactivation as well. This might be the reason for the observed differences between the $ClONO_2$ VMRs measured by CRISTA-NF and simulated by CLaMS.

7.5. Denitrification

The employment of a Lagrangian denitrification scheme in CLaMS enables the simulation of formation and sedimentation of NAT particles, which is an essential process for the vertical redistribution of HNO_3 in the stratosphere (Grooß et al., 2005). A comparison between the CRISTA-NF and CLaMS results for HNO_3 for flight 11 are presented in this section to investigate the performance of this scheme. The cross sections of the CRISTA-NF and CLAMS results for HNO_3 are shown in Fig. 7.11. All observed main structures are clearly visible in both results, like the structure at around 14 km at the end of the flight, which exhibits the highest HNO_3 VMRs during the whole flight. But in contrast to the CRISTA-NF retrieval result neither a de- nor a renitrification layer inside the polar vortex at the beginning of the flight can clearly be seen.

The situation inside the vortex is illustrated in Fig. 7.12 by the comparison of the CRISTA-NF and CLaMS results for a selected altitude scan inside the vortex. Additionally, the results for an altitude scan outside the vortex are shown. The profiles of both results agree very well outside the vortex (Fig. 7.12 b)) and only the same shift in the vertical location of the local maximum and minimum, which is observed for all trace gases, can be seen. Inside the polar vortex (Fig. 7.12 a)) both profiles show more differences, like the dip at 14 km, which is clearly visible in the CLaMS result but can hardly be seen in the CRISTA-NF result. Furthermore, the steep decrease of the HNO_3 volume mixing ratios above 16 km is not fully captured by CLaMS and significant differences at flight altitude are recognisable.

The de- and renitrification of the lower stratosphere depends on the formation, sedimentation and evaporation of NAT particles (see Sect. 2.2). Since the sedimentation speed of the NAT particles is related to the particle size and the evaporation is highly related to the atmospheric conditions, the modelling of these processes is very difficult. For example, small

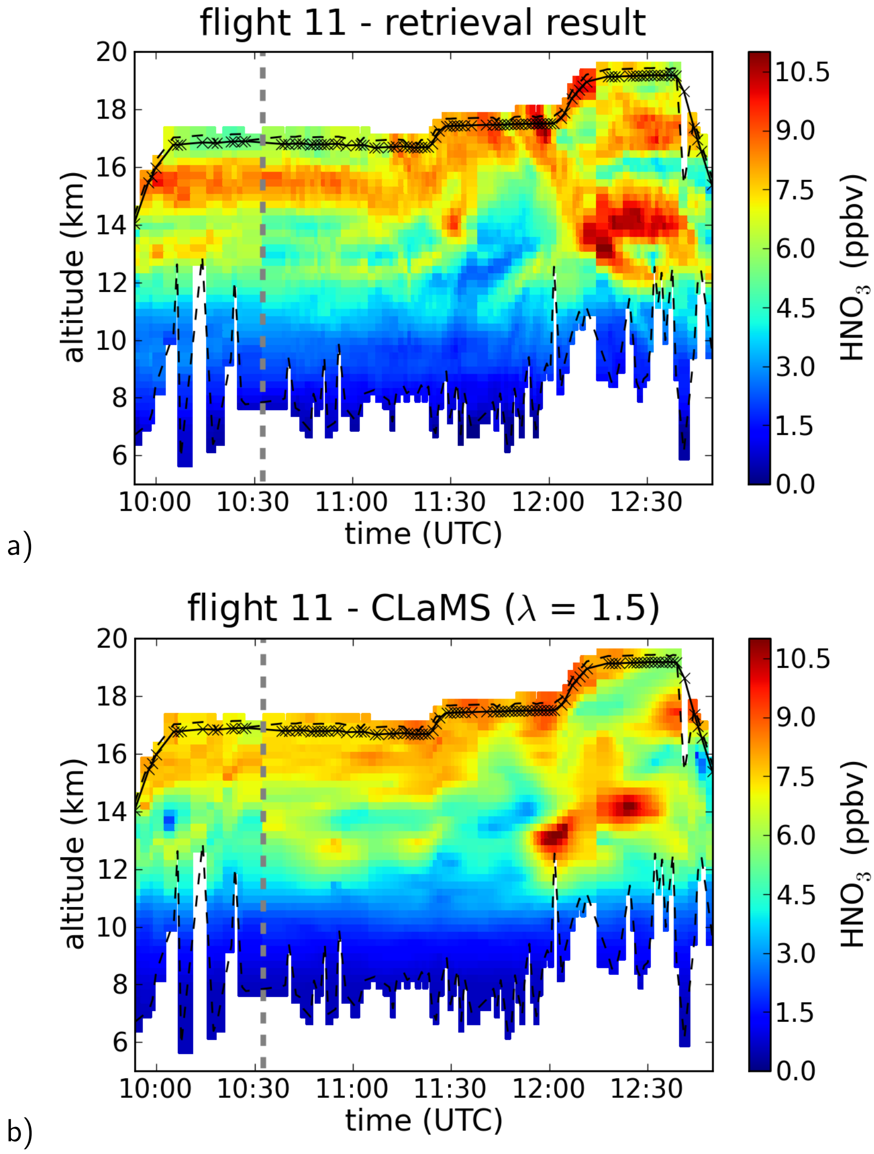

Figure 7.11: Comparison between CRISTA-NF (a)) and CLaMS (b)) results for HNO_3 for flight 11. The solid black line shows the flight altitude and the dashed black lines the lowest and highest tangent height of a valid measurement. The position (time) of each profile is marked by a black cross. Different viewing directions of the instrument are separated by a grey dashed line.

differences in the temperature distribution in CLaMS compared to the real atmosphere or wrong nucleation rates can lead to significant differences between CLaMS results and observations (see Grooß et al., 2005). The observed differences illustrate these difficulties. However, the general distribution of HNO_3 is in a reasonable agreement with the CRISTA-NF observations.

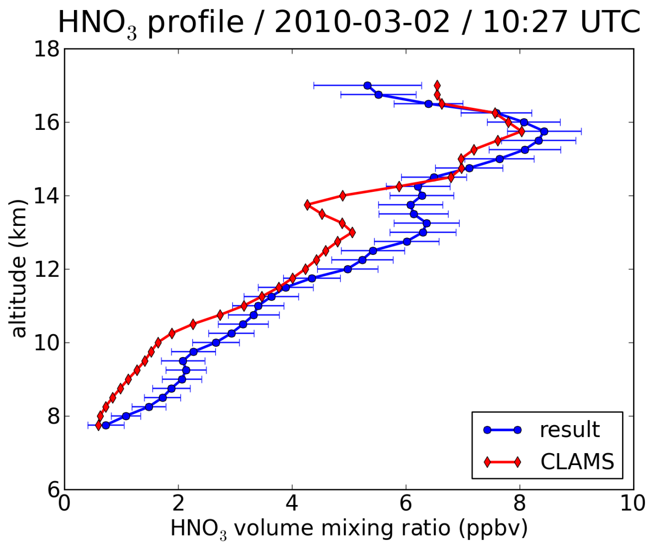

a)

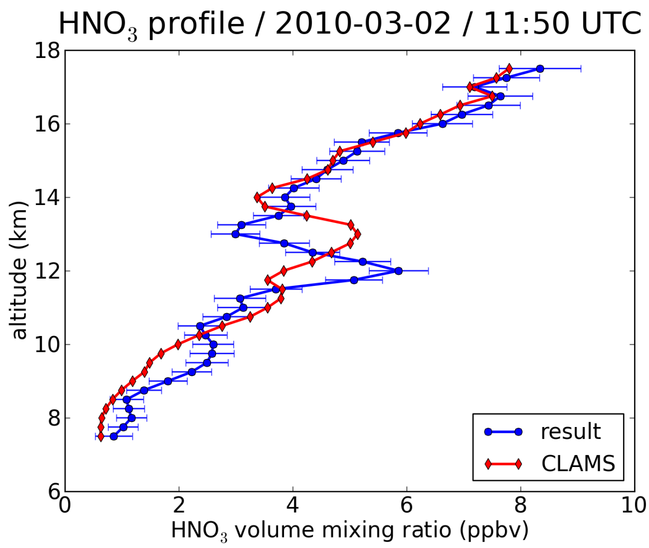

b)

Figure 7.12: Comparison between CRISTA-NF (blue) and CLaMS (red) results for HNO_3 for two altitude scans. The first altitude scan at 10:27 UTC (a)) is located inside the polar vortex and the second one at 11:50 UTC (b)) outside the vortex. Results are displayed between flight altitude and the lowest tangent height of a valid measurement. The error bars show the total+smooth error of the CRISTA-NF retrieval results

7.6. Summary

The comparisons between the CRISTA-NF retrieval results and the CLaMS simulations for flight 11 mostly show a good agreement. Especially the excellent agreement of both results for CFC-11 illustrates the good performance of CLaMS in terms of advection and mixing.

Nevertheless, some differences for the trace gases O_3, $ClONO_2$, and HNO_3 can be seen inside the polar vortex and in vortex filaments. The observed differences indicate an underestimation of the ozone depletion inside vortex air masses by CLaMS, which is most likely caused by an underestimation of the chlorine activation. Comparisons with satellite measurements confirm the underestimation of chlorine activation from the reservoir species HCl.

Additionally, a concept based on artificial tracers is presented, which can be used to analyse the composition of air masses with respect to the origin. By means of these artificial tracers the polar vortex and air masses of different origin (vortex filament and low latitude air masses) can be identified. Comparisons with the results obtained from CRISTA-NF show the importance of the date of the artificial tracer initialisation for such analyses, since the vortex characteristics at the initialisation date is a crucial factor. This is especially important, if the tracers are compared with measurements or shall deliver additional information to measurement results.

Furthermore, during a vortex split event, which took place in December 2009, a large amount of air masses were mixed into the vortex and therefore changed the composition and characteristics of the vortex. The artificial tracers are used to analyse these air masses. The results show that high latitude air masses contributed most to the air masses mixed into the vortex (up to 70 %). The second important contributor were mid latitude air masses, whereas low latitude air masses were not mixed into the vortex.

8. Conclusion and outlook

The presented thesis concentrates on the analysis of the CRISTA-NF measurements aboard the Russian research aircraft M55-Geophysica during the RECONCILE aircraft campaign in Kiruna (Sweden) from mid-January to mid-March, 2010. The measurements were all carried out in the vicinity of the polar vortex and analysed with respect to different scientific objectives, like the descent of air masses inside the vortex and the observation and identification of air masses of different origin. Furthermore, the detection and differentiation of PSCs composed of different particle types (NAT, STS, ice) are presented. All results show the high quality and versatility of the CRISTA-NF measurements.

Polar stratospheric clouds were observed during the first five flights of the aircraft campaign. These PSCs are analysed by methods based on different absorption and therefore emission characteristics of the different particle types, which allow the discrimination of ice and PSCs composed of (or clearly dominated by) a larger number of small NAT particles. The results derived from the measurements and meteorological data show evidence for an ice cloud located above flight altitude during flight 1 (2010-01-17). Furthermore, PSCs composed of a large amount of small NAT particles (mean radii $< 3\,\mu m$) can be excluded. Nevertheless, the presence of small NAT particles cannot be completely ruled out, because a smaller number of small particles or small particles, which exist together with large ones, cannot be distinguished from STS by means of the presented methods.

The instrumentation aboard the M55-Geophysica, which contains different instruments measuring the particle size distribution and the vertical extent of the observed PSCs, enables the compilation of a unique data set about PSC properties. This data will be used for a detailed validation and a further development of analysis methods for determining the composition of PSCs by means of limb emission spectra. The particle measurements aboard the M55-Geophysica are only capable to differentiate particle sizes but not types. CRISTA-NF therefore will provide additional information about the composition of observed polar stratospheric clouds.

The main scientific application of CRISTA-NF is the derivation of trace gas volume mixing ratios from the limb emission spectra. The used retrieval setup allows for the derivation of vertical profiles of several trace gases, whereby CFC-11, O_3, HNO_3, and $ClONO_2$ are the main targets. This thesis presents the full exploitation of the vertical sampling of CRISTA-NF, which enables an unprecedented vertical resolution of the retrieval results. The vertical resolution is about 500 – 600 m for several kilometres below flight altitude for O_3, HNO_3, and $ClONO_2$ and even less than 500 m for CFC-11. Comparisons between the retrieval results and in-situ measurements by HAGAR and FOZAN as well as measurements by the infrared limb sounder MIPAS-STR illustrate the good quality of the CRISTA-NF measurements.

The very high vertical resolution and the dense horizontal sampling along the flight direction ($\approx$ 15 km) allow the analysis of small scale structures in the atmosphere. Flight 11 of the RECONCILE aircraft campaign is used here as case study. The CRISTA-NF measurements show the observation of the polar vortex and two filaments of different origin during this flight. By means of O_3-CFC-11-relations the two observed filaments could be identified as one vortex and one non-vortex filament. Additionally, the cross-sections (2-dimensional curtain of all profiles) exhibit a very thin layer with a vertical extent of partly less than 1 km showing enhanced CFC-11 VMRs and decreased ozone and $ClONO_2$ VMRs, respectively. This clearly illustrates the capability of CRISTA-NF to observe such small structures. Thus, the CRISTA-NF retrieval results provide an excellent basis for comparisons with model simulations to assess the model performance in terms of small scale transport structures.

The chemistry and transport model CLaMS is used in this thesis. CFC-11, an inert trace gas, whose distribution on time scales from days to weeks is determined by advection and mixing, is used to asses the capability of CLaMS with respect to advection and mixing. The comparison between the CRISTA-NF and CLaMS results for CFC-11 shows the ability of CLaMS to reproduce the observed small scale structures. Hence, the performance of CLaMS with respect to transport is very good. In contrast, the comparison between the CRISTA-NF and CLaMS results for ozone indicates an underestimation of the ozone depletion inside the polar vortex by CLaMS, which is caused by an underestimation of chlorine activation. Outside the vortex, CLaMS is able to simulate the chemical processes, in which ozone and $ClONO_2$ are involved. Furthermore, the comparison between the CRISTA-NF and CLaMS results for HNO_3 highlights the difficulty to simulate the formation and sedimentation of NAT particles inside the vortex.

The observation of the polar vortex and the two filaments is additionally used to validate a model concept to identify the origin of air masses. This model concept is based on artificial tracers. These tracers are only advected and mixed in the model and allow the differentiation of air masses of different origin, like the polar vortex or the tropics. The presented results clearly illustrate the importance of the date of the tracer initialisation. Only the tracers initialised on January 1 show the same results as obtained from the measurements, because the CRISTA-NF results are referred to the polar vortex in March, which is very similar to the vortex at begin of January in terms of the air mass composition. The earlier initialisation on December 1 exhibits larger differences caused by a vortex split event in December. During this split event a large amount of air masses from outside are mixed into the vortex and changed the composition. Thus, December 1 is not a reasonable reference date for the comparison with CRISTA-NF results in terms of the vortex characteristics and cannot be used to obtain additional information beyond what can be derived from the measurements. A comparison between the artificial tracers of both initialisation dates shows that the air masses mixed into the vortex partly account for 50% of the air masses inside the vortex after the split event.

In summary, the thesis presents the capability of highly resolved retrieval results for detailed model comparisons and the validation of model concepts. Such comparisons are a prerequisite for the improvement of model performance to enhance the reliability of model predictions of the future development of the atmosphere. However, CRISTA-NF only provides local measurements in two dimensions and is therefore limited regarding the horizontal and vertical coverage. This limitation will be overcome in the future by the new limb imaging technique (Riese et al., 2005) that was developed for airborne (e.g. Ungermann, 2011) and satellite application (ESA, 2012).

Nomenclature

AHRS	Attitude and Heading Reference System
AMMA	African Monsoon Multidisciplinary Analyses
BTD	Brightness Temperature Difference
CALIOP	Cloud-Aerosol LIdar with Orthogonal Polarization
CALIPSO	Cloud-Aerosol Lidar and Infrared Pathfinder Satellite Observations
CFC	ChloroFluoroCarbon
CGA	Curtis-Godson Approximation
CI	Cloud Index
CLaMS	Chemical Lagrangian Model of the Stratosphere
CRISTA	Cryogenic Infrared Spectrometers and Telescopes for the Atmosphere
CRISTA-NF	Cryogenic Infrared Spectrometers and Telescope for the Atmosphere - New Frontiers
CTM	Chemistry Transport Model
ECMWF	European Centre for Medium-range Weather Forecasts
EGA	Emissivity Growth Approximation
EU	European Union
FOV	Field Of View

FOZAN	Fast OZone ANalyzer
FP-7	7th Framework Programme
FWHM	Full Width at Half Maximum
HAGAR	High Altitude Gas AnalyzeR
HIRDLS	HIgh-Resolution Dynamics Limb Sounder
HITRAN	HIgh resolution TRANsmission
HRS	High Resolution Spectrometer
IMW	Integrated Micro Window
JFM	Jurassic Forward Model
JURASSIC	JUelich RApid Spectral SImulation Code
LiDAR	Light Detection And Ranging
LOS	Line Of Sight
LRS	Low Resolution Spectrometer
MIPAS-ENV	Michelson Interferometer for Passive Atmospheric Sounding-ENVisat
MIPAS-STR	Michelson Interferometer for Passive Atmospheric Sounding-STRatospheric aircraft
mPV	modified Potential Vorticity
NAT	Nitric Acid Trihydrate
NI	NAT Index
PSC	Polar Stratospheric Cloud
PV	Potential Vorticity
PVU	Potential Vorticity Unit

RECONCILE	Reconciliation of essential process parameters for an enhanced predictabilty of arctic stratospheric ozone loss and its climate interactions
RFM	Reference Forward Model
SCOUT-O3	Stratospheric-Climate Links with Emphasis on the Upper Troposphere and Lower Stratosphere
Si:Ga	Gallium-doped Silicium
SPAS	Shuttle PAllet Satellite
STS	Supercooled Ternary Solution
TH	Tangent Height
TP	Tangent Point
UCSE	Unit for Connection with Scientific Equipment
UTC	Universal Time Coordinated
UTLS	Upper Troposhere Lower Stratosphere
VMR	Volume Mixing Ratio

A. Calibration and LOS determination

The post-flight wavelength calibration by means of spectra measured by CRISTA-NF during the RECONCILE flights is explained in this chapter. Furthermore, the adjustments of the radiometric absolute calibration and the improvement of the LOS determination are presented.

A.1. Post-flight wavelength calibration

The relation between the output voltage of a spectrometer grating (U_{gra}) and the corresponding wavelength (λ) can be described with a quadratic function as follows (Kullmann, 2006):

$$\lambda(U_{gra}) = a + b \cdot U_{gra} + c \cdot U_{gra}^2 \qquad (A.1)$$

During the laboratory calibration absorption spectra of the infrared active gas NH_3 are measured. These spectra are then compared with calculations by the Reference Forward Model (RFM; Dudhia et al., 2002) to determine the parameters a, b and c (e.g. Kullmann, 2006; Schroeder et al., 2009). Thus, one set of calibration parameters for all measurements is obtained by means of this calibration measurements.

Since this approach is not accurate enough for the purpose of highly precise retrievals, a post-flight wavelength calibration is performed to obtain improved parameters. The calibration parameters are determined by fitting spectra measured by CRISTA-NF during measurement flights to simulated spectra utilising the RFM (Weigel, 2009). As input data for the RFM calculations a combination of CLaMS (Chemical Lagrangian Model of the Stratosphere; McKenna et al., 2002b,a; Konopka et al., 2004, 2007) results and climatological values taken from the MIPAS reference climatology by Remedios et al. (2007) are used. Representative and realistic atmospheric profiles for several atmospheric trace gases (e.g. O_3, H_2O, CFC-11) and the conditions (temperature and pressure) during the RECONCILE campaign are generated using this two data sets.

The scanning direction of the gratings is reversed after each spectrum. Thus, two different types of spectra were measured during the flights, hereafter called forward and backward spectra. The relation between the wavelength and the output voltages of the gratings is different for the two spectra types. The determination of the calibration parameters is therefore performed separately for each of those spectra types and for each flight. Hence, one set of calibration parameters is obtained per flight and spectra type.

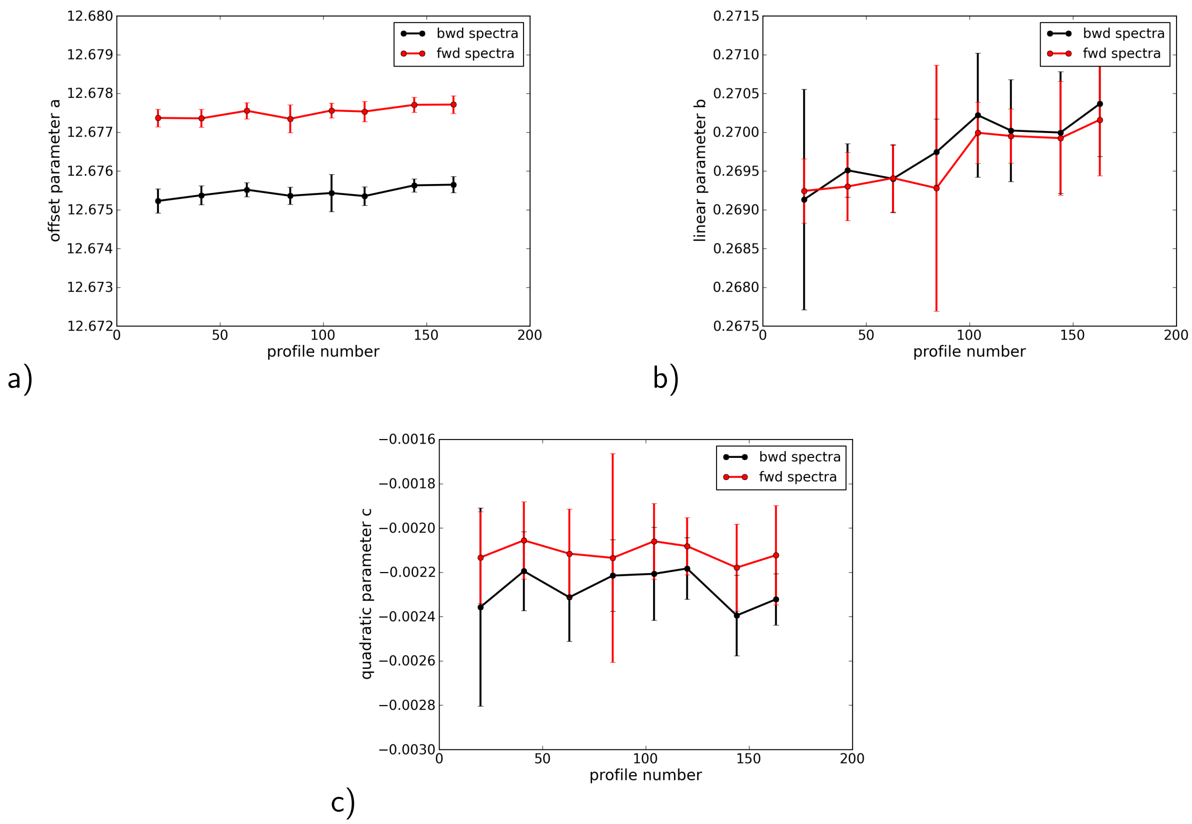

Figure A.1: Calibration parameters obtained from post-flight wavelength calibration for flight 11. The parameters for backward (bwd) spectra are displayed in black and for forward (fwd) spectra in red. The error bars show the standard deviation of the displayed average values.

After a first calibration retrieval the obtained retrieval results are used for a final refinement of the calibration parameters and the described approach is repeated using the retrieved profiles as input for the RFM calculations. Information about trace gases, which are not retrieved but necessary for the fitting process, are taken from CLaMS results and the climatology by Remedios et al. (2007). The fitting process is performed for up to 10 selected altitude scans distributed over the particular flight and the average values of the calibration parameters for each altitude scan are determined.

The refinement of the calibration parameters by means of retrieval results is performed for the RECONCILE flights 10 and 11. Fig. A.1 displays the final calibration parameters for flight 11. Some of the derived calibration parameters are nearly constant, whereas other parameters show a significant trend (e.g. linear parameter b). Thus, a linear fit is calculated for each derived parameter to account for this obvious trends.

Since no retrieval results are available for flight 1 - 5 (discussed in Chap. 4), only the post-flight wavelength calibration without refinement is performed. Nevertheless, trends are taken into account if necessary.

A.2. Radiometric absolute calibration

This section presents the adjustments of the radiometric absolute calibration for the RECONCILE aircraft campaign. The calibration procedure is described by Kullmann (2006) and Schroeder et al. (2009) in detail.

The incoming radiance is measured by a number of cryogenic semiconductor detectors (Si:Ga) and the detector signals are recorded in voltages. A set of calibration parameters is therefore necessary to calculate meaningful physical values ($\mathrm{W/(cm^2\,sr\,cm^{-1})}$). The empirical expression, which describes the relation between the recorded voltages and the radiance, is given by

$$\log_{10} \mathrm{I} = \mathrm{a}(\log_{10} \mathrm{U_{det}})^{\mathrm{p}} + \log_{10} \mathrm{U_{det}} + \mathrm{c}, \tag{A.2}$$

where I is the radiance, $\mathrm{U_{det}}$ the detector voltage, p a constant parameter for each detector and a and c the calibration parameters (Preusse, 1995). These calibration parameters are determined by comparisons between black body emission measurements and the theoretical black body emissions (Schroeder et al., 2009).

CRISTA-NF is covered by a ZnSe-window from the surrounding air masses. Since no calibration measurements without window were performed during RECONCILE (which is in contrast to former campaigns (e.g Schroeder et al., 2009; Weigel, 2009)), the influence of this window has to be taken into account. The radiance inside CRISTA-NF ($\mathrm{I_{CRNF}}$) during the calibration measurements can be described as

$$\mathrm{I_{CRNF}}(\lambda) = \epsilon_{\mathrm{BB}} \cdot \tau_{\mathrm{WIN}}(\lambda) \cdot \mathrm{P_{BB}}(\mathrm{T_{BB}}, \lambda) + \epsilon_{\mathrm{WIN}}(\lambda) \cdot \mathrm{P_{WIN}}(\mathrm{T_{WIN}}, \lambda), \tag{A.3}$$

with the emissivity ϵ_{WIN} and transmissivity τ_{WIN} of the window, the emissivity ϵ_{BB} of the black body, the black body temperature T_{BB}, the window temperature T_{WIN}, the radiance of the black body P_{BB} and the radiance emitted by the window P_{WIN}. The emissivity and transmissivity of the window are taken from the AMMA-SCOUT-O3 calibration (see Schroeder et al., 2009).

Since a measurement of the window temperature was not possible during the calibration measurements, the temperature has to be estimated and adjusted after the calibration. The adjustment was obtained by avoiding negative radiance errors only caused by an overestimation of the window influence. Thus, the window temperature was appointed to 270 K for the calibration before the first RECONCILE phase and to 265 K for the calibration before the second phase (personal communication: S.Höfer).

It is possible that the detector temperature increases during a flight due to sun light coming into the instrument or decreasing liquid helium. The calibration procedure is performed for four different temperatures in the range from 13.0 K (nominal detector temperature) to 14.5 K in 0.5 K temperature steps, because the calibration parameters depend on the detector temperature (Schroeder et al., 2009).

The adjustment of the calibration procedure leads to a larger systematic relative error (instrument gain). Comparisons between measured radiance values, which are calculated by means of the obtained calibration parameters, and the theoretical emissions of the black body show a systematic relative error of 2 % (in former studies 1 % (compare Weigel, 2009)).

The noise of the detectors is in the order of magnitude of a few tenth per cent (Weigel, 2009). However, a noise error of 1 % is assumed to account for other stochastic errors in the retrieval process, like minimal wavelength errors.

A.3. Determination of time shift between UCSE and CRISTA-NF

An obvious time shift between the UCSE recordings and the CRISTA-NF measurements has to be corrected. This time shift is determined using a simple correlation method described by Weigel (2009). The roll angles measured by the CRISTA-NF AMS (Attitude Measurement System) and recorded by the UCSE are used for the comparisons.

In a first step an estimate for the time shift is obtained by means of comparisons of clearly visible features, which are for example caused by aircraft turns.

In a second step a correlation method is used for the final determination of the time shift. The correlation between the two roll angle measurements is calculated for different time shifts around the first estimate. The time shift, which corresponds to the maximum correlation value, is stated to be the correct time shift. The procedure is performed for each profile separately. An analysis of Weigel (2009) showed that the time shifts determined for different profiles differ not more than 0.5 s for the most flights. This difference is lower than the time resolution of the UCSE recordings (time resolution = 1 s) and one time shift (mean of all profiles) is used. The procedure is performed for each flight of the RECONCILE campaign.

A.4. Improvement of LOS determination

In this section the three procedures for the improvement of the LOS determination by means of the MIPAS-STR AHRS measurements are described. A description of the MIPAS-STR AHRS is given by Keim (2002).

In a first step an obvious time shift between the MIPAS-STR AHRS measurements and the UCSE recordings has to be corrected to obtain a compatible set of quantities, because only the pitch and roll angle measurements of the MIPAS-STR AHRS are used. The remaining information (yaw angle and aircraft location) are taken from the UCSE recordings. After the time correction, the MIPAS-STR AHRS roll and pitch angles are corrected onto the reference system of CRISTA-NF. Previously, the CRISTA-NF AMS measurements have to be corrected with respect to an angle offset and a temperature dependence of the pitch angle.

A.4.1. Determination of time shift

The time shift between the MIPAS-STR AHRS measurements and the UCSE recordings is determined similar as described in Sect. A.3. Since the time shift is close to zero seconds, this value can be used as a first estimate. The final time shift is then determined by a comparison between the UCSE roll angle and the MIPAS-STR AHRS pitch angle. Due to a rotation of the MIPAS-STR AHRS of nearly 90° with respect to the flight direction these two angles show to a very good approximation the same quantity. The same is true for the MIPAS-STR AHRS roll angle (negative value) and the UCSE (and CRISTA-NF AMS) pitch angle.

The MIPAS-STR AHRS pitch angle measurements (recorded with 128 Hz) are shifted in time in 0.01 s steps around the first estimate of zero seconds. After adding an offset value of 0.5326° (UCSE roll angle - MIPAS-STR AHRS pitch angle; personal communication: W. Woiwode) to the MIPAS-STR AHRS pitch angle, the MIPAS-STR AHRS measurements are interpolated onto the UCSE time grid. Finally, the correlation between the MIPAS-STR AHRS pitch angle and the UCSE roll angle is calculated for each assumed time shift. The time shift, which shows the maximum correlation value, is then assumed to be the correct time shift between these two measurements. One time shift for each flight (if MIPAS-STR AHRS measurements are available) is determined by using this approach.

A.4.2. Offset during LOS calibration and temperature dependence of the CRISTA-NF pitch angle

A correction of the CRISTA-NF attitude measurements is necessary to be able to correct the MIPAS-STR AHRS measurements onto the reference system of CRISTA-NF. A temperature dependence of the CRISTA-NF AMS pitch angle and angle offsets with respect to the CRISTA-NF initial calibration position have to be taken into account (Weigel, 2009).

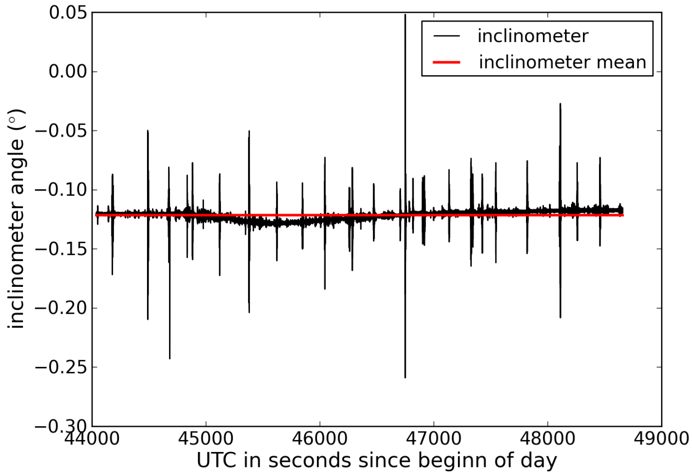

Figure A.2: Offset of the CRISTA-NF AMS inclinometer during the LOS calibration.

During the LOS calibration the CRISTA-NF instrument is adjusted to its initial position, in which the instrument is orientated with respect to the Earth's gravity acceleration vector, utilising theodolites. In this position the CRISTA-NF AMS roll and pitch angle should be zero. The LOS is calculated by means of the instrument attitude, which is described by the rotation angles roll, pitch and yaw, and the viewing direction. Thereby, the viewing direction is calculated by means of the calibration parameters obtained from the LOS calibration and the mirror position. Thus, remaining angle offsets with respect to the initial position have to be determined and taken into account in the LOS calculation.

The roll angle offset is determined utilising the CRISTA-NF AMS inclinometer measurements. A mean offset of -0.122° is visible during the LOS calibration (see Fig. A.2). This value has to be subtracted from all other inclinometer measurements used in the following calculations to correct the measurements with respect to the initial position of the instrument and therefore with respect to the LOS calibration.

The CRISTA-NF AMS pitch angle is calculated utilising the accelerometer measurements. Fig. A.3 displays the temperature dependence of the pitch angle in panel a). This dependence can be approximated by a linear expression (displayed as red line), which is now used to account for the offset during the LOS calibration as well as the temperature dependence.

The pitch angle measurements during the LOS calibration are depicted in Fig. A.3 panel b), on the one hand, without correction (black) and, on the other hand, with correction (red). The measurements without correction show a non constant behaviour caused by different temperatures of the electronics during the calibration and an offset with respect to zero. After the correction both the temperature dependence and the offset are removed.

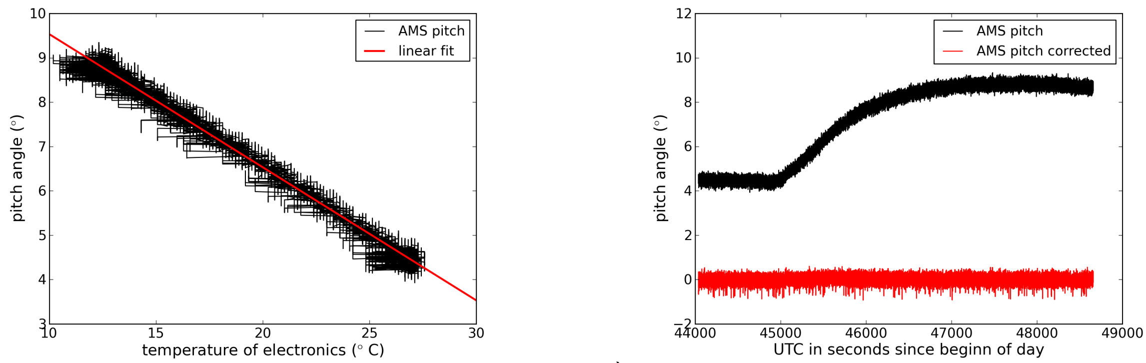

a) b)

Figure A.3: Temperature dependence of the CRISTA-NF AMS pitch angle (a)) and offset of the pitch angle during the LOS calibration (b)). The pitch angle during the LOS calibration without correction is depicted in black and with correction in red.

The determined linear expression is used in the following calculations to correct all CRISTA-NF AMS pitch angle measurements with respect to the initial calibration position.

A.4.3. Offset correction between MIPAS-STR and CRISTA-NF

In the last step the offsets between the MIPAS-STR AHRS and the CRISTA-NF AMS roll and pitch angle measurements are determined to correct the MIPAS-STR AHRS measurements onto the CRISTA-NF reference system. In former studies Weigel (2009) used the angle offsets between the UCSE recordings and the CRISTA-NF AMS measurements to correct the UCSE recordings. Since the CRISTA-NF AMS inclinometer (roll angle) measurements are only valid in times, in which the instrument is not moving (because of inertia), the comparisons between the two instruments are performed before takeoff, while the aircraft is standing on ground.

The rotation sequence (transformation from instrument to Earth: roll, pitch, yaw) is interchanged for the MIPAS-STR AHRS measurements, because the MIPAS-STR AHRS pitch angle is used instead of the CRISTA-NF AMS or UCSE roll angle and vice versa (because of the rotation of the MIPAS-STR AHRS of 90° with respect to the flight direction). However, the MIPAS-STR AHRS pitch and roll angles are only slightly different from zero during a flight, except for the ascent (descent) or a turn, and the errors caused by an interchange are negligible.

The transformation from one reference system to another is actually a rotation. Here this transformation is approximated by determining angle offsets and using them for correction. The errors caused by this approximation are very small for small rotation angles, which is here the case. Furthermore, the uncertainties of the CRISTA-NF AMS measurements (due to noise and aircraft vibrations) are much larger than the errors typically caused by the approximation (see Fig. A.4).

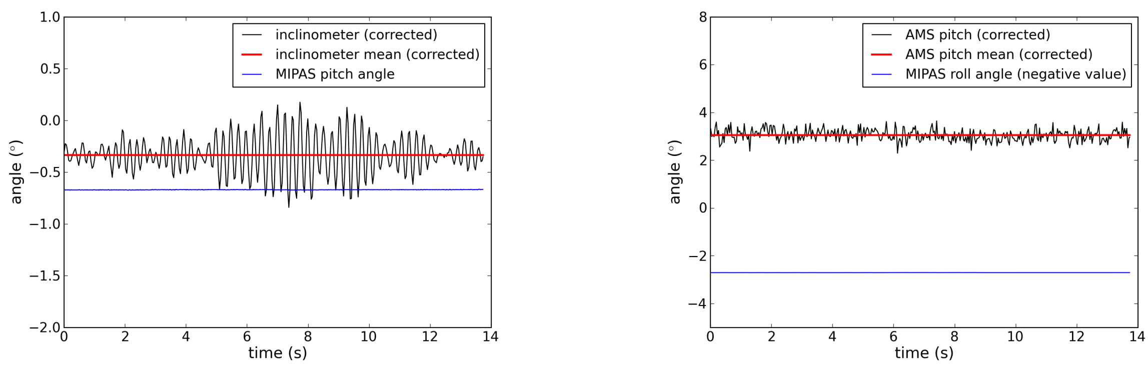

a) b)

Figure A.4: Offsets between the MIPAS-STR AHRS and the CRISTA-NF AMS measurements before flight 11 on March 2, 2010.

Fig. A.4 panel a) shows the comparison between the CRISTA-NF inclinometer measurements (corrected with respect to the initial position) and the MIPAS-STR AHRS pitch angle measurements before flight 11. The fluctuations of the inclinometer measurements are caused by aircraft vibrations but the measurements vary around a constant value. Thus, the mean of the inclinometer measurements in this time period is used to determine the offset.

The measurements of the CRISTA-NF AMS pitch angle and the MIPAS-STR AHRS roll angle (negative value) are shown in panel b). The CRISTA-NF AMS measurements show noise and the mean of the measurements is therefore used for the offset determination. For each flight the offsets for two phases before take off are determined and the mean offsets are taken for correction.

A.4.4. Final data set

The MIPAS-STR AHRS measurements are now corrected in time (with respect to the UCSE recordings) and the offsets between the MIPAS-STR AHRS measurements and the CRISTA-NF AMS measurements are taken into account. Furthermore, the MIPAS-STR AHRS measurements are interpolated onto the UCSE time grid and merged with the UCSE recordings (yaw angle and aircraft location) to obtain a full data set, which contains all angle measurements and the aircraft location. This data set is used for the LOS calculation for RECONCILE flight 10 and 11. The time shift between the UCSE recordings and the CRISTA-NF measurements is known from the comparisons discussed in Sec. A.3. Since an approximative method is used and the CRISTA-NF AMS measurements show large fluctuations and noise, the correction of the angle measurements is validated in the retrieval process (see Sec. 5.2).

For flight 1 - 5 (discussed in Chap. 4) no MIPAS-STR AHRS measurements are available. Thus, only the UCSE recordings are used for LOS calculation. Nevertheless, angle offsets between the UCSE recordings and the CRISTA-NF AMS measurements are determined similar as described in Sec. A.4.3 and taken into account.

B. Retrieval

B.1. Mathematical descriptions

Here some mathematical descriptions are summarised (see also Rodgers, 2000).

The gain matrix is defined as

$$G = \left(S_a^{-1} + F'(\boldsymbol{x}_f)^T S_\epsilon^{-1} F'(\boldsymbol{x}_f) \right)^{-1} F'(\boldsymbol{x}_f)^T S_\epsilon^{-1}, \tag{B.1}$$

where $\boldsymbol{x}_f$ denotes a solution of the retrieval. The averaging kernel matrix is the matrix product of the gain matrix and the Jacobian matrix $F'(\boldsymbol{x}_f)$ and therefore

$$A = GF'(\boldsymbol{x}_f) = \left(S_a^{-1} + F'(\boldsymbol{x}_f)^T S_\epsilon^{-1} F'(\boldsymbol{x}_f) \right)^{-1} F'(\boldsymbol{x}_f)^T S_\epsilon^{-1} F'(\boldsymbol{x}_f). \tag{B.2}$$

B.2. Forward model

The forward model errors are estimated by comparisons of the used forward model (JFM) and an exact line-by-line model. Tab. B.1 summarises the errors for the different used IMWs. The standard deviation between the JFM results and results of an exact line-by-line model is reduced significantly from up to 1 % to at most 0.22 % by using the regression scheme and the mean bias is reduced down to 0.02 % (see also Ungermann et al., 2012).

Table B.1: Summary of the forward model errors in the different used integrated micro windows.

integrated micro window	spectral range (cm^{-1})	forward model error (%)
1	777.5 - 778.5	0.05
2	784.0 - 785.0	0.07
3	787.0 - 790.0	0.06
4	791.5 - 793.0	0.03
5	794.1 - 795.0	0.08
6	795.5 - 796.5	0.08
7	796.6 - 797.5	0.08
8	808.0 - 809.0	0.08
9	810.0 - 813.0	0.08
10	820.5 - 821.5	0.12
11	831.0 - 832.0	0.22
12	846.0 - 847.0	0.10
13	863.0 - 866.0	0.04

C. RECONCILE flight 10

The retrieval results for flight 10 are presented and briefly discussed in this chapter. Furthermore, the CLaMS results for this flight are shown and compared to the CRISTA-NF observations.

C.1. Flight path and conditions

The local flight 10 started in Kiruna at approximately 3:00 UTC and ended in Longyearbyen on Spitsbergen. The flight consisted of three different legs. The first one was orientated towards North, the second towards northwest and the last towards southwest (see Fig. C.1 a)). The highest altitudes of 18 km were reached at the end of the flight (see Fig. C.1 b)).

Additionally, the cloud index (see Sec. 4.1) is displayed at the tangent points of the CRISTA-NF measurements as a measure for the optical conditions. Tropospheric clouds are visible below $\approx$ 9 km during this flight, whereas the measurements above this altitude show no influence of clouds. Thus, most of the measurements provide a good basis for highly precise retrievals.

The meteorological situation is shown in Fig. C.2. Panel a) depicts the ECMWF potential vorticity at 70 mbar. This pressure level is nearly equivalent to the flight altitude of the aircraft at the end of the flight. The region showing the highest PV values is located southeast of Longyearbyen and shows the polar vortex. Thus, the aircraft entered the vortex on the way to Spitsbergen.

The situation at the tangent points of the CRISTA-NF measurements is illustrated in Fig. C.2 panel b). The plot shows the modified PV at the CRISTA-NF tangent points. Two distinct areas with high mPV values are visible. The first one is located immediately below flight altitude at the end of the flight and exhibits very high values of mPV greater than 20 PVU, which indicates the polar vortex. Furthermore, the vertical extent of this area is different during different time periods. The observed differences are caused by the three different viewing directions of CRISTA-NF at the end of the flight (see Fig. C.1 a)). The instrument therefore observed different parts of the polar vortex. The two turns of the aircraft are indicated in Fig. C.2 b) by the white vertical strokes showing the lack of measurements during the turns.

The second area with higher values of mPV is located in the middle of the flight in the altitude range from 13 to 14 km. This area shows values of mPV between 16 and 17 PVU, which are obviously lower than the values in the polar vortex but higher than those of the surrounding air masses. These comparable high values of mPV most likely indicate air masses, which contain a large amount of vortex air masses.

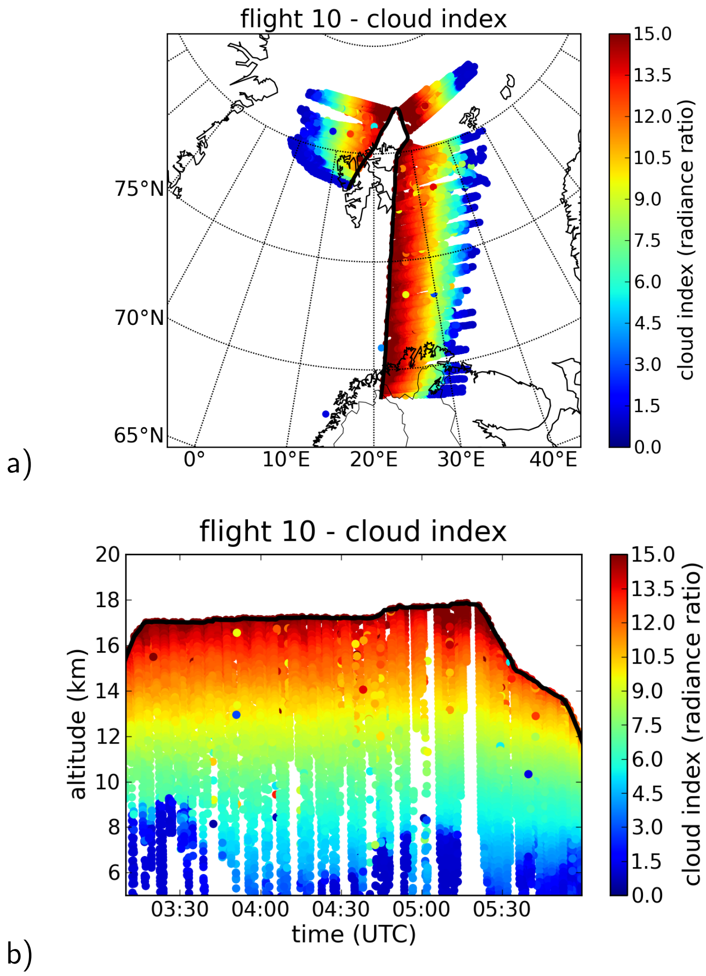

Figure C.1: Latitude-longitude plot (a)) and vertical cross section (b)) of the CRISTA-NF cloud index during flight 10. The flight path of the aircraft is marked by a solid black line.

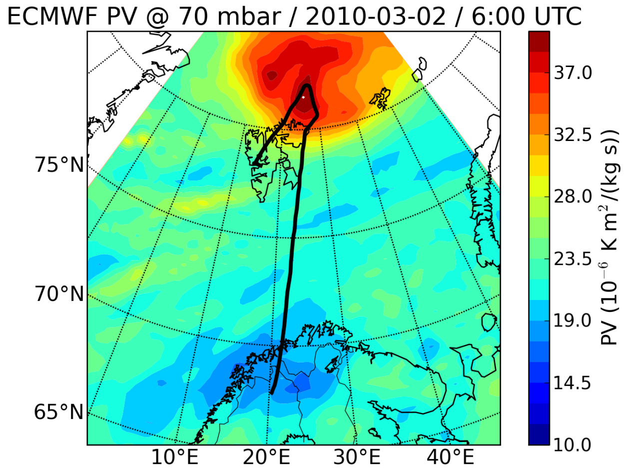

a)

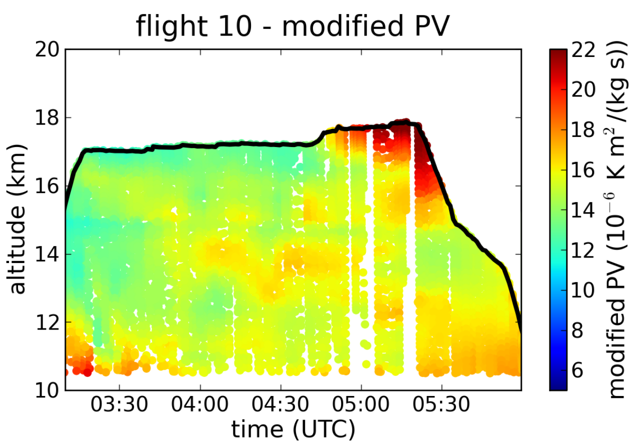

b)

Figure C.2: ECMWF potential vorticity at 70 mbar at 6:00 UTC on 2010-03-02 (a)) and modified potential vorticity at the CRISTA-NF tangent points (b)) for flight 10. The flight path of the aircraft is marked by the solid black line.

C.2. Validation

This section briefly presents the comparison between the CRISTA-NF retrieval results for ozone and CFC-11 and the in-situ measurements by HAGAR and FOZAN.

The ozone volume mixing ratios at flight altitude derived from the CRISTA-NF measurements (blue) and measured by FOZAN (red) are displayed in Fig. C.3. Both measurements are in a very good agreement, except for some differences caused by the different measurement techniques of the instruments.

The high volume mixing ratios measured by FOZAN at 4:50 UTC, for example, show the observation of a structure with small horizontal extent (compare Fig. C.4 at around 78.5° North). This small scale structure is not fully resolved by the CRISTA-NF measurements, because of the limb sounding measurement technique.

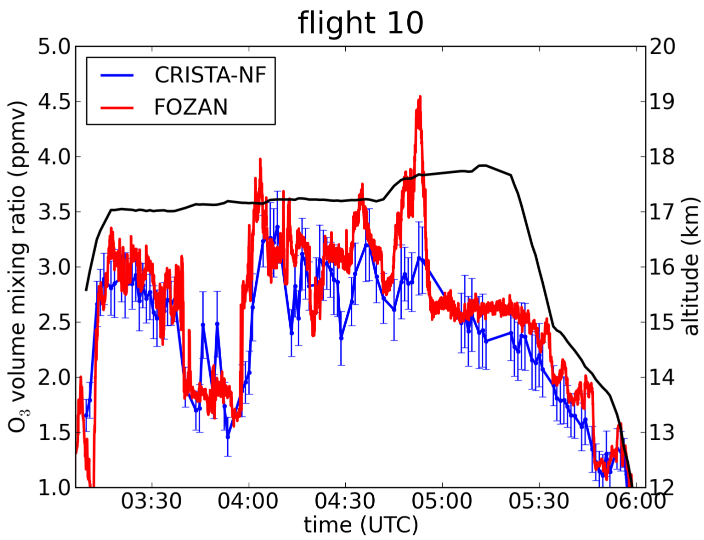

Figure C.3: Comparison between the CRISTA-NF retrieval results for ozone (blue) and in-situ measurements by FOZAN (red) at flight altitude for RECONCILE flight 10. The errors bars for CRISTA-NF show the total+smooth error and the FOZAN measurements have a relative error less than 10 % (e.g. Ulanovsky et al., 2001). The flight altitude is depicted as solid black line with an axis on the right side. FOZAN data: courtesy of A. Ulanovsky and F. Ravegnani

The obvious shift in the observation time of some structures, e.g. at 4:15 UTC and 4:40 UTC, is caused by the horizontal orientation of the observed filaments, which is not orthogonal to the flight direction (see Fig. C.4).

Fig. C.5 shows the comparison between the CRISTA-NF retrieval results for CFC-11 and the HAGAR measurements. In general both measurements agree well, except for the same shifts in the observation time of small structures and obvious differences at the beginning of the flight.

During the first half of the flight CRISTA-NF overestimates the CFC-11 volume mixing ratios. But due to the very inhomogeneous atmosphere during this time period (visible in the distribution of potential vorticity north of Kiruna; Fig. C.2 a)) this is at least partly caused by the viewing geometry of CRISTA-NF.

The difference visible between 4:45 UTC and 5:15 UTC is additionally caused by the viewing geometry of CRISTA-NF. At 4:45 UTC the aircraft enters the polar vortex and HAGAR

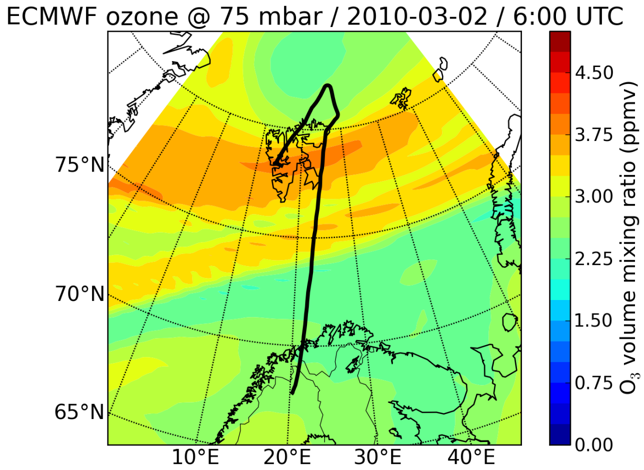

Figure C.4: ECMWF ozone volume mixing ratios at 75 mbar at 6:00 UTC on 2010-03-02. The flight path is depicted as solid black.

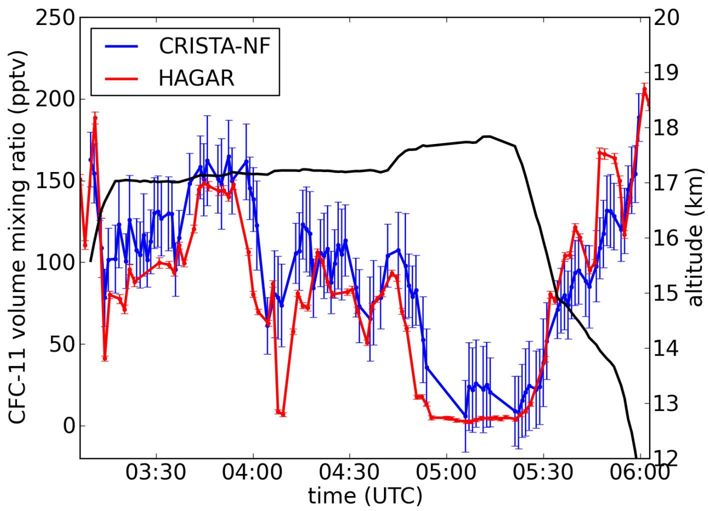

Figure C.5: Comparison between the CRISTA-NF retrieval results for CFC-11 (blue) and in-situ measurements by HAGAR (red) at flight altitude for RECONCILE flight 10. The errors bars show the total+smooth error for CRISTA-NF and the absolute accuracy for HAGAR. The flight altitude is depicted as solid black line with an axis on the right side. HAGAR data: courtesy of E. Hösen and C.M. Volk

observes a steep decrease in the CFC-11 VMRs. CRISTA-NF by contrast observes air masses from inside as well as from outside the vortex during this time, which leads to a slower decrease in CFC-11 VMRs. The horizontal distribution of PV shows that the instrument views from an area with high PV to an area with lower PV (see Fig. C.2 a) and Fig. C.1 a)).

However, the good agreement of the retrieval results and the in-situ measurements illustrates the reliability of the CRISTA-NF retrieval results.

C.3. Retrieval results

The CRISTA-NF retrieval results for CFC-11, ozone, $ClONO_2$ and HNO_3 are presented and discussed in this section. Furthermore, the ozone-CFC-11-relation is used to identify air masses with a large amount of vortex air.

Fig. C.6 shows the CRISTA-NF retrieval results for flight 10. The corresponding total+smooth errors are shown in Fig. C.7. The relative error of CFC-11 is usually between 10 and 15 %, except for areas with very low CFC-11 VMRs, e.g. at the end of the flight. There the relative error increases and reaches up to 100 % at some points at flight altitude. However, the comparison with the HAGAR measurements (see Fig. C.2) shows that the CFC-11 VMRs in these areas are reliable as well. The observed structures in the cross sections of the total+smooth errors are most likely caused by aircraft movements. These aircraft movements lead to larger errors in the corresponding profile.

The two structures observed in the distribution of mPV (see Fig. C.2 b)) are visible in the cross section of CFC-11 too. These structures are indicated by comparable low CFC-11 volume mixing ratios. The lowest VMRs (< 20 pptv) are visible in the area immediately below the flight altitude at the end of the flight. Together with the high values of mPV in the same area this is a reliable indicator for the polar vortex. Furthermore, the three steps observed in the distribution of mPV can be seen in the cross section of CFC-11 as well. Due to the different viewing directions of CRISTA-NF during this part of the flight the instrument looked into different parts of the polar vortex. As indicated by the steps in the cross sections of mPV and CFC-11 the vertical extent of the polar vortex was considerable different.

The second structure with low CFC-11 volume mixing ratios is located in the middle of the flight at around 14 km. The CFC-11 VMRs are higher than in the region identified as polar vortex but significant lower than the CFC-11 VMRs of the surrounding air masses. Taking into account the comparable high values of mPV in this structure (see Fig. C.2 b)) of about 16 - 17 PVU this indicates air masses consisting of a noticeable fraction of air originating from the polar vortex. Thus, CRISTA-NF observed the polar vortex and a filament with a large fraction of vortex air during flight 10.

The cross sections of $ClONO_2$ and ozone (Fig. C.6 b) and c)) confirm these observations.

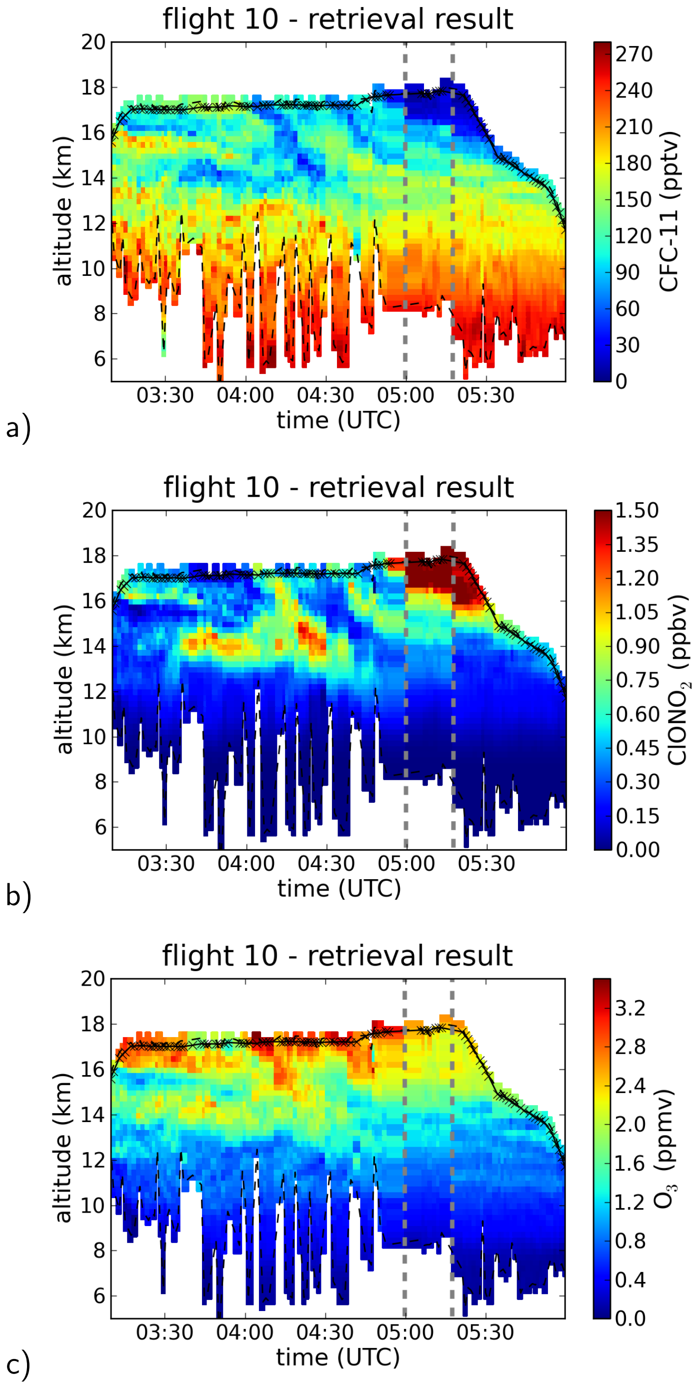

Figure C.6: Retrieval results of the CRISTA-NF measurements for the trace gases CFC-11 (a)), $ClONO_2$ (b)), and O_3 (c)) for flight 10. The solid black line shows the flight altitude and the dashed black lines the lowest and highest tangent height of a valid measurement. The position (time) of each profile is marked by a black cross. Different viewing directions of the instrument are separated by a grey dashed line.

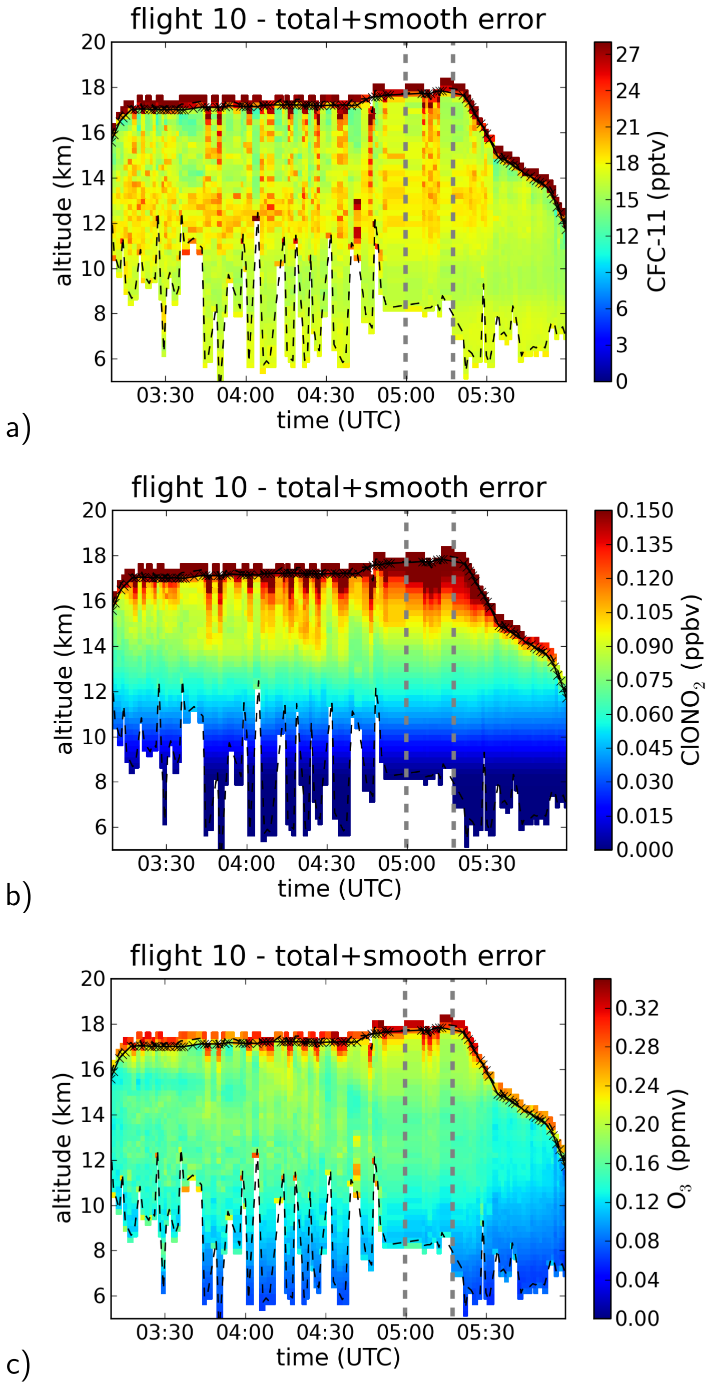

Figure C.7: Cross sections of the total+smooth error for the trace gases CFC-11 (a)), $ClONO_2$ (b)), and O_3 (c)) for flight 10. The solid black line shows the flight altitude and the dashed black lines the lowest and highest tangent height of a valid measurement. The position (time) of each profile is marked by a black cross. Different viewing directions of the instrument are separated by a grey dashed line.

Inside the polar vortex the $ClONO_2$ VMRs exhibit the highest measured values. Additionally, the volume mixing ratios inside the filament are significant higher than in the surrounding air masses. This is a consequence of the chlorine deactivation inside vortex air masses after the PSC existence and the cold phase of the vortex (see Sec. 2.3 and Sec. 6.2.2).

The ozone VMRs inside the polar vortex at the end of the flight are lower/equal to the VMRs outside the vortex at comparable altitudes, because of the ozone depletion inside the vortex (see Sec. 2.3 and Sec. 6.2.2).

In order to analyse the air masses inside the filament in terms of the air mass origin in more detail, the ozone-CFC-11-relation can be used (compare Sec. 6.2.4). Fig. C.8 shows the ozone VMRs versus the CFC-11 VMRs for two regions, the polar vortex and the filament in the middle of the flight. The vortex relation shows measurements inside the polar vortex after 5:00 UTC (first turn of the aircraft illustrated by a grey dashed line in Fig. C.6). The measurements inside the filament are selected according to time, altitude and a threshold value for the CFC-11 VMRs of 100 pptv.

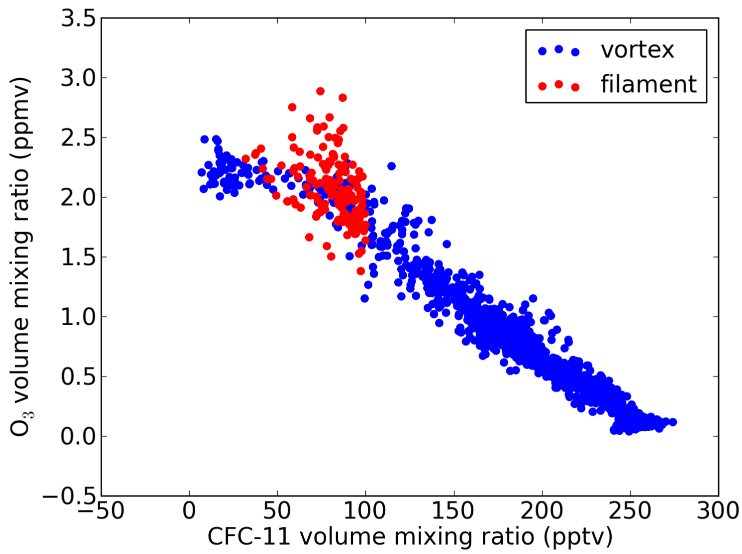

Figure C.8: Scatter plot of ozone VMR vs. CFC-11 VMR for flight 10 for the two regions: vortex (blue) and filament in the middle of the flight (red).

A large part of the measurements inside the filament exhibit the same ozone-CFC-11-relation than inside the polar vortex. This confirms, that the air masses inside the filament contain a large amount of air masses originating from the polar vortex.

Fig. C.9 shows the cross section of HNO_3 in panel a) and the corresponding total+smooth errors in panel b). In the altitude range between 14.5 km and 16.5 km inside the polar vortex an enhancement of the HNO_3 volume mixing ratios is clearly visible, whereas the volume mixing ratios at flight altitude are significantly lower. This illustrates the de- and renitrification of the stratosphere by sedimentation of NAT particles (compare Sec. 2.2 and Sec. 6.2.2).

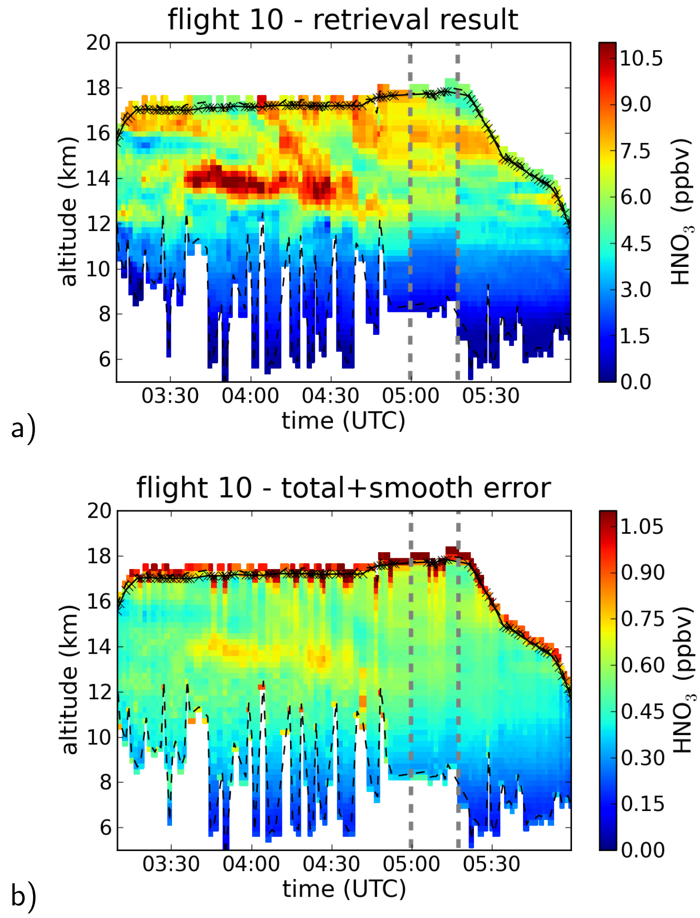

Figure C.9: Retrieval results of the CRISTA-NF measurements for the trace gas HNO_3 (a)) for flight 10 and the corresponding total+smooth error (b)). The solid black line shows the flight altitude and the dashed black lines the lowest and highest tangent height of a valid measurement. The position (time) of each profile is marked by a black cross. Different viewing directions of the instrument are separated by grey dashed lines.

C.4. CLaMS results

This section presents the CLaMS results for CFC-11, $ClONO_2$, ozone, and HNO_3 for flight 10. A description of CLaMS and the used setup is given in Sec. 7.1.

Fig. C.10 shows the CLaMS results for CFC-11 and $ClONO_2$ in panel a) and panel b), respectively. The cross section of CFC-11 exhibits all main structures observed by CRISTA-NF (compare Fig. C.6 a)), albeit differences in some regions are visible. For example, the region at around 4:30 UTC and 15 km showing higher CFC-11 VMRs is not fully captured by CLaMS, which is at least partly caused by the different horizontal resolution of CLaMS and CRISTA-NF. However, the general good agreement of both data sets in terms of the observed structures and absolute values illustrates the good performance of CLaMS with respect to advection and mixing.

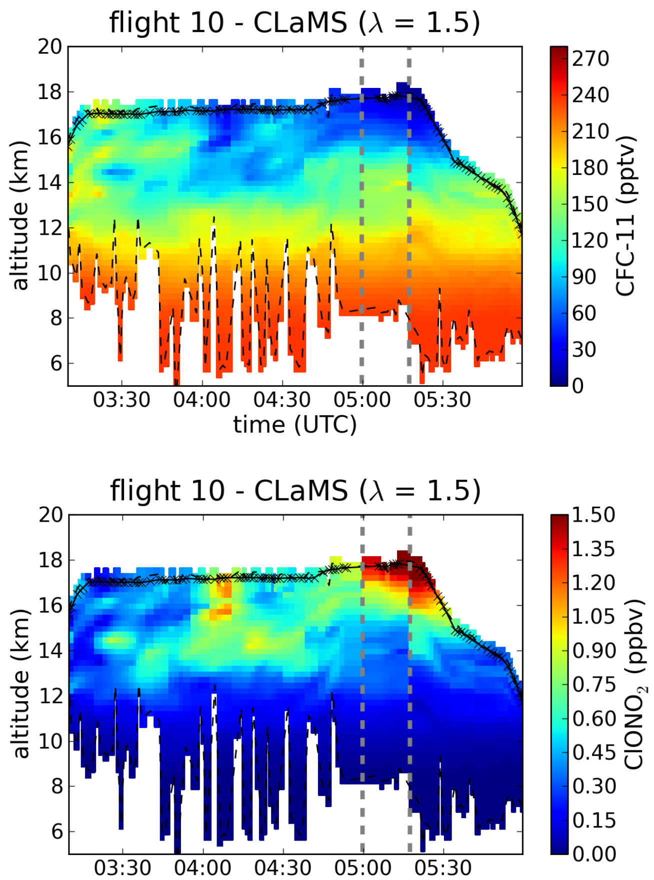

a)

b)

Figure C.10: CLaMS results for the trace gases CFC-11 (a)) and $ClONO_2$ (b)) for flight 10. The solid black line shows the flight altitude and the dashed black lines the lowest and highest tangent height of a valid measurement. The position (time) of each profile is marked by a black cross. Different viewing directions of the instrument are separated by grey dashed lines.

The comparison for $ClONO_2$ shows a slight underestimation of the volume mixing ratios inside the polar vortex and the filament in the middle of the flight (compare Fig. C.6 b)).

The same underestimation is observed for flight 11 and discussed in Sec. 6.2.2. This underestimation is a hint for an underestimation of the chlorine activation by CLaMS (compare Sec. 7.4).

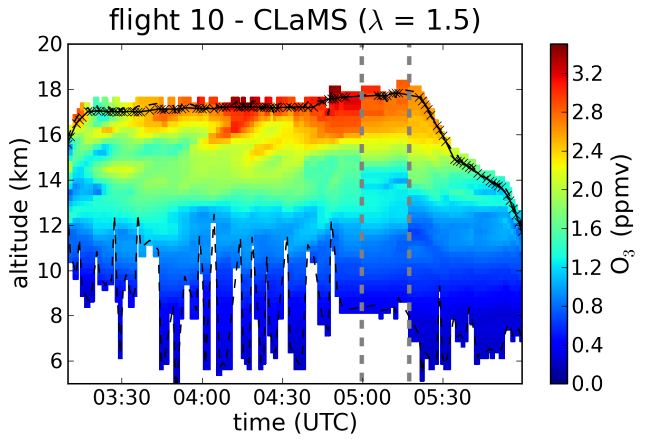

a)

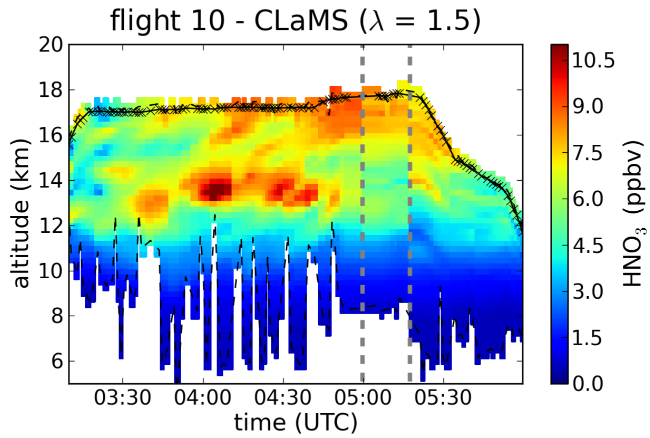

b)

Figure C.11: CLaMS results for the trace gases O_3 (a)) and HNO_3 (b)) for flight 10. The solid black line shows the flight altitude and the dashed black lines the lowest and highest tangent height of a valid measurement. The position (time) of each profile is marked by a black cross. Different viewing directions of the instrument are separated by grey dashed lines.

The CLaMS results for ozone and HNO_3 are shown in Fig. C.11 in panel a) and panel b), respectively. The results for ozone agree very well with the CRISTA-NF retrieval results, except for the air masses inside the polar vortex at the end of the flight (compare Fig. C.6 c)). Significant higher ozone VMRs in the CLaMS results are visible in this area. This difference indicates an underestimation of the ozone depletion by CLaMS, which is a consequence of an underestimation of the chlorine activation from the reservoir species HCl (compare Sec. 7.4).

The CLaMS and CRISTA-NF results for HNO_3 are in good agreement, but a difference inside the polar vortex is visible (compare Fig. C.9 a)). The lower HNO_3 VMRs at flight altitude in this area are not simulated by CLaMS. Since the lower values are a consequence of the sedimentation of NAT particles, this illustrates the complexity to simulate this process (compare Sec. 7.5).

In general, both the CLaMS and CRISTA-NF results agree well, albeit some differences indicate an underestimation of the ozone depletion and deficiencies in the estimation of the chlorine activation and deactivation.

C.5. Air mass origin

This section proceeds with the presentation of the artificial tracers of CLaMS for flight 10. The artificial tracers are initialised as described in Sec. 7.3 and are used to identify air masses of different origin. Here only the tracers initialised on January 1 are shown to exclude the vortex split event in December from the analysis (compare Sec. 7.3).

Fig. C.12 shows the vortex tracer (P3; panel a)) and the low latitude tracer (P0; panel b)) for flight 10. The vortex tracer reaches values around 0.9 inside the polar vortex. This high values show that the air masses inside the vortex contain 90 % of air masses originally originating from the polar vortex. Furthermore, the vortex tracer inside the filament in the middle of the flight exhibits values of around 0.7. This illustrates that the air masses inside the filament contain a large amount of vortex air masses, which is in a good agreement with the CRISTA-NF results.

The cross section of the low latitude tracer shows structures with high values at the beginning of the flight. This values are partly larger than 0.6 and show low latitude air masses, which were transported towards the pole. The area below 16 km and the area below 14 km correspond to structures with high CFC-11 VMRs observed by CRISTA-NF (compare Fig. C.6 a)). The high CFC-11 VMRs are therefore a consequence of a large fraction of low latitude air masses inside the observed structures.

The distributions of the artificial tracers are therefore in very good agreement with the observations by CRISTA-NF, which confirms the reliability of this concept.

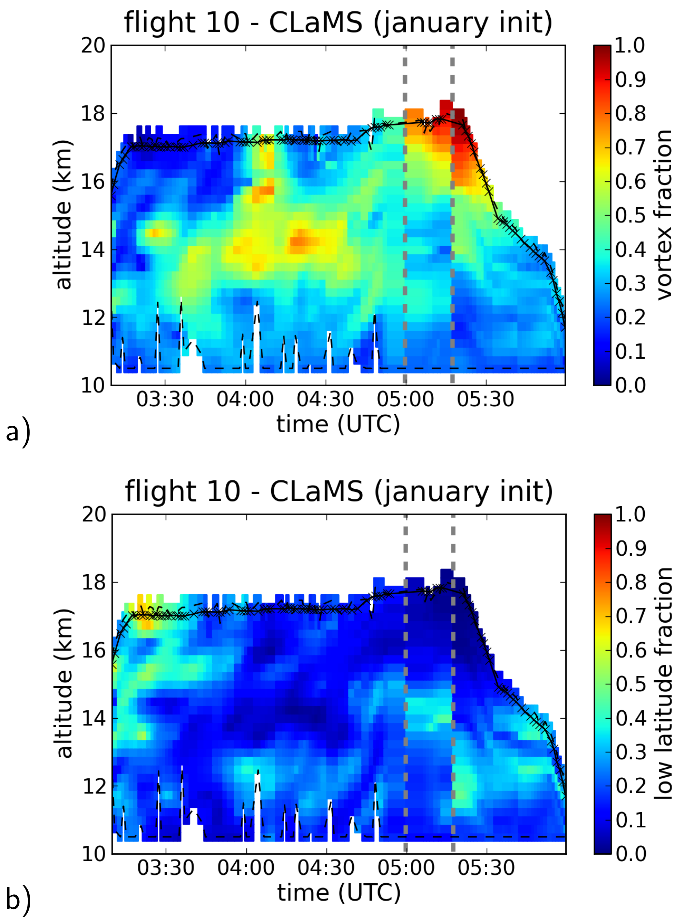

Figure C.12: CLaMS vortex tracer (a)) and low latitude tracer (b)) for flight 10 initialised on January 1. The solid black line shows the flight altitude. The position (time) of each profile is marked by a black cross. Different viewing directions of the instrument are separated by grey dashed lines.

Acknowledgements

First of all I thank Prof. Dr. Ralf Koppmann and Prof. Dr. Martin Riese for offering me the opportunity to work on this research topic and to write this thesis. Thanks also for helpful discussions and support during the whole time.

I'd like to address many thanks to the CRISTA-NF team, Friedhelm Olschewski, Peter Knieling, Hans–Peter Heuser, Dr. Sebastian Höfer, Dr. Fred Stroh, who made the CRISTA-NF measurements during RECONCILE possible. Special thanks go to Dr. Katja Weigel, who introduced me to the CRISTA-NF instrument and the data processing. Furthermore, I thank Thomas Meisehen for his work as student assistant.

Special thanks go to all people working on JURASSIC2 at IEK–7 at the Research Centre Jülich, especially Dr. Jörn Ungermann, who answered all my questions regarding the retrieval and supported me during the data analysis.

I would like to thank Dr. Reinhold Spang for helpful discussions and support with respect to the cloud analyses.

Many thanks go to the CLaMS group at IEK–7, especially Dr. Jens–Uwe Grooß and Dr. Gebhard Günther, for providing the impressive CLaMS simulation results and answering all arising questions.

Furthermore, I'd like to thank Elisabeth Hösen and Prof. Dr. C. Michael Volk for providing HAGAR data, Wolfgang Woiwode and Dr. Hermann Oelhaf for providing MIPAS-STR data, Dr. Alexey Ulanovsky and Dr. Fabrizio Ravegnani for providing FOZAN data and Dr. Michael Pitts and Dr. Lamont Poole for providing CALIOP data.

The RECONCILE project is funded by the EU under the Grant number RECONCILE-226365-FP7-ENV-2008-1. I also thank the RECONCILE Coordination and flight planning teams, MDB and Enviscope for the successful implementation of and support during the aircraft campaign.

The meteorological data used in this work were provided by the European Centre for Medium-Range Weather Forecasts (ECMWF).

Finally, I thank anybody whom I might have forgotten to mention above.

Bibliography

Bernath, P. F., McElroy, C. T., Abrams, M. C., Boone, C. D., Butler, M., Camy-Peyret, C., Carleer, M., Clerbaux, C., Coheur, P.-F., Colin, R., DeCola, P., DeMaziere, M., Drummond, J. R., Dufour, D., Evans, W. F. J., Fast, H., Fussen, D., Gilbert, K., Jennings, D. E., Llewellyn, E. J., Lowe, R. P., Mahieu, E., McConnell, J. C., McHugh, M., McLeod, S. D., Michaud, R., Midwinter, C., Nassar, R., Nichitiu, F., Nowlan, C., Rinsland, C. P., Rochon, Y. J., Rowlands, N., Semeniuk, K., Simon, P., Skelton, R., Sloan, J. J., Soucy, M.-A., Strong, K., Tremblay, P., Turnbull, D., Walker, K. A., Walkty, I., Wardle, D. A., Wehrle, V., Zander, R., and Zou, J.: Atmospheric Chemistry Experiment (ACE): Mission overview, Geophys. Res. Lett., 32, doi:10.1029/2005GL022386, 2005.

Carslaw, K., Luo, B., Clegg, S., Peter, T., Brimblecombe, P., and Crutzen, P.: Stratospheric aerosol growth and HNO_3 gas phase depletion from coupled HNO_3 and water vapor uptake by liquid particles, Geophys. Res. Lett., 21, 2479–2482, doi:10.1029/94GL02799, 1994.

Crutzen, P. J. and Arnold, F.: Nitric acid cloud formation in the cold Antarctic stratosphere: a major cause for the springtime 'ozone hole', Nature, 324, 651–655, doi:10.1038/324651a0, 1986.

Curtis, A. R.: Discussion of 'A statistical model for water vapour absorption' by R. M. Goody, Quart. J. Roy. Meteorol. Soc., 78, 638–640, 1952.

Dörnbrack, A., Pitts, M. C., Poole, L. R., Orsolini, Y. J., Nishii, K., and Nakamura, H.: The 2009/2010 Arctic stratospheric winter – general evolution, mountain waves and predictability of an operational weather forecast model, Atmos. Chem. Phys., 12, 3659–3675, doi:10.5194/acp-12-3659-2012, 2012.

Douglass, A. R., Schoeberl, M. R., Stolarski, R. S., Waters, J., III, J. M. R., Roche, A. E., and

Massie, S. T.: Interhemispheric differences in springtime production of HCl and $ClONO_2$ in the polar vortices, J. Geophys. Res., 100, 13 967–13 978, 1995.

Dudhia, A., Morris, P. E., and Wells, R. J.: Fast monochromatic radiative transfer calculations for limb sounding, J. Quant. Spectrosc. Radiat. Transfer, 74, 745–756, doi:10.1016/S0022-4073(01)00285-0, 2002.

ESA: Report for Mission Selection: PREMIER, ESA SP-1324, 3, European Space Agency, Noordwijk, The Netherlands, 2012.

Farman, J., Gardiner, B., and Shanklin, J.: Large losses of total ozone in Antarctica reveal seasonal ClOx/NOx interactions, Nature, 315, 207–210, 1985.

Fastie, W.: Ebert Spectrometer Reflections, Phys. Today, 4(1), 37–43, 1991.

Fischer, H., Birk, M., Blom, C., Carli, B., Carlotti, M., von Clarmann, T., Delbouille, L., Dudhia, A., Ehhalt, D., Endemann, M., Flaud, J. M., Gessner, R., Kleinert, A., Koopman, R., Langen, J., López-Puertas, M., Mosner, P., Nett, H., Oelhaf, H., Perron, G., Remedios, J., Ridolfi, M., Stiller, G., and Zander, R.: MIPAS: an instrument for atmospheric and climate research, Atmos. Chem. Phys., 8, 2151–2188, doi:10.5194/acp-8-2151-2008, 2008.

Francis, G. L., Edwards, D. P., Lambert, A., Halvorson, C. M., Lee-Taylor, J. M., and Gille, J. C.: Forward modeling and radiative transfer for the NASA EOS-Aura High Resolution Dynamics Limb Sounder (HIRDLS) instrument, J. Geophys. Res., 111, doi:10.1029/2005JD006270, 2006.

Gettelman, A., Hoor, P., Pan, L. L., Randell, W. J., Hegglin, M. I., and Birner, T.: The extra tropical upper troposphere and lower stratosphere, Rev. Geophys., 49, doi:10.1029/2011RG000355, 2011.

Gille, J. C., Barnett, J. J., Whitney, J. G., Dials, M. A., Woodard, D., Rudolf, W. P., Lambert, A., and Mankin, W.: The High-Resolution Dynamics Limb Sounder (HIRDLS) experiment on AURA, Proc. SPIE, 5152, 161–171, doi:10.1117/12.507657, 2003.

Glatthor, N., von Clarmann, T., Fischer, H., Funke, B., Grabowski, U., Höpfner, M., Kellmann, S., Kiefer, M., Linden, A., Milz, M., Steck, T., and Stiller, G. P.: Global peroxyacetyl nitrate (PAN) retrieval in the upper troposphere from limb emission spectra of the Michelson Interferometer for Passive Atmospheric Sounding (MIPAS), Atmos. Chem. Phys., 7, 2775–2787, doi:10.5194/acp-7-2775-2007, 2007.

Godson, W. L.: The evaluation of infra-red radiative fluxes due to atmospheric water vapour, Quart. J. Roy. Meteorol. Soc., 79, 367–379, 1953.

Gordley, L. L. and Russell, J. M.: Rapid inversion of limb radiance data using an emissivity growth approximation, Appl. Optics, 20, 807–813, doi:10.1364/AO.20.000807, 1981.

Griessbach, S.: Clouds and aerosol in infrared radiative transfer simulations for the analysis of satellite observations, Ph.D. thesis, University of Wuppertal, 2011.

Grooss, J.-U., Pierce, R. B., Crutzen, P. J., Grose, W. L., and Russell III, J. M.: Re-formation of chlorine reservoirs in southern hemisphere polar spring, J. Geophys. Res., 102, 13 141–13 152, doi:10.1029/96JD03505, 1997.

Grooß, J.-U., Günther, G., Müller, R., Konopka, P., Bausch, S., Schlager, H., Voigt, C., Volk, C., and Toon, G. C.: Simulation of denitrification and ozone loss for the Arctic winter 2002/2003, Atmos. Chem. Phys., 5, 1437–1448, doi:10.5194/acp-5-1437-2005, 2005.

Grossmann, K., Offermann, D., Gusev, O., Oberheide, J., Riese, M., and Spang, R.: The crista-2 mission, J. Geophys. Res., 107 D23, 8173, 2002.

Günther, G., Müller, R., von Hobe, M., Stroh, F., Konopka, P., and Volk, C. M.: Quantification of transport across the boundary of the lower stratospheric vortex during Arctic winter 2002/2003, Atmos. Chem. Phys., 8, 3655–3670, doi:10.5194/acp-8-3655-2008, 2008.

Hanson, D. and Mauersberger, K.: Laboratory studies of the nitric acid trihydrate: Implications for the south polar stratosphere, Geophys. Res. Lett., 15, 855–858, doi:10.1029/GL015i008p00855, 1988.

Hase, F. and Höpfner, M.: Atmospheric ray path modeling for radiative transfer algorithms, Appl. Optics, 38, 3129–3133, doi:10.1364/AO.38.003129, 1999.

Hoffman, L., Weigel, K., Spang, R., Schroeder, S., Arndt, K., Lehmann, C., Kaufmann, M., Ern, M., Preusse, P., Stroh, F., and Riese, M.: CRISTA-NF measurements of water vapour during the SCOUT-O3 Tropical Aircraft Campaign, Adv. Space Res., 43(1), 74–81, doi:10.1016/j.asr.2008.03.018, 2009.

Hoffmann, L. and Alexander, M. J.: Retrieval of stratospheric temperatures from Atmospheric Infrared Sounder radiance measurements for gravity wave studies, J. Geophys. Res., 114, doi:10.1029/2008JD011241, 2009.

Höpfner, M., Luo, P., Massoli, P., Cairo, F., Spang, R., Snels, M., Di Donfrancesco, G., Stiller, G., von Clarmann, T., Fischer, H., and Biermann, U.: Spectroscopic evidence of NAT, STS, and ice in MIPAS infrared limb emission measurements of polar stratospheric clouds, Atmos. Chem. Phys., 6, 1201–1219, doi:10.1029/2003GL017231, 2006.

Höpfner, M., Pitts, M. C., and Poole, L. R.: Comparison between CALIPSO and MIPAS observations of polar stratospheric clouds, J. Geophys. Res., 114, doi:10.1029/2009JD012114, 2009.

Hoskins, B. J., McIntyre, M. E., and Robertson, A. W.: On the use and significance of isentropic potential vorticity maps, Quart. J. Roy. Meteorol. Soc., 111, 877–946, 1985.

IPCC: Climate Change 2007: The Physical Science Basis. Contribution of Working Group I to the Fourth Assessment Report of the Intergovernmental Panel on Climate Change, Cambridge University Press, Cambridge, United Kingdom and New York, NY, USA, edited by S. Solomon, D. Qin, M. Manning, Z. Chen, M. Marquis, K.B. Averyt, M. Tignor and H.L. Miller, 2007.

Keim, C.: Entwicklung und Verifikation der Sichtlinienstabilisierung für MIPAS auf dem hochfliegenden Forschungsflugzeug M55 Geophysica, Wissenschaftliche Berichte, FZKA, 6729, universität Karlsruhe, 2002.

Keim, C., Liu, G. Y., Blom, C. E., Fischer, H., Gulde, T., Höpfner, M., Piesch, C., Ravegnani, F., Roiger, A., Schlager, H., and Sitnikov, N.: Vertical profile of peroxyacetyl nitrate (PAN) from MIPAS-STR measurements over Brazil in February 2005 and its contribution to tropical UT NO_y partitioning, Atmos. Chem. Phys., 8, 4891–4902, doi:10.5194/acp-8-4891-2008, 2008.

Konopka, P., Steinhorst, H.-M., Grooß, J.-U., Günther, G., Müller, R., Elkins, J. W., Jost, H.-J., Richard, E., Schmidt, U., Toon, G., and McKenna, D. S.: Mixing and ozone loss in the 1999–2000 Arctic vortex: Simulations with the three–dimensional Chemical Lagrangian Model of the Stratosphere (CLaMS), J. Geophys. Res., 109, doi:10.1029/2003JD003792, 2004.

Konopka, P., Günther, G., Müller, R., dos Santos, F., Schiller, C., Ravegnani, F., Ulanovsky, A., Schlager, H., Volk, C., Viciani, S., Pan, L., McKenna, D. S., and Riese, M.: Contribution of mixing to upward transport across the tropical tropopause layer (TTL), Atmos. Chem. Phys., 7, 3285–3308, 2007.

Kullmann, A.: Ein flugzeuggetragenes kryogenes Infrarotspektrometer zur Fernerkundung klimarelevanter Spurengase im Tropopausenbereich, Ph.D. thesis, University of Wuppertal, 2006.

Kullmann, A., Riese, M., Olschewski, F., Stroh, F., and Grossmann, K.: Cryogenic Infrared Spectrometers and Telescopes for the Atmosphere - New Frontiers, Proceedings of SPIE, 5570, 423–432, 2004.

Lait, L. R.: An alternative form for potential vorticity, J. Atmos. Sci., 51, 1754–1759, 1994.

Marti, J. and Mauersberger, K.: A survey nad new measurements of ice vapor pressure at temperatures betwenn 170 and 250 K, Geophys. Res. Lett., 20, 363–366, 1993.

Massie, S., Gille, J., Khosravi, R., Lee, H., Kinnison, D., Francis, G., Nardi, B., Eden, T., Craig, C., Halvorson, C., Coffey, M., Packman, D., Cavanaugh, C., Craft, J., Dean, V., Ellis, D., Barnett, J., Hepplewhite, C., Lambert, A., Manney, G., Strawa, A., and Legg, M.: High Resolution Dynamics Limb Sounder observations of polar stratospheric clouds and subvisible cirrus, J. Geophys. Res., 112, doi:10.1029/2007JD008788, 2007.

McKenna, D. S., Grooß, J.-U., Günther, G., Konopka, P., Müller, R., Carver, G., and Sasano, Y.: A new Chemical Lagrangian Model of the Stratosphere (CLaMS) 2. Formulation of chemistry scheme and initialization, J. Geophys. Res., 107, doi:10.1029/2000JD000113, 2002a.

McKenna, D. S., Konopka, P., Grooß, J.-U., Günther, G., Müller, R., Spang, R., Offermann, D., and Orsolini, Y.: A new Chemical Lagrangian Model of the Stratosphere (CLaMS) 1. Formulation of advection and mixing, J. Geophys. Res., 107, doi:10.1029/2000JD000114, 2002b.

MDB: High-altitude M55 Geophysica aircraft - Investigators Handbook, 2002.

Molina, L. and Molina, M.: Production of Cl_2O_2 from the Self-Reaction of the ClO Radical, J. Phys. Chem., 91, 433–436, 1987.

Montzka, S. A.: Source Gases that Affect Stratospheric Ozone, in: Stratospheric Ozone Depletion and Climate Change, edited by Müller, R., Royal Society of Chemistry, 2012.

Müller, R.: Introduction, in: Stratospheric Ozone Depletion and Climate Change, edited by Müller, R., Royal Society of Chemistry, 2012a.

Müller, R., ed.: Stratospheric Ozone Depletion and Climate Change, Royal Society of Chemistry, 2012b.

Müller, R. and Günther, G.: A Generalized Form of Lait's Modified Potential Vorticity, J. Atmos. Sci., 60, 2229–2237, 2003.

Müller, R., Tilmes, S., Konopka, P., Grooß, J.-U., and Jost, H.-J.: Impact of mixing and chemical change on ozone-tracer relations in the polar vortex, Atmos. Chem. Phys., 5, 3139–3151, doi:10.5194/acp-5-3139-2005, 2005.

Nash, E. R., Newman, P. A., Rosenfield, J. E., and Schoeberl, M. R.: An oblective determination of the polar vortex using Ertel's potential vorticity, J. Geophys. Res., 101, 9471–9478, 1996.

Offermann, D., Grossmann, K., Barthol, P., Knieling, P., Riese, M., and Trant, R.: Cryogenic infrared spectrometers and telescopes for the atmosphere (crista) experiment and middle atmosphere variability, J. Geophys. Res., 104, 16 311–16 325, 1999.

Peter, T.: Microphysics and heterogeneous chemistry of polar stratospheric clouds, Annu. Rev. Phys. Chem., 48, 785–822, 1997.

Peter, T. and Grooß, J.-U.: Polar Stratospheric Clouds and Sulfate Aerosol Particles: Microphysics, Denitrification and Heterogeneous Chemistry, in: Stratospheric Ozone Depletion and Climate Change, edited by Müller, R., Royal Society of Chemistry, 2012.

Piesch, C., Gulde, T., Sartorius, C., Friedl-Vallon, F., Seefeldner, M., Wölfel, M., Blom, C., and Fischer, H.: Design of a MIPAS instrument for high-altitude aircraft, Proc. of the Second Intern. Airborne Remote Sensing Conference and Exhibition, Vol. II, 199–208, Ann Arbor, MI, USA, 1996.

Pitts, M., Poole, L., and Thomason, L.: CALIPSO polar stratospheric cloud observation: second generation detection algorithm and composition discrimination, Atmos. Chem. Phys., 9, 7577–7589, 2009.

Pitts, M. C., Poole, L. R., Dörnbrack, A., and Thomason, L. W.: The 2009/2010 Arctic polar stratospheric cloud season: a CALIPSO perspective, Atmos. Chem. Phys., 10, 24 205–24 243, doi:10.5194/acpd-10-24205-2010, 2010.

Plumb, R. A.: Tracer interrelationships in the stratosphere, Rev. Geophys., 45, doi:10.1029/2005RG000179, 2007.

Preusse, P.: Vorbereitung der Eichung der CRISTA-Spektrometer, diploma Thesis, University of Wuppertal, 1995.

Remedios, J. J., Leigh, R. J., Waterfall, A. M., Moore, D. P., Sembhi, H., Parkes, I., Greenhough, J., Chipperfield, M., and Hauglustaine, D.: MIPAS reference atmospheres and comparisons to V4.61/V4.62 MIPAS level 2 geophysical data sets, 7, 9973–10 017, doi:10.5194/acpd-7-9973-2007, 2007.

Riediger, O., Volk, C. M., Strunk, M., and Schmidt, U.: HAGAR - A new in situ tracer instrument for stratospheric balloons and high altitude aircraft, Eur. Comm. Air Pollut. Res. Report, 73, 727–730, 2000.

Riese, M., Spang, R., Preusse, P., Ern, M., Jarisch, M., Offermann, D., and Grossmann, K. U.: Cryogenic Infrared Spectrometers and Telescopes for the Atmosphere (CRISTA) data processing and atmospheric temperature and trace gas retrieval, J. Geophys. Res., 104, 16 349–16 367, doi:10.1016/S0273-1177(97)00172-5, 1999.

Riese, M., Friedl-Vallon, F., Spang, R., Preusse, P., Schiller, C., Hoffmann, L., Konopka, P., Oelhaf, H., von Clarmann, T., and Höpfner, M.: GLObal limb Radiance Imager for the Atmosphere (GLORIA): Scientific objectives, Adv. Space Res., 36, 989–995, doi:10.1016/j.asr.2005.04.115, 2005.

Riese, M., Ploeger, F., Rap, A., Vogel, B., Konopka, P., Dameris, M., and Forster, P.: Impact of uncertainties in atmospheric mixing on simulated UTLS composition and related radiative effects, J. Geophys. Res., doi:10.1029/2012JD017751, in press, 2012.

Rodgers, C. D.: Inverse Methods for Atmospheric Sounding: Theory and Practice, vol. 2 of *Series on Atmospheric, Oceanic and Planetary Physics*, World Scientific, 2000.

Rothman, L., Gordon, I., Barbe, A., Benner, D., Bernath, P., Birk, M., Boudon, V., Brown, L., Campargue, A., Champion, J.-P., Chance, K., Coudert, L., Dana, V., Devi, V., Fally, S., Flaud, J.-M., Gamache, R., Goldman, A., Jacquemart, D., Kleiner, I., Lacome, N., Lafferty, W., Mandin, J.-Y., Massie, S., Mikhailenko, S., Miller, C., Moazzen-Ahmadi, N., Naumenko, O., Nikitin, A., Orphal, J., Perevalov, V., Perrin, A., Predoi-Cross, A., Rinsland, C., Rotger, M., Simecková, M., Smith, M., Sung, K., Tashkun, S., Tennyson, J., Toth, R., Vandaele, A., and Auwera, J. V.: The HITRAN 2008 molecular spectroscopic database, J. Quant. Spec. Rad. Transf., 110, 533 – 572, doi:10.1016/j.jqsrt.2009.02.013, 2009.

Santee, M., MacKenzie, I., Manney, G., Chipperfield, M., Bernath, P., Walker, K., Boone, C., Froidevaux, L., Livesey, N., and Waters, J.: A study of stratospheric chlorine partitioning based on new satellite measurements and modeling, J. Geophys. Res., 113, 2008.

Schoeberl, M. R. and Hartmann, D. L.: The Dynamics of the Stratospheric Polar Vortex and Its Relation to Springtime Ozone Depletions, Science, 251, 46–52, 1991.

Schroeder, S., Kullman, A., Preusse, P., Stroh, F., Weigel, K., Ern, M., Knieling, P., Olschewski, F., Spang, R., and Riese, M.: Radiance calibration of CRISTA-NF, Adv. Space Res., 43(12), 1910–1917, doi:10.1016/j.asr.2009.03.009, 2009.

Solomon, S.: Stratospheric ozone depletion: A review of concepts and history, Rev. Geophys., 37, 275–315, 1999.

Solomon, S., Garcia, R. R., Roland, F. S., and Wuebbles, D. J.: On the depletion of Antartic ozone, Nature, 321, 755–758, 1986.

Spang, R. and Remedios, J. J.: Observations of a distinctive infra-red spectral feature in the atmospheric spectra of polar stratospheric clouds measured by the CRISTA instrument, J. Geophys. Res., 108, doi:10.1029/2003GL017231, 2003.

Spang, R., Riese, M., and Offermann, D.: CRISTA-2 observations of the south polar vortex in winter 1997: A new dataset for polar process studies, Geophys. Res. Lett., 28, 3159–3162, 2001.

Spang, R., Eidmann, G., Riese, M., Offermann, D., Preusse, P., Pfister, L., and Wang, P.-H.: CRISTA observations of cirrus clouds around the tropopause, J. Geophys. Res., 107, doi:10.1029/2001JD000698, 2002.

Spang, R., Remedios, J., and Kramer, L.: Polar stratospheric cloud observations by MIPAS on ENVISAT: detection method, validation and analysis of the northern hemisphere winter 2002/2003, Atmos. Chem. Phys., 5, 679–692, 2005.

Spang, R., Hoffman, L., Kullman, A., Olschewski, F., Preusse, P., Knieling, P., Schroeder, S., Stroh, F., Weigel, K., and Riese, M.: High resolution limb observations of clouds by the CRISTA-NF experiment during the SCOUT-O3 tropical aircraft campaign, Adv. Space Res., 42(10), 1765–1775, doi:10.1016/j.asr.2007.09.036, 2008.

Spang, R., Arndt, K., Dudhia, A., Höpfner, M., Hoffmann, L., Hurley, J., Grainger, R. G., Griessbach, S., Poulsen, C., Remedios, J. J., Riese, M., Sembhi, H., Siddans, R., Waterfall, A., and Zehner, C.: Fast cloud parameter retrievals of MIPAS/Envisat, Atmospheric Chemistry and Physics, 12, 7135–7164, doi:10.5194/acp-12-7135-2012, 2012.

Stolarski, R., Krueger, A., Schoeberl, M., McPeters, R., Newman, P., and Alpert, J.: Nimbus 7 satellite measurements of the springtime Antarctic ozone decrease, Nature, 322, 207–210, 1986.

Tikhonov, A. N. and Arsenin, V. Y.: Solutions of ill-posed problems, Winston, Washington D.C., USA, 1977.

Toon, O., Hamill, P., Turco, R., and Pinto, J.: Condensation of HNO3 and HCl in the winter polar stratospheres, Geophys. Res. Lett., 13, 1284–1287, 1986.

Twomey, S.: Introduction to the Mathematics of Inversion in Remote Sensing and Indirect Measurements, Dover, 1977.

Ulanovsky, A., Yushkov, V., Sitnikov, N., and Ravegnani, F.: FOZAN-II fast-response chemiluminescent airborne ozone analyzer, Instrum. Exp. Tech., 44, 249–256, doi:10.1023/A:1017535608026, 2001.

Ungermann, J.: Tomographic reconstruction of atmospheric volumes from infrared limb-imager measurements, Ph.D. thesis, Wuppertal University, 2011.

Ungermann, J., Kaufmann, M., Hoffmann, L., Preusse, P., Oelhaf, H., Friedl-Vallon, F., and Riese, M.: Towards a 3-D tomographic retrieval for the air-borne limb-imager GLORIA, Atmos. Meas. Tech., 3, 1647–1665, doi:10.5194/amt-3-1647-2010, 2010.

Ungermann, J., Kalicinsky, C., Olschewski, F., Knieling, P., Hoffmann, L., Blank, J., Woiwode, W., Oelhaf, H., Hösen, E., Volk, C. M., Ulanovsky, A., Ravegnani, F., Weigel, K., Stroh, F., and Riese, M.: CRISTA-NF measurements with unprecedented vertical resolution during the RECONCILE aircraft campaign, Atmos. Meas. Tech., 5, 1173–1191, doi:10.5194/amt-5-1173-2012, 2012.

von Hobe, M. and Stroh, F.: Stratospheric Halogen Chemistry, in: Stratospheric Ozone Depletion and Climate Change, edited by Müller, R., Royal Society of Chemistry, 2012.

Waibel, A. E., Peter, T., Carslaw, K. S., Oelhaf, H., Wetzel, G., Crutzen, P. J., Pöschl, U., Tsias, A., Reimer, E., and Fischer, H.: Arctic Ozone Loss Due to Denitrification, Science, 283, 2064–2069, doi:10.1126/science.283.5410.2064, 1999.

Waters, J., Froidevaux, L., Harwood, R., Jarnot, R., Pickett, H., Read, W., Siegel, P., Cofield, R., Filipiak, M., Flower, D., Holden, J., Lau, G., Livesey, N., Manney, G., Pumphrey, H., Santee, M., Wu, D., Cuddy, D., Lay, R., Loo, M., Perun, V., Schwartz, M., Stek, P., Thurstans, R., Boyles, M., Chandra, K., Chavez, M., Chen, G.-S., Chudasama, B., Dodge, R., Fuller, R., Girard, M., Jiang, J., Jiang, Y., Knosp, B., LaBelle, R., Lam, J., Lee, K., Miller, D., Oswald, J., Patel, N., Pukala, D., Quintero, O., Scaff, D., Van Snyder, W., Tope, M., Wagner, P., and Walch, M.: The Earth Observing System Microwave Limb Sounder (EOS MLS) on the Aura Satellite, IEEE Transactions on Geoscience and Remote Sensing, 44, doi:10.1109/TGRS.2006.873771, 2006.

Waugh, D. W. and Polvani, L. M.: Stratospheric Polar Vortices, in: The Stratosphere: Dynamics, Transport and Chemistry, edited by Polvani, L. M., Sobel, A. H., and Waugh, D. W., AGU, 2010.

Weigel, K.: Infrared limb-emission observations of the upper troposphere, lower stratosphere with high spatial resolution, Ph.D. thesis, University of Wuppertal, 2009.

Weigel, K., Riese, M., Hoffman, L., Hoefer, S., Kalicinsky, C., Knieling, P., Olschewski, F., Preusse, P., Spang, R., Stroh, F., and Volk, C.: CRISTA-NF measurements during the AMMA-SCOUT-O3 aircraft campaign, Atmos. Meas. Tech., 3, 1437–1455, doi:10.5194/amt-3-1437-2010, 2010.

Weinreb, M. P. and Neuendorffer, A. C.: Method to Apply Homogeneous-path Transmittance Models to Inhomogenous Atmospheres, J. Atmos. Sci., 30, 662–666, doi:10.1175/1520-0469(1973)030<0662:MTAHPT>2.0.CO;2, 1973.

Werner, A., Volk, C., Ivanovna, E., Wetter, T., Schiller, C., Schlager, H., and Konopka, P.: Quantifying transport into the Artic lowermost stratosphere, Atmos. Chem. Phys., 10, 11 623–11 639, doi:10.5194/acp-10-11623-2010, 2010.

Winker, D., Pelon, J., Coakley Jr., J., Ackerman, S., Charlson, R., Colarco, P., Flamant, P., Fu, Q., Hoff, M., Kittaka, C., Le Treut, H., Mccormick, M., Megie, G., Poole, L., Powell, K., Vaughan, M., and Wielicki, B.: THE CALIPSO MISSION: A

Global 3D View of Aerosols and Clouds, Bull. Amer. Meteor. Soc., 91, 1211–1229, doi:http://dx.doi.org/10.1175/2010BAMS3009.1, 2010.

Woiwode, W., Oelhaf, H., Gulde, T., Piesch, C., Maucher, G., Ebersoldt, A., Keim, C., Höpfner, M., Khaykin, S., Ravegnani, F., Ulanovsky, A. E., Volk, C. M., Hösen, E., Dörnbrack, A., Ungermann, J., Kalicinsky, C., and Orphal, J.: MIPAS-STR measurements in the Arctic UTLS in winter/spring 2010: instrument characterization, retrieval and validation, Atmospheric Measurement Techniques, 5, 1205–1228, doi:10.5194/amt-5-1205-2012, URL http://www.atmos-meas-tech.net/5/1205/2012/, 2012.